NISTIR 6309

Corrosion Fatigue Crack Initiation in Duplex Stainless Steel Paper Making Components

M. R. Stoudt

U.S. DEPARTMENT OF COMMERCE
Technology Administration
Metallurgy Division
Materials Science and Engineering
Laboratory
National Institute of Standards
and Technology
Gaithersburg, MD 20899

Final Report for:
NIST CRADA CN-1237

Prepared for:
John C. Rogers, Technical Director
Sandusky International, Inc.
615 West Market Street
P.O. Box 5012
Sandusky, OH 44871-5012

NIST

NISTIR 6309

Corrosion Fatigue Crack Initiation in Duplex Stainless Steel Paper Making Components

M. R. Stoudt

U.S. DEPARTMENT OF COMMERCE
Technology Administration
Metallurgy Division
Materials Science and Engineering
Laboratory
National Institute of Standards
and Technology
Gaithersburg, MD 20899

Final Report for:
NIST CRADA CN-1237

Prepared for:
John C. Rogers, Technical Director
Sandusky International, Inc.
615 West Market Street
P.O. Box 5012
Sandusky, OH 44871-5012

March 1999

U.S. DEPARTMENT OF COMMERCE
William M. Daley, Secretary

TECHNOLOGY ADMINISTRATION
Gary R. Bachula, Acting Under Secretary
for Technology

NATIONAL INSTITUTE OF STANDARDS
AND TECHNOLOGY
Raymond G. Kammer, Director

Executive Summary

The demand for more cost-effective paper production has generated a strong driving force for wider and faster paper machines. As a result, the reliability and durability of the metallic components in those machines have become pivotal issues and as such, increased the awareness of the enormous economic impact associated with equipment repair and replacement throughout the pulp and paper industry. According to some estimates, the annual costs associated with corrosion maintenance in the North American pulp and paper industry are on the order of one billion dollars. It is in the best interest of the industry to develop materials that are more resistant to the operational environment as components made from these materials would extend the service life and lower operating costs. However, premature failures of the suction roll shells and other metallic components are still routinely reported throughout this industry and while numerous improvements have been made to life prediction models, a disparity still exists between the laboratory measurement-based life predictions methods and actual service performance and this disparity is the largest hinderance to the development of new materials.

A good example of this problem has been reported by Sandusky International, the sole US based producer of suction roll shells for the paper industry. This company produces two duplex stainless steel alloys with very similar compositions and the performance predictions based on laboratory measurements and current life prediction methods indicate that the behaviors of these two alloys should be virtually identical in service. However, in the ten year period since the development of these alloys, Sandusky has not experienced a single service failure with one alloy while the other alloy continues to fail prematurely.

This research was primarily designed to develop a solution to the problem as reported by Sandusky International. Simply stated, that problem is: in-service Alloy 75[1] corrosion fatigue failures occur even though the life prediction methods indicate they should not. The existing measurement methods and interpretations indicate that both Alloy 75 and Alloy 86 should have essentially identical corrosion fatigue behaviors, yet one alloy fails in service while the other does not. At the onset of this program, it was thought that the development of a crack propagation measurement that had a higher resolution would provide better data for use in the existing life prediction models and that this data would both reveal the source of the differences in the behaviors and enable the development of alloys which are more resistant to this failure mode. A review of the literature on crack propagation in these alloys and life prediction methods led to a set of experiments that were designed to evaluate the relative influences of anodic and cathodic processes on environmentally induced fracture in these alloys. These experiments included: a) scratch repassivation experiments conducted under both free corrosion and controlled electrode potential conditions which evaluated the influence of frequency effects on the fatigue crack

---

[1] Certain commercial products are identified in this report in order to adequately specify the equipment, processes or materials used. Such identification does not imply recommendation by the National Institute of Standards and Technology, nor does it imply that these products are the best available for the purpose.

propagation rate and b) slow strain rate tensile tests to determine the relative sensitivity to the hydrogen generated during a crack propagation event.

The results of these experiments revealed no reasonable expectation that a modification in one of the experimental parameters used to predict crack propagation would reveal a significant difference in the behaviors of these two duplex alloys and that the development of a new, higher resolution, long crack propagation technique would not yield an appropriate solution to the problem. As a result, it was necessary to determine whether a process that was not considered previously could induce fatigue failure in one alloy, but not in the other. Consequently, a second set of experiments was conducted to determine what role corrosion may have in the initiation of cracks in these alloys. These experiments involved a detailed evaluation of the complex corrosion behaviors of the two duplex stainless steel alloys in the paper processing environment and an evaluation of the mechanical properties under controlled conditions where pitting was known to occur.

The second set of experiments clearly demonstrated that Alloy 75 was significantly more likely to pit in service than Alloy 86 and that during pitting, the more ductile austenitic phase was preferentially attacked. Furthermore, the morphology of these pits concentrates stress and nucleates cracks more effectively than predicted by the conventional life prediction models. Therefore, it was concluded that the pitting resistance and the resulting pit morphology in Alloy 75 is the source of the disparity in the performance of the alloys in service and that better pitting resistance is a key factor in the development of alloys which are more resistant to this failure mechanism.

Abstract

The pulp and paper industry is frequently impacted by the enormous cost of replacing prematurely failed suction roll shells and other metallic components. A great deal of research has lead to numerous improvements in the models used for life prediction which has guided alloy development, but a disparity still exists between laboratory scale life prediction methods and the actual service performance and this disparity is an inherent problem hindering the development of new materials. Sandusky International produces two duplex stainless steel alloys with very similar compositions and the performance predictions based on current life prediction methods indicate that the behaviors of these two alloys should be similar in service. However, in the ten year period since the development of these alloys, Sandusky has not experienced a single service failure with one alloy while the other continues to fail prematurely. An evaluation was undertaken to determine the fundamental factors of this difference in performance.

Two hypotheses were adopted for this study. The first assumed that a problem existed in the measurement method used to generate the data used in the life prediction models or that this data was deficient in some fashion. The results of that evaluation revealed no reasonable expectation that a modification of the experimental parameters used to predict crack propagation would yield a cause for the reported discrepancy in performance between the two Sandusky alloys. The second hypothesis evaluated whether a process could promote cracking in one alloy and not the other. The results of this evaluation showed that overall, Alloy 75 and Alloy 86 have quite similar electrochemical and mechanical behaviors. The only significant difference observed between the two alloys in an aerated, simulated deinked white water environment was a wider separation between the free corrosion and pitting potentials in the alloy that has not exhibited premature failure (Alloy 86). In general, a small separation between these two potentials establishes a high probability for pitting during service and a wide separation denotes a low probability for pitting under the same corrosion conditions.

Slow strain rate tensile tests were used to further evaluate whether the resistance to pitting is the primary factor that determines the performance of these alloys in a paper making environment. The results of that analysis revealed that whenever pitting did occur, the failuremode was identical regardless of the alloy examined. Failure was always due to a reduction in cross sectional area caused by the formation and propagation of pitting which dissolved the more ductile phase (austenite). This action resulted in a simultaneous decrease in the fracture toughness of the alloy and an increase in the applied stress intensity and rapid failure occurred when the stress intensity reached the value of K_{Iscc} for the alloy. An analysis of an actual service failure supported this finding. The main conclusion drawn from this study was: the discrepancy in the performance between the two Sandusky duplex stainless alloys was a direct result of the predictive models not properly addressing the role of pitting corrosion in the fatigue crack initiation process.

Table of Contents

11. Introduction

1.1 The Industrial Problem

The demand for more cost-effective paper production has given rise to a strong driving force for wider and faster paper machines. As a result, the reliability and durability of the metallic components in those machines have become pivotal issues and as such, increased the awareness of the enormous economic impact associated with equipment repair and replacement throughout the pulp and paper industry. According to some estimates, the annual costs associated with corrosion maintenance in the North American pulp and paper industry is on the order of one billion dollars [1]. It is in the best interest of the industry to develop materials that are more resistant to the operational environment as components made from these materials would extend the service life and lower operating costs.

The environmental conditions in a pulp-paper mill generally range from alkaline-sulfide in the initial pulping operations to strongly oxidizing (bleaching) in the later processing steps [1]. These widely varying conditions create very harsh environments for the materials used for these operations and it follows that many significant and differing corrosion problems exist throughout this industry. The final stages of the paper making process involve separating the processing solutions from the pulp slurry and it is normally performed through a series of suction roll shells (also referred to as press rolls). These devices are usually cylindrical metal shells perforated with a multitude of radial holes. The length of a typical shell is normally determined by the width of the paper machine (up to 8 m) and depending on the type of paper produced, the wall thickness may range from 5 cm to 10 cm with an outside diameter on the order of about 1 m [2, 3]. These shells are typically under moderate vacuum and the extracted processing solutions are passed through the holes in the shell walls (shown schematically in Figure 1). Roll shells are integral components in the paper making process and failure of these devices has been a long-standing problem in the industry. Failure of these rolls is most often attributed to corrosion fatigue although there has been some speculation about the involvement of alternative modes of corrosion and corrosion-assisted cracking [4].

Historically, suction roll shells have been made with a wide variety of materials and fabrication techniques. Prior to 1954, bronze alloys were used almost exclusively throughout the industry for suction roll shell materials, but the modulus of the available bronzes could not withstand the higher stresses generated by the increased widths and operational speeds of the newer paper machines. These alloys were also shown to be fairly susceptible to both erosion corrosion and general corrosion which often resulted in accelerated failure rates [5]. As a result, a variety of austenitic and martensitic stainless steel alloys were developed in an attempt to meet the demands for increased performance. While these steels could easily withstand the increased stress requirements, the resistances to the processing environments was not acceptable. Since the late 1960's, duplex stainless steels have been developed for suction roll shell applications and to date, these alloys have demonstrated a better overall performance in the processing environments, but unfortunately, premature failures are still common occurrences [3, 4].

Suction roll shells routinely operate under conditions that are highly conducive to the initiation and growth of fatigue cracks. In most paper machines, these rolls are only supported at their ends and the combined effects of applied nip roll pressures, suction box loading and gravitational forces can create large alternating stresses with high rotational frequencies. A typical service life of one of these components ranges from five to eight years and it is not uncommon for a roll shell to experience more than 10^9 stress cycles during a single year of operation [2]. In addition to the high degree of mechanical stresses, the roll shell may be in constant contact with the processing white water which, depending upon the specific application, may be a very aggressive environment [2, 3, 6]. The current industrial trend to reduce mill effluents through the use of closed white water systems has exacerbated the corrosive nature of these solutions by increasing concentrations in the recycle, thus creating the need for even more resistant alloys [1].

Premature failures of the suction roll shells and other metallic components are still routinely reported throughout this industry and while numerous improvements have been made to life prediction models, the disparity between laboratory measurement-based life predictions and actual service performance remains the primary problem hindering the development of new materials. A good example of this problem has been reported by Sandusky International, the sole US based producer of suction roll shells for the paper industry. This company produces two alloys with very similar compositions and the performance predictions based on laboratory measurements and current life prediction methods indicate that the behaviors of these two alloys should be virtually identical in service. However, in the ten year period since the development of these alloys, Sandusky has not experienced a single service failure with one alloy while the other alloy continues to fail prematurely. This evaluation addresses the many questions raised by this disparity.

1.2 Review of Relevant Literature

1.2.1 Stress Corrosion Cracking and Crack Initiation

Failure in suction roll shells is almost always caused by the initiation and growth of cracks in the ligaments between the holes in the shell. These cracks most often initiate in the regions of the highest tensile stresses, (i.e., on the inside diameter of the shell near the mid-span) and grow in a circumferential fashion, although other morphologies are frequently encountered [2]. Corrosion is also known to be an important factor in this problem. Erosion corrosion, incurred from high flow rates of the processing solution, has been shown to accelerate failures in these components through thinning the ligament area between holes, thereby reducing the load bearing surface area which increases the mean cyclic stress levels. Resistance to this form of corrosion is a key factor for any material under consideration for use as a roll shell. When compared to the other alloys developed for suction roll shells, duplex stainless alloys have demonstrated substantially better resistance to erosion corrosion as examinations of service failures exhibit little or no visible evidence of this form of corrosion [3, 4 , 7].

In general, the overall performance of duplex alloys has been superior to other suction roll shell alloys in paper making environments, but the performance of these alloys tends to be dependent on the particular alloy heat treatment. In addition, the operations used for fabrication often generate residual tensile stresses which can also adversely affect the fatigue life. The complicated duplex microstructure is generally obtained through the use of ferrite phase stabilizers such as chromium and/or molybdenum. These alloys routinely contain high chromium contents which have been shown to lead to problems with high temperature embrittlement and intergranular corrosion [8]. Demo showed that single phase ferritic stainless steels with chromium contents on the order of 25%, frequently exhibited high ductile to brittle transition temperatures due to the formation of large, continuous chromium nitrides and carbonitrides along the grain boundaries [9]. These effects normally occur at somewhat higher temperature ranges (e.g., approximately 450 °C), but depending on the alloy composition and thermal treatments, the onset of embrittlement may occur at much lower temperatures [8]. Plumtree and Gullberg found that the brittle behavior observed by Demo was strongly dependent on the cooling rate and that slow, air cooling produced the lowest fracture toughness as well as significantly reduced corrosion resistance [10].

The superior corrosion resistance of stainless steels is generally attributed to the presence of a thin, continuous, thermodynamically stable, oxide film which effectively isolates the metal from the environment. When passive films are involved in any corrosion process, the repair of the film after a rupture event is most often the determining factor in the resistance of the material to the environment [11, 12]. Depending on the type of environment, the passive film may be susceptible to localized forms of attack such as pitting and crevice corrosion. The passive behavior and passive film breakdown of stainless steels have been the focus of numerous investigations and the processes involved are described in great detail in the literature [13-15]. It is generally accepted that the rate of stable pit formation is proportional to the degree of undermining and retention of the surface oxide film which, in turn, is dependent upon many factors (e.g., the type and concentration of ionic species, temperature, aeration, etc.) [16-18]. Newman postulates that in many cases, the overall pitting resistance of a material may be better determined by the ability to repair a rupture in the passive film rather than the general ability to resist film breakdown [12]. This is particularly important in the processes that govern the initiation of environmentally-induced cracking.

In an aqueous environment, an environmentally induced cracking process generally occurs by one of three basic classes of mechanisms: a) anodic slip dissolution, b) film-induced cleavage, or c) hydrogen embrittlement [17, 19, 20]. While these mechanisms are based on either static or monotonic loading, they are also equally applicable to cyclic loading.

The mechanism of anodic slip dissolution was one of the first proposed environmentally induced cracking mechanisms and still receives considerable support. In this mechanism, tensile stress is assumed to produce sufficient strain to rupture the surface film at an emerging slip step. A crack then grows by anodic dissolution of the unfilmed surface produced at the rupture site. Most investigators now agree that some form of film rupture is essential to the crack initiation process, but considerable controversy persists as to how an environmentally induced crack grows thereafter. The electrochemical reactions may indeed trigger a brittle mechanical cracking process that accounts for crack growth. However, in some cases, crack growth has been observed to proceed discontinuously (i.e., in steps) and corresponding periodic crack arrest markings (striations) are frequently observed on the surface. This result is contrary to the smooth increases in crack length expected for a crack growth process controlled by purely electrochemical means [21].

The film-induced cleavage (FIC) mechanism has been proposed to explain the discontinuous, transgranular crack growth and high transgranular crack growth rates. This mechanism is based on the concept that the fracture of brittle surface films (such as dealloyed films in certain alloys and oxides on pure metals and other alloys) generates sufficient energy for crack propagation. If sufficient velocity is developed at the film/metal interface, the sharp crack formed in this brittle film may be injected into the underlying metal substrate where it will continue to propagate until it arrests through the formation and emission of blunting dislocations at the crack tip [22, 23]. The surface film must then reform at the crack tip surface before a new burst of brittle crack growth is possible. In the FIC mechanism, anodic dissolution is only required to form the brittle surface film, not to propagate the crack as in the case of anodic slip dissolution. As a result, the brittle surface film may form at much lower anodic dissolution rates so, according to this mechanism, a low anodic current at the strained surface can foster rapid, discontinuous, brittle cracking [21, 22].

The hydrogen embrittlement (HE) mechanism is generally defined as a brittle mechanical fracture resulting from penetration and diffusion of atomic hydrogen into the crystal structure of a metal or alloy. In an aqueous corrosion process, hydrogen is usually a product of the cathodic reaction and it may be generated by the reduction of water or acid through either of the following reactions: [24]

$$H_2O + e^- \rightarrow H + OH^- \tag{1}$$

$$H^+ + e^- \rightarrow H \tag{2}$$

Before the H_2 molecule can be formed, there is a significant residence time of the nascent H atom on the surface, especially if cathodic poisons such as S^{-2} and As^{+3} are present to delay the recombination rate. During this time, the atomic hydrogen can easily diffuse into the lattice and cause embrittlement. In general, there is an incubation time before the onset of cracking which decreases with increasing applied stress, and most systems also possess a minimum stress below which HE will not occur [25]. Hydrogen embrittlement is especially prevalent in ferritic iron based alloys because of the restricted slip capabilities associated with the body centered cubic (BCC) crystal structure. While the inherent higher ductility, lower hydrogen solubility and hydrogen diffusivity generally make austenitic steels more resistant to HE, these alloys can also exhibit susceptibility if there is enough cold work present [14, 21].

The major difference between these mechanisms for environmentally induced cracking is that any corrosive solution can produce HE provided that the alloy has a susceptible microstructure and enough hydrogen is liberated by cathodic reactions on the surface. The anodic dissolution and film-induced cleavage mechanisms, on the other hand, require a specific, and usually different, dissolved species for each alloy system [20, 25, 26].

The rates of metal dissolution, hydrogen-ion reduction and subsequently, crack growth, are all controlled by the reactions required to restore the passive film on the freshly created surface at the crack tip. At any given electrochemical potential, the film restoration reactions are controlled by three factors. These are: a) the film rupture rate, b) the solution renewal rate and c) the rate of repassivation [17, 27, 28]. In cases involving fatigue loading, both the magnitude of the cyclic stress and the frequency are also known to exert very strong influences on the rate of crack extension [27]. When a crack is immersed in solution, cyclic stresses can continuously pump the aggressive solution into the region of the crack tip through the opening and closing action between the mating faces of a crack wall. This process can create a state of continual blunting and resharpening of a crack tip which is known to have a very strong influence on the rate of anodic dissolution. This type of synergistic interaction between the environment, cyclic loads and material microstructure is generally referred to as "corrosion fatigue." As a result, the mechanisms proposed to govern corrosion fatigue are similar to those for stress corrosion cracking in that they tend to be specific to a particular material-environment-loading system [11, 27, 29].

As in the case of stress corrosion cracking, the rates of crack initiation and propagation in corrosion fatigue are strongly dependent on the stability of the passive film. In environmental conditions where the passive film is completely stable, the influence of corrosion on the initiation process will be relatively small. However, when the film is continuously ruptured by the formation of persistent slip bands or other mechanical deformation processes, the influence of corrosion on the initiation rate will be considerably higher [27]. The strongest influence of corrosion occurs under the conditions where the passivity is essentially unstable. Under these conditions, both crack initiation and propagation are rapid and the impact on the resulting fatigue life is substantial [30].

The premise that corrosion-induced pits in the specimen surface act as stress concentrators was one of the earliest proposed mechanisms to explain the reduction in fatigue life in aqueous environments [30]. It was assumed that pits induced by an active corrosion process either increased the applied stress by reducing the cross-sectional area or lowered the threshold stress required to initiate fatigue cracks [31]. While pitting certainly has a strong influence on the crack initiation process, it is more realistic to assume that no one, specific mechanism completely governs the corrosion fatigue initiation process in aqueous media. There have been many other mechanisms proposed and they can be generally stated as follows: a) stress concentrations at the base of corrosion pits, b) enhanced slip irreversibility due to dissolution or oxidation of slip steps, c) preferential corrosion attack at regions of highly localized plastic deformation, d) preferential attack in regions where the passive film has been ruptured, and e) surface energy reductions resulting from adsorption of environmental species [11, 27, 31]. Corrosion fatigue is believed to be the primary fracture mechanism in the failure of duplex stainless suction roll shells. This is based on the examination of numerous service failures, where the general location, orientation and crack front markings strongly suggest interactions between the cyclic loading and the processing environment. However, the exact cause of these failures is still somewhat inconclusive as laboratory fatigue crack growth experiments have been unable to adequately explain or predict the in-service failures.

1.2.2 Life Prediction in Corrosion Fatigue

The effect of environment on the rate of fatigue crack growth is often characterized by considering different combinations of crack growth measured under purely mechanical fatigue and under stress corrosion conditions. Figure 2a is a schematic illustration of the sigmoidal relationship between stress corrosion crack growth velocity (da/dN) and the Mode I stress intensity factor, (K_I). This figure also exhibits another threshold value of stress intensity known as K_{Iscc} which is determined by the environmental interaction. Above this threshold, the crack velocity sharply increases with stress intensity (Region I) and below it, the environment has no appreciable effect. This is followed by a region of stable crack growth in which the crack growth rate is essentially independent of the applied K (Region II). Beyond Region II, the value of applied K quickly approaches the fracture toughness for the material resulting in a sharp increase in crack velocity (Region III). The regions in this figure are often likened to: initiation and near-threshold propagation (Region I), stable crack propagation (Region II) and unstable growth and fracture (Region III). McEvily and Wei schematically illustrated the effects of the environment on fatigue crack propagation. [32] Figures 2b, 2c and 2d, illustrate the three main types of interactions associated with corrosion fatigue. Figure 2b represents the "true corrosion fatigue" condition where the environment alone is assumed to have no effect on the crack growth behavior. In this case, the environment accelerates crack growth only under cyclic loading conditions through the mechanisms outlined earlier. True corrosion fatigue is also known to influence cyclic fracture at stress intensity values below K_{Iscc}. Figure 2c represents "stress corrosion-fatigue" which is believed to be a simple superposition of mechanical fatigue and stress corrosion cracking. In this form, crack propagation is only known to occur at ΔK and R values where K_{max} is larger than K_{Iscc}. The combination of the effects of true corrosion fatigue and stress corrosion-fatigue may result in a "mixed corrosion/stress corrosion fatigue behavior" which is illustrated in Figure 2d. Further descriptions of these effects on crack propagation can be found elsewhere in the literature [27].

As stated earlier, corrosion fatigue results from the synergistic interactions between specific environments, cyclic loading parameters and material microconstituents. The application of fracture mechanics to fatigue has led to the development of several reasonably good prediction models for crack growth in benign environments. These models generally hold for a wide range of materials and loading conditions and in some cases, even allow for determinations of the actual crack extension with each loading cycle. Several, well accepted empirical models are routinely employed for life predictions under conditions of purely mechanical fatigue, (e.g, the Paris and Coffin-Manson equations [33]) unfortunately, the uncertainties associated with the environmental interactions do not allow for such predictions in corrosion fatigue. It is not surprising that quantitative models have not been fully developed for this very complex problem or that a widely accepted model that predicts the corrosion fatigue behavior of a wide range of materials and environments still does not exist in the literature [27]. As a result, the majority of life prediction data in corrosion fatigue are obtained through numerous experiments on specific materials and in specific environments [29].

Most predictive corrosion fatigue models are based on a superposition-type approach such as the one put forth by Wei and Landes in the early 1970's [27]. This model assumes that the overall crack growth rate for a given material and environment, $(da/dN)_T$, can be determined by a linear superposition of the crack extension rates obtained from purely mechanical fatigue measurement and under conditions of stress corrosion cracking as shown in Equation 3 [34].

$$\left(\frac{da}{dN}\right)_T = \left(\frac{da}{dN}\right)_F + \left(\frac{da}{dN}\right)_{SC} \tag{3}$$

In this equation, the environmentally induced crack growth rate $(da/dN)_{sc}$ is obtained by integrating the amount of crack extension resulting from one fatigue cycle such that [34]

$$\left(\frac{da}{dN}\right)_{SC} \alpha \int_0^\tau \frac{da}{dt}(K)\,dt \tag{4}$$

where τ is the period of the load cycle. This model provides a reasonable prediction of the corrosion fatigue behavior for a limited number of systems [27], unfortunately, it does not adequately address the synergy between the mechanical and environmental aspects of the corrosion fatigue process. The superposition model also assumes that the rate of stress corrosion crack growth is exactly the same under monotonic and cyclic loading conditions. Other investigators have proposed alternatives to address some of the limitations in the superposition approach. These essentially amount to the addition of corrosion fatigue terms to the Wei and Landes equation:

$$\left(\frac{da}{dN}\right)_T = \left(\frac{da}{dN}\right)_F + \left(\frac{da}{dN}\right)_{SC} + \left(\frac{da}{dN}\right)_{CF} \tag{5}$$

Austen and McIntyre used this approach as the basis of their process competition model. They postulated that fatigue and SCC could be mutually competitive processes, and that the process which requires the lowest stress intensity will dominate the rate of crack extension [35]. In other words, either K_{max} or K_{Iscc} can determine the rate of crack growth. This approach has shown considerable promise in explaining crack growth under conditions of low applied stress intensities.

Investigations into the fundamental principles associated with stress corrosion cracking behavior have led to a fairly good understanding of the nature of passive film rupture and the role it has in crack propagation. These principles are also applicable to the processes in corrosion fatigue. In the case of a corrosion fatigue system involving a passive film, each crack extension event will produce a current transient resulting from the chemical reactions required to restore the passive film on the freshly generated bare surface. Figure 3 is a schematic showing the relationship between these current transients and cyclic loading. Models which attempt to predict crack growth through the use of film rupture events have shown great promise, especially in cases where the stress intensities are near the threshold value required for crack growth or where the loading frequencies are relatively low. This approach has been used extensively to predict the corrosion fatigue behavior of both ferritic and stainless steels in high temperature, high purity water environments as well as to determine the effects of frequency on corrosion fatigue crack propagation [29, 36]. Equations of varying forms exist throughout the literature, but they generally involve some form of integration of the total current generated during a single repassivation event. An example is shown in Equation 6:

$$\left(\frac{da}{dN}\right)_{cf} = c\int_{0}^{\tau}\frac{i(t)}{nF}\,dt \qquad (6)$$

In this equation, τ is the mean time between film rupture events (which, in fatigue loading, is the reciprocal of the cyclic frequency), i(t) is the current density as a function of time, n is the number of transferred electrons, F is Faraday's constant and c is a proportionality constant.

Better measurements of the electrochemical parameters appear to be the most practical approach for the development of more accurate corrosion fatigue life prediction models. None of the predictive models existing in the literature for duplex stainless steels sufficiently address the complex electrochemical behavior of these alloys during corrosion fatigue. In addition, only limited information on the electrochemical behavior of duplex alloys in paper making environments is available in the literature. As a result, many components still fail prematurely due to inaccurate life predictions. In that regard, measurements of the electrochemical behavior, specifically those which address repassivation, are necessary if an accurate predictive model is to be developed for the corrosion fatigue behavior of a duplex stainless steel alloy in a paper making environment.

1.2.3 Corrosion of Duplex Stainless Steels in Paper Making Environments

A typical paper making white water environment contains a variety of ionic species, many of which are known to individually cause corrosion of stainless steel. The compositions of these solutions vary widely according to the type of paper produced, but they most often contain chloride, sulfate, and sulfite. Depending on the operating conditions in the paper mill, the concentrations of these species may vary from a few to several thousand parts per million which makes life predictions in these environments all the more difficult. In recent years, the practice of using thiosulfates ($S_2O_3^{-2}$) to brighten recycled paper pulp has created a different set of corrosion related problems. The results of numerous investigations have shown that the thiosulfate ion can be particularly aggressive to austenitic stainless steels [12, 37]. The aggressive nature of this environment may be particularly important with respect to a duplex stainless steel. Spaehn postulates that the complex microstructures involved with two phase alloys may actually enable more than one active cracking mechanism [30]. In other words, the anodic dissolution mechanism may be active in the austenitic phase while hydrogen embrittlement may be active in the ferritic phase.

Austenitic stainless steels such as type 304 have been shown to be generally susceptible to pitting attack in neutral to slightly acidic solution that contain dissolved chlorides. Several different mechanisms for chloride induced pitting in these alloys are discussed in the literature, but in essence, they are based on the concept that chloride ions adsorb on the surface and catalyze the liberation of the Fe^{+3} ion through displacement of the outer layers of the passive film. The passive film is continuously thinned in that localized region until anodic dissolution reactions with the bare metal are activated and the pit becomes stable [13]. The pitting resistance is known to be dependent upon the density of preferred nucleation sites such as heterogeneous sulfide or chromium oxide inclusions as well as many other factors, such as, metallurgical condition, amount of cold work and second phase precipitates [15]. Because pitting is a fairly common problem, many preventative measures have been developed and used with reasonable degrees of success. However, pitting behavior is very much a function of the concentration of the ionic species in solution and small additions of thiosulfates to a chloride solution have been shown to have a strongly adverse effect on the pitting resistance of austenitic stainless steels [12, 38]. The aggressive effects of these ions are well documented and are known to cause pitting in pure iron as well as passive film breakdown and, in some cases, extraordinarily rapid cracking in sensitized stainless steels [12, 38, 39]. These observations have been attributed, at least in part, to a synergistic interaction between the chloride and thiosulfate ions present in the solution [18, 40].

The thiosulfate ion is known to be thermodynamically unstable in solutions with moderate to low pH levels (i.e., $pH \approx 4$ to 6) and in solutions of this type, it can readily disassociate to elemental sulfur or to other ionic forms [41]. Thiosulfate can also easily be electrochemically reduced to sulfide ions as by-products of any corrosion reactions in solutions of this pH range. Figure 4 is a graphic representation (E-pH diagram) illustrating the instability of the thiosulfate ion over a relatively small range of electrode potentials [41]. The deleterious effects of these ions have been well documented in the literature. Newman and Sieradzki showed free sulfur in solution can promote intergranular stress corrosion cracking in sensitized stainless steels [17]. The sulfide ion quickly bonds with free hydrogen to form H_2S, which is known to both promote active dissolution, and inhibit repassivation [15]. H_2S is also a well known hydrogen recombination poison, which may promote the hydrogen embrittlement mechanism [13].

Following the hypothesis put forward by Spaehn, it is reasonable to assume that distinctly different and simultaneous mechanisms may occur within the individual phases of a duplex steel. That is, embrittlement reactions may be active in the ferritic phase if the dissolution reactions stimulated by the thiosulfate/chloride attack of the austenite liberate sufficient hydrogen and recombination poisons. The limited electrochemical data available for duplex alloys in this type of environment do not provide sufficient information to eliminate Spaehn's hypothesis as a possibility.

1.3 Development of a More Suitable Measurement

The review of the relevant literature revealed that the existing corrosion and corrosion fatigue test methodology and data do not adequately address the complex problems associated with duplex stainless steels in a paper making environment. As a result, they are not trustworthy indicators of the performance of these materials in suction roll shell applications. Also, the laboratory based stress vs. cycles-to-failure (S-N) data available in the literature for these materials often do not agree with actual service performance [2]. The inability of current laboratory tests to accurately predict suction roll performance is a considerable impediment to the development of new classes of suction roll materials. Because of this lack of suitable information, this industry is forced to continue to rely heavily on prototype development which is expensive, time consuming, and only permits evaluation of a limited number of candidate materials at any one time. Also, successful candidate materials are rarely retired for destructive metallurgical evaluation to uncover the reason for success. Due to the lack of adequate life prediction models, paper producers must often make material decisions based on empirical laboratory data that may or may not be representative of the actual performance in the field [2-4, 7].

In response to these issues, NIST and Sandusky International designed a study to improve the existing measurement methods or, if possible, develop new methods to assist this industry in addressing the fundamental corrosion fatigue behavior of duplex stainless steels in a paper making environment. This study was also designed to address some of the data limitations which currently impede the development of more resistant alloys. The current industrial test methodology employs testing a variety of materials in various environments in order to rank the overall performance. An evaluation of this type typically includes: simple exposure corrosion tests, crack propagation tests, and general S-N fatigue tests [4]. While this approach may yield some usable information, it is very costly and insufficient in several areas.

In order to develop data that is more representative of the actual service conditions, it is necessary to better understand the synergy between the service environment and the loading conditions. It is reasonable to assume that more representative data would improve the accuracy of the current predictive models for corrosion fatigue. The approach taken for this study was based on the assumption that a linear superposition model of the type proposed by Wei and Landes (Equation 3) could be used to estimate the corrosion fatigue behavior in service. The performance data available in the literature for these materials in benign environments is more than adequate to predict the behavior under conditions of pure mechanical fatigue. Unfortunately, this is not the case for the electrochemical data required for the environmentally induced cracking terms in the same equation. More thorough information regarding the electrochemical behavior of the duplex alloys in paper making environments is a key factor in the development of a more representative environmental term. Several basic electrochemical techniques are applicable to this purpose and, as a result, they have become very powerful, standardized tools for characterizing the performance of a material under a wide range of environmental conditions.

The goals of this study were: a) to address the limitations in the performance data for duplex stainless steel alloys in a simulated paper making solution and thereby improve the accuracy of the electrochemical term in a superposition-type life prediction model, b) to evaluate the influence of different alloying elements on the corrosion fatigue resistance of two duplex steel alloys and c) to determine whether the information gained as a result of this study will explain the reported differences in behavior between the two Sandusky alloys. This evaluation is specifically designed to be compatible with other efforts to develop better life prediction models and it is expected to have an important role in the development of a more representative test method as well as materials that are more resistant to the effects of the paper making environment.

2. Experimental Procedure

2.1 Materials

Table 1 lists the nominal chemical compositions of the two duplex stainless suction roll shell steels evaluated in this study and the typical mechanical properties of these alloys (as reported by Sandusky International) are presented in Table 2. Lengthwise and cross sections of each alloy were cut from bar stock for metallographic analysis in order to establish the base metal microstructure of the duplex alloys. The sections were prepared according to standard metallographic procedure and then etched with Viella's Etchant [42, 43]. This etchant was chosen because it generally works well with stainless steels and it allowed for easy distinction between the two phases in the duplex alloys. The nominal composition of Viella's Etchant is 1 g picric acid dissolved in 5 ml of HCl and 100 ml of ethanol [44].

2.2 Electrochemical Measurements

Since the behavior of any metal in a corrosive environment is dependant upon a variety of factors such as the type and concentration of the ionic species present, the solution temperature, the pH, and the amount of dissolved oxygen, it is often necessary to conduct a series of experiments which control and/or isolate specific variables and then combine those results to obtain the overall behavior in a particular environment. An evaluation was designed to develop a fundamental understanding of the electrochemical behavior of each of the two duplex stainless alloys in standardized, simulated paper making solution. The techniques employed for this investigation consisted of measurements of the free corrosion potentials, potentiodynamic polarization experiments, cyclic voltammetry and AC impedance measurements.

Samples of each alloy were cut from bar stock and mounted in epoxy. Electrical contact was made prior to mounting through the use of a wire attached to the sample with a conductive epoxy. Standard metallographic procedures were used to polish the electrodes to a 1 μm diamond finish prior to testing. All of the electrochemical experiments were conducted at 50 °C ± 1 °C in solutions with the same nominal composition. That composition is shown in Table 3.

The free corrosion potential (FCP) of each alloy was measured in naturally aerated and deaerated simulated, deinked white water by placing the electrode along with a saturated calomel reference electrode (SCE) in a double-walled electrochemical cell connected to a computer controlled high impedance digital voltmeter. The cell was attached to a recirculating temperature bath that fixed the solution temperature to 50 °C ± 1.0 °C. The measured potential and the elapsed time were recorded by the computer during the period required for the system to reach steady state. For the FCP measurements in deaerated solution, nitrogen was bubbled vigorously through the solution for twenty minutes to deaerate the solution, after which, the flow rate was reduced and changed to a dispersion over the top of the solution surface.

The potentiodynamic polarization experiments were conducted by using a computer controlled potentiostat and a saturated calomel reference electrode. The potentiostat applies current to the sample to keep the potential difference between the sample and a reference electrode equal to a predetermined value (E_d). For potentiodynamic polarization experiments, the potential, E_d, is not constant, but varies at a constant scan rate between selected extremes. For these experiments, the potential was scanned at 20 mV/s and 5 mV/s over a range of potentials designed to exceed those expected in normal service. The potential was swept from the FCP down to a lower vertex potential, back past the FCP to a selected upper vertex potential and then back to the FCP. The magnitude of the lower vertex potential was selected to insure that the hydrogen evolution reaction would be the dominant reaction. The magnitude of the upper vertex potential was selected to be high enough so that either pitting or oxygen evolution would be the primary source of current. Scans were also performed at the rate of 1 mV/s in order to resolve any possible features not observed at the higher scan rates. The method used for the 1 mV/s scans differed slightly from the previous scans in that the system was allowed to return to the steady state potential between the cathodic and anodic polarizations. A plot was then constructed from the two data segments.

The cyclic voltammetry was conducted in a manner very similar to the one outlined for the potentiodynamic polarization experiments. The main difference being the potential was scanned between two extreme values five consecutive times without any interruption. The primary purpose of these measurements was to reveal the nature of any electrode reactions (either completely reversible or quasi-reversible) or reactions with adsorbed species that may have occurred with the ions present in this solution.

The electrochemical impedance spectroscopy analysis (EIS) used electrodes and electrochemical cells of the same form previously described. In these experiments, a corroding electrode is subjected to an alternating, small-amplitude perturbation of varying frequency and the basis of the measurement is the response of the electrode to that perturbation. The time-dependent current response of an electrode surface to the sinusoidally alternating potential signal is expressed as an angular frequency dependent impedance. This technique can be used to reveal a variety of parameters for a corroding system, but in this case, it was primarily used to approximate the corrosion rate of each alloy in the white water. Detailed descriptions of the applications of this technique as well as the actual elements used are outside the scope of this report, but numerous sources can be found in the literature [13, 14, 45].

2.3 Scratch-Repassivation Tests

These tests were designed to evaluate the behavior of the two duplex alloys after the passive film has been ruptured by either a chemical or mechanical means. The rate of film restoration often determines the resistance of an alloy to different forms of localized corrosion, namely crevice corrosion, pitting and stress corrosion cracking because these particular forms of corrosion generally depend on the reactions that occur when the bare metal is exposed to the environment [14, 17, 18, 21, 46]. The scratch-repassivation technique has been employed in numerous investigations as a means of evaluating the characteristics of film restoration on a variety of materials [17, 18, 38, 46, 47]. All of the different techniques implemented for these evaluations are designed to rapidly generate a bare metal surface and record the corresponding electrochemical reactions.

Thin sheet samples approximately 0.5 mm thick were cut and mounted in epoxy with the scratching direction positioned to be perpendicular to the plane of the sheet. As before, a conductive epoxy was used to attach a wire to the back of the sample to make electrical contact. The wire and conductive epoxy were completely shielded from the test solution by the epoxy mount and a PTFE sleeve. Prior to testing, the electrodes were polished to a 1 μm diamond surface after which, they were coated with a thin layer of stop-off lacquer to minimize errors resulting from the capacitance effects of the electrode/solution interface.

The electrode holder used for these experiments was designed to minimize experiment-to-experiment variations in the sample location, scratch dynamics and exposed metal surface to electrode potential drop, and is shown in Figure 5. The rationale behind the electrochemical system design for these experiments, the calibration procedures, and the resolution of the inherent measurement problems associated with the technique are described in greater detail elsewhere [46]. It was decided that small, but reproducible, errors in the measurement were acceptable when compared to the efforts required to minimize those errors so, the two Luggin capillary design shown in the figure was implemented [46].

The system used to evaluate the repassivation behavior of the duplex stainless alloys is shown schematically in Figure 6. The procedure consisted of placing the electrode in the holder, attaching the appropriate potentiostat leads, raising the beaker containing the solution to immerse the electrode, positioning the sapphire scribe on the epoxy above the sample, setting the oscilloscope trigger, and then releasing a 1 kg stainless steel weight from a height of approximately 0.1 m above the end of the rod which holds the sapphire scribe. The contact between the weight and the scratch rod triggers the oscilloscope and drives the sapphire tip across the sample at a velocity of on the order of 1 m/s. The sapphire tip was placed in the epoxy of the mount above the sample so that the tip would be accelerated to the scratching velocity prior to reaching the sample and thin samples were used to ensure that the sapphire tip would be well past the sample before decelerating. Based on these precautions, it is reasonable to assume that the velocity of the sapphire scratch tip was constant for the duration of the scratch. The oscilloscope was set to record either potential for open circuit experiments or current for potentiostatic experiments. The time between the initial impact of the weight with the scratch rod and the point where the scribe enters the metal as well as the point where the scribe completes its traverse of the sample are clearly indicated in the oscilloscope trace.

2.4 Stress Corrosion Cracking Susceptibility Tests

These tests were designed to evaluate the stress corrosion cracking and hydrogen embrittlement resistances of the two Sandusky duplex stainless steel alloys in the simulated deinked white water paper making solution. An unambiguous evaluation of the hydrogen sensitivity required a series of mechanical tests conducted at fixed and reproducible hydrogen activities. The slow strain rate (SSR) tensile test technique was selected for this purpose because a) the hydrogen embrittlement process is strain rate dependant, b) the activity of hydrogen on the surface of the samples can be held constant through the use of closed loop control of the potential difference between the sample and a reference electrode, and c) this technique is designed to generate intrinsic mechanical properties data for a given alloy while revealing any interactions that may have occurred between that alloy and the testing environment within a relatively short time frame [24, 48, 49].

The SSR tensile tests were used to evaluate both the mechanical properties of the two alloys in an inert environment and the change in those properties resulting from environmental interactions (i.e., anodic dissolution, FIC or HE) or hydrogen provided by electrochemical reactions on the surface. The intrinsic mechanical properties were determined by conducting SSR tests in dry nitrogen gas on samples which had been stored in a vacuum at room temperature for more than sixty days prior to testing. The simulated deinked newsprint solution was selected for the hydrogen source instead of the more classic, highly buffered solution with a hydrogen recombination poison because the white water was more representative of the aqueous environment that would be commonly encountered in service. The test vessel used for these experiments consisted of a 250 ml double walled glass cell and is shown schematically in Figure 7. This cell was connected to a recirculating constant temperature bath which enabled control of the solution temperature to within ± 1.0 °C. For the constant potential (hydrogen fugacity) experiments, the potential of the sample was measured against a saturated calomel reference electrode ($0\ V_{SCE} = 0.242\ V_{SHE}$) and controlled with a commercial potentiostat. The mechanical tests were conducted using a computer controlled slow strain rate testing system which operated at a constant cross head speed of 0.025 µm/sec (1 x10-6 in/sec). The computer system was configured to record applied load, cross head displacement, elapsed time and either electrode potential or current depending on the particular experiment.

Five samples of each duplex alloy were machined with the tensile axis parallel to the long axis of centrifugally cast suction roll shell as shown in Figure 8. The sample preparation for all of the tensile tests consisted of mechanically polishing the gauge section to a 6 µm diamond finish, according to standard metallographic procedures, followed by a thorough measurement of the relevant specimen parameters. The remainder of the sample was coated with a stop-off lacquer to limit the surface area exposed to the environment. One sample of each alloy was tested in an inert environment to determine the baseline behavior. The remaining samples were tested in the deinked white water under both free corrosion and potentiostatically controlled conditions. After failure, the samples were promptly removed from the cell, rinsed in flowing water and alcohol, dried and then stored in a vacuum desiccator until analyzed.

The fracture surfaces were cut from the broken SSR samples and prepared for analysis. The influence of the deinked white water on the ductility of the alloys was determined from reduction in area (RA) measurements performed on the fracture surfaces with a optical measuring microscope with a ± 0.5 x10-6 m resolution. Scanning electron microscopy was performed on the samples to verify the presence of environmentally induced cracking. The results of these experiments were used to assess the susceptibility for failure by stress corrosion cracking and/or hydrogen embrittlement of both alloys in the deinked white water.

3. Results

3.1 Metallography

Figures 9a and 9b are representative micrographs showing the duplex microstructure of alloys 75 and 86 respectively. In both of these figures, the sample has been etched with Viella's etch which reveals austenite (gamma) as the white constituent and ferrite (alpha) as the darker constituent. The "black" constituent present in both figures is a similar two-phase microstructure on a much finer scale. The microstructure present in both of the duplex alloys is essentially composed of austenite pools surrounded by a ferrite matrix and the ratio of austenite to ferrite is approximately one to one.

Compositional analyses were performed on the alloys to assess any differences between the two phases present. Figure 10 is a backscattered scanning electron (BSE) micrograph of Alloy 86 which shows the bright phase as gamma and the dark as alpha. Figure 11a is also a BSE image, but it has been optimized for compositional analysis by x-ray energy dispersion spectroscopy (EDS). The composition of the line indicated in this figure is presented in Figure 11b. The EDS analysis of this line revealed that the copper is only present in the white regions intersected by the line (the gamma phase). According to the literature, solubility of copper is negligible in the alpha phase (BCC) and approximately 2% in gamma (FCC) [50]. From this, the numerous copper-rich precipitates observed along the interphase boundaries shown in the figure were assumed to be the result of segregation from the alpha to the gamma during solidification.

3.2 Electrochemical Analyses

The free corrosion behaviors of both duplex alloys were measured for 24 hour periods in aerated, simulated deinked white water at 50 °C. The behaviors were also measured in similar aerated solutions containing chloride and no thiosulfate, and thiosulfate and no chloride (as shown in Table 3), in order to reveal any differences in the behavior caused by the individual ionic species. The free corrosion potentials in each solution are shown for Alloy 75 in Figure 12 and for Alloy 86 in Figure 13. Free corrosion measurements were conducted in both aerated and deaerated solutions. Since the service environment is open, and therefore aerated, the results from the aerated experiments are more representative of the service conditions and are shown in this report.

Potentiodynamic scans were conducted on both alloys. Figure 14 is a comparison of the electrochemical behaviors of the two alloys in the white water at 50 °C at a potential scan rate of 5 mV/s. This figure shows that the cathodic behaviors of the two alloys are essentially the same, but it also illustrates the marked differences observed in the anodic behaviors. In this figure, the passivity of Alloy 75 shows signs of passivity breakdown near 0 V_{SCE} with the onset of pitting occurring at approximately +0.100 V_{SCE}, whereas Alloy 86 demonstrates passivity over a substantially wider potential range. The potentiodynamic scans were repeated at a scan rate of 1 mV/s to reveal greater detail and subtle differences in the behavior of these alloys can be seen in Figures 15 and 16.

A baseline evaluation of the influence of the individual ionic species on the electrochemical behavior was performed with a series of potentiodynamic scans in solutions having the same composition as those used for the free corrosion potential measurements. These experiments were conducted in deaerated solutions in order to maximize the resolution of any reactions with environmental species other than oxygen. Figure 17 shows that the electrochemical behavior of Alloy 75 remains essentially the same regardless of the ionic species present in the solution. Small changes in the transpassive behavior are noticeable, but were considered negligible for this investigation. The behavior of Alloy 86, shown in Figure 18, appears to be more sensitive to the ions present in solution. In this figure, the solution containing both thiosulfate and chloride ions appears to have the most influence on the behavior which supports the hypothesis of a synergistic interaction between these two ions as postulated in the literature.

Additional information about the chemical reactions that occur in a given solution can be gained through the use of cyclic voltammetry (CV). This technique is very similar to the potentiodynamic scan except that, the potential is scanned at a much faster rate and is cycled without interruption until steady state is reached. In the first set of CV experiments, platinum electrodes were used because platinum provides an ideal catalytic electrode surface which enables this technique to reveal the maximum information about the reactions that can occur in these solutions. Figure 19 shows an overview of the reactions that occur on a platinum electrode in each of the three white water solutions. Figure 20 shows the same results over a smaller current range. This figure reveals that, the solutions which contain the thiosulfate ion show a peak at approximately +0.900 V_{SCE} whereas the solution which does not contain the thiosulfate shows a smaller peak at approximately -0.250 V_{SCE}. According to the E-pH diagram shown in Figure 4, these peaks are in the appropriate ranges for the oxidation of thiosulfate to sulfite (SO_3^{-2}) and the reduction of HS- to thiosulfate respectively.

Figures 21 and 22 are the results of CV experiments conducted on Alloy 75 and Alloy 86 respectively. These measurements were used to evaluate the rates of the reactions observed on the platinum electrodes on the Sandusky alloys. The behavior of the Alloy 75 is essentially the same in all three solutions. The magnitude of the peak exhibited by the Alloy 75 at approximately -0.400 V_{SCE} is slightly greater in the deaerated, deinked white water then in other solutions, which would be consistent with an interaction between the thiosulfate and chloride. In contrast, the behavior of the Alloy 86, does exhibit noticeable differences in each of the three solutions. Peaks occur in all solutions at approximately -0.200 V_{SCE}, but the magnitude is noticeably greater in the standard deinked white water which again supports the postulated interaction between the thiosulfate and chloride ions. However, the solution with no chloride exhibits a second peak at approximately +0.300 V_{SCE} which is not present in either of the other solutions. This could be due to either a reaction between the thiosulfate and one of the constituents in the alloy or to the suppression of a reaction by the chloride ion in the other solutions.

The better resistance to pitting observed in the Alloy 86 has been attributed to the copper present in that alloy. As a result, CV experiments were also conducted on a pure copper electrode to further evaluate the reactions between this element and the white water solutions. The results of those measurements are shown in Figure 23 and Figure 24. Similar to the observations on the platinum electrode, the solutions containing the thiosulfate ion exhibit different peaks than the solution that does not contain the thiosulfate. In Figure 24, the magnitude of the peak that occurred at approximately -0.800 V_{SCE} is substantially larger in the solutions that contain thiosulfate which again indicates a possible reaction with the thiosulfate ion.

Estimates of the corrosion rates of the alloys in the deinked white water were obtained by electrochemical impedance spectroscopy (EIS) which was used to estimate the polarization resistance. In this technique, the potential of the sample compared to a reference electrode is again controlled by the potentiostat, but in this case, the potential is oscillated about the free corrosion potential in a sinusoidal manner at varying frequencies. A low amplitude sine wave is used for this excitation in order to minimize perturbations to the surface of the sample which could alter the corrosion rate. The impedance of the electrode in the electrolyte is determined from the potential excitation and the current response. The difference between the values where the real component of the frequency approaches infinity and where it approaches zero is used as an estimate of the polarization resistance. The polarization resistance is related to the corrosion rate through the relationship:

$$i_{Corr} = \left(\frac{1}{R_P}\right)\left(\frac{b_A b_C}{b_A + b_C}\right) = \text{Const}\bullet\left(\frac{1}{R_P}\right) \qquad (7)$$

where i_{corr} is the corrosion current density, R_P is the polarization resistance and b_A and b_C are the anodic and cathodic Tafel constants for the alloys in the environment. Since the polarization experiments above indicate that the Tafel slopes for these two alloys in this environment are essentially the same, this relationship indicates that the corrosion rates can be compared by comparing the polarization resistances or admittances directly. Figures 25 and 26 are Nyquist plots of the real versus the imaginary components of the impedance data. In this type of plot, a semi-circle or semi-ellipse results with the high frequency data points near the origin and the low frequency data points out where the semi-ellipse returns to the real axis. The polarization resistance is estimated as the major axis of this semi-ellipse. Figures 25 and 26 show that the corrosion rates of both alloys in this environment are quite low and that the general corrosion rate of Alloy 75 at its free corrosion potential is less than that of Alloy 86 at its free corrosion potential. It should be noted that the free corrosion potential of Alloy 86 is higher and that this could be responsible for the observed difference. The polarization resistance for each alloy was estimated by fitting the data in these figures to an equation for an ellipse. The polarization admittances estimated by the curve fitting routine was 2.83×10^{-7} ohms^{-1} with a standard uncertainty of 0.25×10^{-7} for Alloy 86 and 10.43×10^{-7} ohms^{-1} with a standard uncertainty of 0.17×10^{-7} for Alloy 75. That is, the corrosion rate indicated for Alloy 86 was about 3.5 times that of Alloy 75. The relationships used to determine the uncertainties for these measurements can be found in the NIST standard guidelines [51]. Another technique used to estimate polarization resistances from EIS data is the Bode plot where the modulus of the impedance is plotted against the frequency and the difference between the high and low frequency plateaus is used as an estimate of the polarization resistance. Figure 27 is a Bode plot for the alloys in deinked white water and the polarization resistances estimated from this figure are similar to those indicated in Figures 25 and 26.

3.3 Scratch Repassivation Experiments

The electrochemical transients produced by a scratch repassivation experiment reveal information about the general characteristics of passive film repair after a film rupture event. Under free corrosion conditions, this technique reveals both the range of potentials that can occur for the unfilmed metal (E_{min}) and the rate of film restoration (dE/dt) under natural conditions. Scratch experiments conducted under controlled potential conditions determine the metal dissolution rate and the maximum rate of film restoration. During any film rupture event, the minimum, or bare surface electrode potential may be significantly different from the normal free corrosion potential. This minimum potential may also exceed the equilibrium potential for hydrogen in the solution and thereby stimulate the hydrogen evolution process. The equilibrium fugacity of hydrogen generated will vary with electrode potential and solution pH according to the Nernst equation:

$$E\left(V_{SHE}\right) = \frac{RT}{F} \ln \left\{ \frac{[H^+]}{[H_2]^{0.5}} \right\} \tag{8}$$

Where $E(V_{SHE})$ is the potential measured with respect to a hydrogen electrode, R is the gas constant, F is the Faraday constant, T is the absolute temperature and the bracketed quantities are the activities. Substituting a temperature of 298 K into this equation, the relationship between electrode potential (versus a calomel electrode), hydrogen fugacity and solution pH becomes: [52]

$$E\left(V_{SCE}\right) = -0.242 - 0.0296\left\{\log\left(P_{H2}\right)\right\} - 0.059\,(pH) \qquad (9)$$

This relationship also shows that the hydrogen fugacity at the electrode surface increases by one order of magnitude for each additional 0.059 V_{SHE} decrease in electrode potential.

According to the literature, the nominal pH of a typical deinked white water ranges between approximately 3.5 and 4.0 [53]. Using Equation 8, the resulting approximate hydrogen evolution potential for this solution is on the order of -0.480 V_{SCE}. It is very important to note that Equation 8 assumes equilibrium conditions and under non-equilibrium conditions, such as hydrogen bubbling, the actual hydrogen fugacity calculated from this equation may vary significantly due to localized changes in pH, irreversible losses and mass transport [24].

The typical repassivation behavior observed under open circuit conditions is shown for both alloys in Figure 28. Table 4 shows the minimum potential (E_{min}), the maximum rate of potential change during repassivation (dE/dt_{max}), and the averages and the standard deviations for both quantities. The results of a statistical evaluation are also presented in this table. The average minimum potential was approximately -0.700 V_{SCE} ± 0.100 V_{SCE} for Alloy 75 and approximately -0.610 V_{SCE} ± 0.200 V_{SCE} for the Alloy 86. The repassivation rates were more scattered, 81.5 V/s ± 61 V/s for the Alloy 75 and 64.3 V/s ± 76 V/s for the Alloy 86. Compared to similar experiments conducted on other materials,[46, 52] the scatter in the repassivation rate measurements seem to be rather widespread, but considering the complex microstructures present in each alloy and the low electrical conductivity of the white water solution, these values are not unreasonable. It is possible that the relatively large standard deviations are due to large variations in the repassivation process caused by the duplex microstructure, but it is more likely that they are produced by measurement errors resulting from the low conductivity of the test solution. The most significant result of these measurements, as exhibited in Figure 28, is the minimum potential produced for both alloys during a film rupture event at a crack tip may indeed drop below the potential required for hydrogen evolution. Therefore, this result indicates that it is possible for hydrogen to be produced at the tip of a crack during cyclic loading and that hydrogen cracking could occur in either alloy if the microstructure is susceptible at this level of hydrogen. As shown in Figure 29, the minimum bare surface potential does, indeed, go below the hydrogen evolution potential in the deinked white water for both alloys. This figure also indicates that the hydrogen fugacity at the minimum bare surface potential may be sufficient to support a hydrogen embrittlement mechanism in either of these alloys. However, there is no statistically significant difference in the behavior of the two alloys.

The repassivation rate was evaluated for both alloys under potentiostatically controlled conditions at -0.300 V_{SCE}. The data for the controlled potential experiments is presented in Table 5. The primary parameters used to analyze these scratches are: the total elapsed time, t, the bare surface current density, i(B), the time at peak current, t(B), and a fitting parameter, n. Typical transients are shown for both alloys in Figure 29. Both the magnitude of the peak and the rate of decay of the transients shown in this figure are very similar for the two alloys. These measurements indicate that the rate of film restoration after a film rupture event is approximately the same for both alloys in the white water solution.

3.4 Stress Corrosion Cracking Evaluation

The literature describes several test methods to evaluate SCC susceptibility (e.g., direct tension) [54], but in general, these test methods are designed around a fixed, initial stress or stress intensity which could be below the critical stress intensity required for crack propagation (i.e., K_{Iscc}). In contrast, the SSR technique is designed around a constantly increasing strain which produces increasing stress and stress intensities. This technique also generates a failure in each test, with or without the presence of SCC, and as a result, will always provide a numerical value which can be used to evaluate the relative performance in any alloy/environment combination [48]. Even though the SSR technique has proven as reliable as any other testing technique for assessing the SCC or hydrogen embrittlement susceptibility, there are limitations to the technique [55]. Since the constant loading and straining conditions of the SSR technique represent loading conditions that are more severe than most applications, this testing technique also tends to be more severe and most of the reported errors pertain to the indication of environmental cracking when none is observed in service (i.e., false positives). On the other hand, incidents of cracking occasionally occur in service when none was indicated in SSR tests (i.e., false negatives) but, most of these have been attributed to the SSR test environment failing to accurately reflect the actual service environment conditions or strain rates that are too high for the operating cracking mechanism [55]. Also crevices, as well as effects caused by the constant straining process, may induce localized changes in the environment and the surface potential of the sample in service which may differ significantly from that of the sample in the SSR test.

The results of the slow strain rate tests conducted in aerated, deinked white water at 50 °C are presented for Alloys 75 and 86 in Tables 6a and 6b respectively. These results of these experiments show variations in all three quantities as a function of the applied potential for both alloys which suggest that the white water did have some influence on the mechanical properties. The mechanical data for each alloy were then ratioed to the values obtained in the reference environment (dry nitrogen) and plotted against the electrode potential. These data are shown in Tables 7a and 7b.

In general, if a material is susceptible to any form of environmentally induced failure, it will result in significant changes in either or both of the two basic parameters measured by a slow strain rate tensile test: the ultimate tensile strength (UTS), and the ductility. The UTS is determined from the maximum applied load and the ductility is commonly determined by two parameters, the engineering strain to failure (STF) and the reduction in area (RA) [33].

The UTS is a measurement of the fracture strength of an alloy and a noticeable change should be exhibited in this parameter if some environmental interaction occurs that promotes crack initiation and propagation at some critical value of stress. In many cases however, the ductility data are better indicators of environmental interactions than the UTS data. In general, environmental cracking mechanisms, such as anodic slip dissolution, depend more upon critical values of plastic strain rather than stress. Therefore, when cracking does occur by one of these mechanisms, it is normally reflected in the ductility data. It should be noted that the STF values shown in Table 6 were calculated from load frame displacement measurements taken by a linear variable displacement transducer (LVDT) positioned outside of the cell during the experiment. As a result, this measurement includes both the elastic and plastic components of the deformation measured to induce failure. Ductility data of this type should not be used as the sole basis for engineering calculations because it is subject to greater experimental error [33].

The second measurement of the ductility, the RA value, is determined by a physical measurement of the fracture surface at the completion of the tensile test. Unlike the STF, the RA measurement is based purely on the plastic component of the deformation required for failure and, as a result, the RA is generally a better means to determine an environmental interaction for engineering alloys that demonstrate appreciable ductility [33].

The reduction in area (RA) data are plotted in Figure 30. As expected, the minimum reduction in area for Alloy 75 occurred at the lowest potential (-0.850 V_{SCE}) which is to the left (i.e., below) the hydrogen evolution line present in the figure. In the case of Alloy 86, the minimum RA value occurred at the same potential where pitting was observed (+0.850 V_{SCE}).

While noticeable differences are present in the mechanical property data, the limited number of tests makes a proper statistical analysis impossible. However, statistical analyses of slow strain rate data obtained from tests performed on similar alloys indicate that changes greater than approximately 10% in any of the parameters are statistically significant [48]. To compensate for the lack of statistics, a thorough fractographic analysis was performed on each specimen and the results of these analyses were in agreement with the behavior predicted by the literature and the electrochemical evaluations.

The base-line fractographic behavior for both alloys in the inert, reference environment are shown in Figure 31. Both of these micrographs exhibit approximately equal areas of ductile, microvoid coalescence and brittle, transgranular, cleavage-like features which correspond to austenite and ferrite phases respectively. From the amount of cleavage present in these figures, it appears that the ferrite phase exhibited little or no ductile failure in the nitrogen environment at 50 °C. On the other hand, no evidence of brittle failure was present in the austenite phase in either alloy. Based on the SSR data and these figures, it is clear that the ferrite phase was the primary source of strength and the austenite phase was the major source of ductility in both alloys.

The general corrosive attack on the Alloy 75 in the white water is shown in Figure 32. Figure 32a shows the initiation and propagation of a corrosion pit in Alloy 75 tested in the deinked white water at a fixed electrode potential of -0.300 V_{SCE}. As shown in this figure, significant amounts of the austenite phase have been dissolved by the white water solution. This is more apparent in Figure 32b. On the other hand, no evidence of corrosive attack was observed anywhere in the Alloy 86 specimen tested under the same conditions. In fact, the analysis of this fracture revealed features very similar to those observed in nitrogen. A representative micrograph of the Alloy 86 fracture surface is shown in Figure 33. The behavior of Alloy 75 tested under cathodic protection conditions was very similar to that observed in nitrogen. No distinguishable evidence of corrosion was present and the austenite exhibited mostly ductile features thereby indicating little or no effect of hydrogen. A representative micrograph of the behavior under cathodic protection is presented in Figure 34. Alloy 86 was tested at a potential near the pitting potential observed in the potentiodynamic scans. At this potential, the behavior of Alloy 86 was quite similar to that observed for Alloy 75 tested at -0.300 V_{SCE}. Evidence of deep pitting attack was present in several locations on the fracture surface. Figures 35a and 35b show areas of selectively dissolved austenite surrounded by cleaved ferrite.

A section of an Alloy 75 service failure was provided for analysis by Sandusky International. A low magnification overview of the fracture surface is shown in Figure 36. This figure shows an array of drilled holes surrounded by fractured metal ligaments. This morphology is consistent with the descriptions of the service failures found in the literature. Optical microscopy revealed evidence of fatigue cracking but a significant amount of the fracture surface was covered with a thick black film making further evaluation difficult. A small section of the failure was cut and cleaned for analysis in the SEM. The analyzed specimen was cut from the area of highest tensile stress (i.e., the internal surface of the shell as indicated in Figure 36) as the failure most likely initiated in this region of the component. Figure 37 is a representative micrograph showing several fatigue cracks initiating at base of very small pits. The morphology of the striations is consistent with those normally observed in Stage I crack initiation. Stage II striations were observed further into the specimen.

4. Discussion of Results

The basic issue addressed by this research was, why do corrosion fatigue measurements indicate that Alloy 75 and Alloy 86 should have similar performance in service when service experience indicates very different behavior? At the outset of this work, Sandusky International was making suction roll shells out of two alloys with very similar compositions (Table 1) and mechanical properties (Table 2). Corrosion fatigue (S-N) and corrosion fatigue crack propagation (da/dN-ΔK) measurements had been conducted on these alloys by Sandusky [53, 56] and others [2, 4, 7] and the performance predictions based on these measurements indicated that these alloys should have virtually identical behavior in service. However, Sandusky has not yet observed a service failure with Alloy 86 while failures of Alloy 75 occur on a periodic basis. That is, the real objective of this research was to determine the source of the discrepancy between the performance predicted by these measurements and that observed in service.

There are two fundamentally different possibilities for the origin of this discrepancy. First, there could be something wrong with the measurement methods used to obtain the data for the performance prediction models. That is, the measurements may have been conducted under environmental or loading conditions that are not entirely representative of that present in service, or they may have had insufficient resolution. Second, the data could be accurate and representative, but the performance prediction model(s) may overlook a causative factor in the failure process. In general, performance prediction models assume a failure process and estimate the time to failure by estimating the time for each step in the sequence required for the failure process. If some alternative process bypasses one of the steps in this sequence, then failure will occur more quickly. If the bypassed step is lifetime defining (failure limiting), then failures can be induced when none would occur when this step cannot be bypassed. Put in the simplest terms, the measurements may be correct and may accurately represent the rates of the processes measured as they occur in service, but we may be measuring the wrong things and ignoring the process that is actually inducing the failures.

The possibility that there may be something wrong with the measurements was examined first. Examination of the literature on corrosion fatigue indicates that there are a large number of metallurgical, loading, and environmental parameters that influence crack propagation rates [27, 28, 57, 58]. For the two alloys in this application, most of these parameters are changed very little, if at all, or should have been revealed by the measurements conducted previously if they influenced fatigue crack propagation rates significantly. Therefore, the loading frequency is the most potentially significant difference between the testing conditions and the service conditions. In service, suction roll shells are operated at rotational speeds which generate maximum loading frequencies on the order of 25 to 30 Hz. On the other hand, corrosion fatigue tests are typically conducted at frequencies determined by the testing equipment (nominally 10 to 20 Hz). As a result, experiments were conducted to determine if there is sufficient reason to postulate a significant difference in the frequency effect on corrosion fatigue for these two alloys.

As discussed in the introduction, each corrosion fatigue crack extension event will generate a current transient as the passive film is restored on the surface of the bare metal. The amount of current required to repassivate the bare surface is proportional to the area under the transients shown in Figure 3. As a result, the total current required for repassivation can be approximated through the use of a scratch repassivation experiment and a model that integrates the resulting current transient such as the one shown in Equation 6 [34]. The information gained from this technique may then be used to predict the influence of frequency on the rate of crack extension.

The potential influence of test frequency on crack propagation rates was examined using scratch repassivation experiments. In order to properly evaluate whether dissolution based cracking mechanisms are active in these alloys in service, the testing frequency should lie within the range of frequencies relevant to the conditions in service. Therefore a series of scratch experiments was conducted at constant electrode potentials that were representative of the corrosion conditions in service. The results of this examination were used to determine both the dissolution and film restoration rates for these alloys in the simulated paper making environment.

According to the literature, the operational frequencies of paper machines are generally determined by the type of paper produced. That is, machines which produce less dense papers, such as tissues, tend to run at much higher rotational speeds than those used to produce writing papers [56]. The high end of these operational frequencies is on the order of 1700 rpm to 1800 rpm (≈ 30 Hz). In Figure 29, the elapsed time required for effectively complete repassivation in both alloys is on the order of 0.01 seconds. This time interval corresponds to a cyclic frequency of approximately 100 Hz. Due to the limitations of most testing equipment, crack propagation experiments are difficult to perform at cyclic frequencies of this magnitude. Figure 29 also illustrates that the repassivation rates for both alloys are essentially the same. This indicates that the amount of metal lost to anodic reactions during film rupture would be virtually the same in either alloy regardless of the cyclic frequency used in a crack propagation experiment. Therefore, it was concluded that there is no anodic dissolution basis for postulating that the observed differences in the behavior of the alloys is due to a frequency effect on the crack propagation rates.

Hydrogen related mechanisms were considered next because the alloys may possibly possess differences in the rates of the solid state diffusion processes required for hydrogen transport. The possibility of hydrogen embrittlement was evaluated through two experimental techniques. First, scratch repassivation measurements were conducted under free corrosion (open circuit) conditions to determine whether hydrogen evolution was possible during a film rupture event produced during a load cycle and if so, was there a significant difference between the two alloys. Second, the relative sensitivity of each alloy to hydrogen embrittlement was determined by the slow strain rate tensile tests.

The SSR experiments were conducted in both a nitrogen reference environment and in the simulated white water under conditions of controlled electrode potentials (hydrogen fugacities). The values for the controlled potential experiments were determined from the scratch test results and Equation 8. The potentials selected for this evaluation were -0.600 V_{SCE}, because it was in a range where the anodic dissolution of the specimen was minimized, but also low enough to evolve hydrogen on the specimen surface, and -0.850 V_{SCE}, because it was low enough to generate a relatively high hydrogen fugacity while maintaining a minimal rate of bubbling at the surface of the electrode. Assuming thermodynamic equilibrium conditions, the corresponding hydrogen fugacities at these potentials in this solution are 6.69×10^{2} MPa (6.6×10^{3} atm) and 3.75×10^{11} MPa (3.7×10^{12} atm) respectively.

The fractographic analysis of the specimens tested at -0.600 V_{SCE} showed no distinguishable evidence of anodic attack in the austenite regions and little or no change in the appearance of the ferrite. These results were in agreement with the mechanical data in that there was good retention of strength, although the ductility was somewhat lower than the value obtained in nitrogen. The mechanical data indicate also that Alloy 86 was cathodically protected at this potential. The reduction in area measured for Alloy 75 tested at -0.850 V_{SCE} revealed a 1.13 percent decrease from the value recorded at -0.600 V_{SCE}. This further decrease in ductility implies that the Alloy 75 may have a slight sensitivity to hydrogen but, it is not large enough to adequately explain the differences in the behavior of the alloys reported in service. The fractographic analysis also revealed no distinct differences in the fracture morphology from those observed at -0.600 V_{SCE}. The results of the hydrogen sensitivity evaluations demonstrate that hydrogen evolution is possible in the simulated paper making environment but neither alloy is embrittled at these hydrogen fugacities.

The evaluation of the first hypothesis revealed no reasonable expectation that a modification in one of the experimental parameters used to predict crack propagation would reveal a significant difference in the behaviors of these two duplex alloys. As a result, it was necessary to determine if there was a process that could be inducing fatigue failure in one alloy, but not in the other. In corrosion fatigue, crack initiation is often the result of pitting, stress corrosion cracking or intergranular corrosion. Therefore, evaluating the second hypothesis required a detailed study of the corrosion behavior of the two duplex alloys in the white water environment.

Since corrosion fatigue cracks frequently initiate at the base of pits, the first parameter evaluated was the pitting behavior, and it was evaluated under free corrosion conditions. In general, the free corrosion behavior is determined by the amount of oxidizers in the environment and the corrosion resistance of the alloy. As shown in the open circuit potential measurements, Figures 12 and 13, both alloys exhibited relatively good overall resistance to the simulated deinked white water solutions, but the Alloy 86 consistently exhibited better resistance to pitting than the Alloy 75. Because the two alloys have essentially identical compositions, except for one element, copper, the greater pitting resistance observed in the Alloy 86 is almost certainly due to the influence of the copper in this alloy although the literature on pitting in stainless steels is inconclusive about the beneficial effects of copper additions [19, 59]. Under free corrosion conditions in the standard aerated, deinked white water, Alloy 75 consistently exhibited evidence of pitting attack whereas Alloy 86 generally exhibited little or no evidence of pitting under the same conditions. Also, the pitting in Alloy 75 was primarily located along the austenite/ferrite interphase interfaces, although some pitting was observed in the austenite phase. Little or no pitting was observed in the ferrite phase. Some pitting was observed in Alloy 86 after 24 hours in the simulated white water, but compared to the Alloy 75 under the same conditions, the pits (as measured with a digital micrometer) in the Alloy 86 samples were shallower and generally limited to the regions along the interphase interfaces. These pits could be produced by variations in the passive film in the regions of the interphase interfaces resulting from alloying element segregation. It is also possible that, pitting of this type could be an indication of some form of chromium depletion and/or sensitization along the interphase regions.

Variations in the electrochemical behavior were also observed in the potentiodynamic scans performed in the deinked white water. The results of these measurements showed that the pitting potential occurs at or near the free corrosion potential for the Alloy 75 in the aerated white water. In the case of Alloy 86, the potentiodynamic scans, shown in Figure 14, reflected stable passivity over a much wider range of potentials. In this figure, Alloy 75 exhibits the onset of transpassive behavior between -0.200 and -0.050 V_{SCE}. This is the same approximate range for the free corrosion potential for this alloy in the aerated solution.

The interactions between the ionic species and the Alloy 86 during the potentiodynamic scans are illustrated in Figure 18. The changes in the potential and current associated with the peaks shown in this figure were attributed to the effects of the individual ionic species in the test solution. The largest apparent influence occurs in the standard white water solution (i.e., sulfate, chloride, and thiosulfate) which, again, is consistent with the synergy proposed between the chloride and thiosulfate ions discussed in the introduction. The interactions between the Alloy 86 and the individual solutions containing just thiosulfate, or chloride were not as pronounced although some variations in the current and potential were present. In contrast, the behavior of the Alloy 75 was essentially the same for all three environments. Some statistical scatter is present, but no real discernable differences are observable in Figure 17. The differences in the interactions observed between the Alloy 86 and the three white water solutions is almost certainly the result of the copper present in this alloy.

Figures 21 and 22 show the behavior of the two alloys in a linear format because the interactions between the ions present in the standard white water solution and the test alloy are more apparent. The behavior of Alloy 75 in the two partial solutions is effectively the same which is in agreement with the behavior observed in the previous experiment. However, the linear format does show the behavior of the Alloy 86 to be a bit different. As shown earlier, the maximum interaction between the ions and the Alloy 86 was observed in the complete solution, but the behaviors in the partial solutions are distinctly different. The peak present at approximately +0.250 V_{SCE} in the white water-minus chloride solution does not appear in other scans performed on either alloy. The E-pH diagram constructed from the available thermodynamic data, (Figure 4) and the CV's performed on platinum and pure copper electrodes (Figures 20 and 24 respectively) both indicate that this peak is in an appropriate potential range for a change in the ionic state of the thiosulfate ion. It is possible that, in the standard white water solution, this reaction either does not occur or it is suppressed somehow by the interaction between the chloride and thiosulfate ions. Considering that copper is the only appreciable compositional difference between the two alloys, this peak implies either a singular interaction is occurring between the copper and a specific oxidation state of the sulfur in the solution, or that a reaction was catalyzed by the small copper-rich particles present along the interphase interfaces (shown in Figure 11).

It is also possible that the better performance of the Alloy 86 is due to the fact that Alloy 86 has a slightly faster corrosion rate than Alloy 75. The corrosion rates for both alloys in the simulated deinked white water were estimated from data obtained under free corrosion conditions using Electrochemical Impedance Spectroscopy (EIS). As shown in Figures 25 and 26, the estimated overall corrosion rates were very low for both alloys in this solution, however, the EIS measurements did reveal that the corrosion rate of the Alloy 86 was higher than the corrosion rate for Alloy 75. According to the literature, the resistance to pitting tends to be better in alloys which possess relatively low or moderate free corrosion rates because higher corrosion rates increase the potential for localized attack. The Alloy 86 exhibited a lesser tendency toward pitting attack in the white water under free corrosion conditions although the corrosion rate, as estimated by the EIS, was approximately a factor of five higher than the corrosion rate for the

Alloy 75 which was clearly susceptible to pitting attack under the same conditions. Even though differences in the estimated corrosion rates of both duplex alloys in the white water were observed, the overall rates are quite low for both alloys which implies the differences in the electrochemical behavior between the two alloys must be the result of another influence. The most likely explanation for the higher corrosion rate in Alloy 86 is that the Cu particles observed along the interphase interfaces act as local cathodes, which increase the rate of general corrosion. However, it is also possible that the copper particles accelerate repassivation of sub-critical pit nuclei. That is, if the process to form a pit is similar to a basic nucleation and growth process [60] then sub-critical pit nuclei would continuously form and promptly repassivate. In this case, an alloy with faster cathodic kinetics would repassivate larger pit nuclei thereby keeping them from reaching critical size.

The results of the electrochemical analyses demonstrate that, overall, the electrochemical behaviors of the two alloys in the simulated white water are quite similar. The most noticeable difference in the electrochemical behaviors of the two alloys was that the onset of pitting occurs at a much higher potential in the Alloy 86. In the standard aerated white water, the Alloy 75 showed little or no separation between the pitting potential and the free corrosion potential, but in the Alloy 86, the onset of pitting occurred at a potential approximately 0.800 V higher than the free corrosion potential. The separation between these two potentials is a measure of the energy that the oxidizers present in a solution must supply to induce pitting in an alloy. The results of the electrochemical analyses show that Alloy 86 requires substantially more energy to induce pitting than Alloy 75 in the paper making environment. As a result, a small separation between the free corrosion and pitting potentials indicates a high probability for pitting as the free corrosion potential is a highly variable quantity which fluctuates with changes in the service environment. On the other hand, a wide separation between these two potentials means a much lower probability that pitting will occur in the service environment.

The results of the electrochemical analysis, were the basis of the hypothesis that the difference in service behaviors of these two alloys is primarily due to the pitting resistance of the two alloys. This difference could be due to several factors, but again, the compositions of the two alloys are essentially the same, so it is reasonable to attribute the observed improvement in the pitting resistance to the 2% copper addition in Alloy 86. It is also reasonable to assume that if pitting were to occur in the Alloy 86, the performance of that alloy should be very similar to that of Alloy 75. This hypothesis, that the performance of the alloys in service is determined by the pitting resistance, was evaluated with SSR experiments.

A test was performed at -0.300 V_{SCE} which was designed to emulate the electrochemical conditions created in the region of a small crack in a roll shell made from Alloy 75. In this situation, the capacitance produced by the huge differences in surface areas would, in essence, polarize the region immediately surrounding the crack to the free corrosion potential generated by the large roll shell. The value of the fixed potential for this experiment was determined from polarization data and the actual electrode potential data recorded during a similar SSR experiment performed under free corrosion conditions. Figure 32a is a representative micrograph showing the type of pitting attack observed in both experiments. This figure shows the type of quasicrystallographic attack frequently observed in pitting corrosion. Consistent with the results of the polarization experiments, there is little or no evidence of attack in the ferrite phase whereas austenite in the same region is almost entirely dissolved. This preferential attack is more apparent in Figure 32b which is a micrograph taken in the neighboring region of Figure 35a. The primary feature in this figure is, once again, cleaved ferrite. Little or no austenite is visible in this figure, which is a another strong indication of the preferential attack of this phase by the thiosulfate and chloride ions. Combining the features in this figure with the results of the electrochemical evaluation, it was determined that the white water solution preferentially dissolves the ductile phase (austenite) which generates sharp, stress concentrations along interphase interfaces that promote crack initiation.

An SSR experiment was conducted on Alloy 86, near the pitting potential, in order to evaluate whether or not the results would be similar if pitting were to occur in this alloy. The results of this experiment are shown in Figures 35a and 35b. These figures clearly show evidence of anodic attack in the austenite and little, if any, effect in the ferrite. The pitting shown in Figure 35a has a morphology similar to that observed in the Alloy 75 tested at -0.300 V_{SCE}. In this figure, the austenite is essentially dissolved which resulted in a sponge of brittle ferrite. Figure 35b, shows a similar preferential anodic attack in the austenite to that observed in the Alloy 75 at -0.300 V_{SCE}. In each of the SSR experiments conducted under pitting corrosion conditions, the failure appears to be the result of a reduction in cross sectional area caused by the formation and propagation of pits. As the pit propagated into the tensile specimen, the anodic dissolution of the more ductile phase simultaneously decreased the fracture toughness of the alloy and the cross sectional area. Rapid failure occurred in both alloys when the stress intensity reached the critical value for the alloy. It was determined that once pitting initiated in Alloy 86, the failure mode was identical to that observed in Alloy 75 during free corrosion.

The results of the slow strain rate analyses demonstrated that the fracture resistance of both alloys in the simulated white water environment is determined by the pitting resistance. This implies that fatigue will be similarly influenced and that the failures observed in service occurred by corrosion induced fatigue cracks which initiated at the base of corrosion pits. To further evaluate this possibility, a section of a failed Alloy 75 suction roll shell fracture was examined to determine both the nature of the cracking and the general location of the crack initiation as they occurred in an actual paper making environment. Figure 36 shows a representative configuration of holes and remaining ligaments in the failed roll shell. The general location of the tensile stresses and the surface which was in contact with the paper slurry are also indicated in this figure. A large portion of the surface of this fracture was covered by a tenacious black film which hindered the optical microscopy, but the analysis revealed that a primary crack front was formed by the union of several small cracks which emanated from the inside diameter surface of the roll shell. The crack initiation was further studied with scanning electron microscopy. As shown in Figure 37, the cracks initiated at the base of small corrosion pits. While fatigue cracking is clearly present in this figure, the crack initiation at the base of a corrosion pit is consistent with the results of the SSR analysis. The conclusions drawn from the failure analysis support the hypothesis that pitting resistance is the factor that determines the corrosion fatigue resistance of these alloys in service.

The results of this investigation also support the hypothesis that the resistance to pitting is responsible for the differences in service behavior observed between Alloy 75 and Alloy 86. Other failure mechanisms, such as hydrogen embrittlement, may be possible in these alloys, but the measurements clearly indicate that they are not determining factors in the service behavior. The results of the individual evaluations were all in agreement with this conclusion. They all showed that while both of these duplex alloys have relatively good overall resistance to the simulated white water environment, Alloy 75 consistently exhibited a higher susceptibility to pitting than Alloy 86. The potentiodynamic and cyclic voltammogram data both indicate that the 2% copper addition in the Alloy 86 exerts a noticeable influence on the electrochemical behavior of that alloy which, in turn, enhanced the resistance of that alloy to pitting in the deinked white water environment. Copper has been shown to have a beneficial effect on the general corrosion behavior of iron-based alloys in acidic solutions [61]. In addition to providing a noticeable increase in the separation between the free corrosion and pitting potentials, the copper in the Alloy 86 also appears to stabilize the passive behavior over a wider range of potentials. Both of these factors appear to be responsible for the substantially reduced susceptibility to pitting in Alloy 86.

These results were obtained under controlled laboratory conditions and do not attempt to address the role of biologicals in the corrosion process. The range of operational temperatures and the composition of the solutions in the papermaking process are known to support the growth of bacterial and in turn, promote the formation of bio-films which may influence the behavior of the alloys in service. In general, the nature and concentration of these species can vary widely between individual paper mills which make it virtually impossible to reproduce the conditions on a laboratory scale.

The objective of this work was to help Sandusky International prevent fatigue failures in suction roll shells. Initially, it was thought that this objective could be accomplished through the development of better methods for measuring fatigue crack propagation at or near the long crack propagation threshold with higher resolution of small crack propagation rates and investigating frequency effects. The first step taken to accomplish this objective was to determine the causative factors in the fatigue failures to insure that this research would be relevant to the failure processes occurring in service. The results of this examination demonstrated that the existing measurement methods and data failed to predict failure in Alloy 75 not because of a lack of resolution, but due to the fact that by measuring the fatigue crack propagation thresholds for long cracks, one was overlooking the failure mechanism which was the initiation and propagation of small cracks from the pits that form in Alloy 75.

Figure 38 is a Kitagawa diagram which illustrates the relationship between the fatigue behavior observed in S-N type fatigue tests and fatigue crack propagation threshold measurements [62]. Kitagawa showed that as the crack or flaw size in samples became smaller that the cyclic stress required to propagate a crack and cause fatigue failure increased according to the relationship:

$$\Delta\sigma = \frac{\Delta K_{th}}{Y\sqrt{\pi a}} \tag{10}$$

where ΔK_{th} is the crack propagation threshold stress intensity, a is the flaw or crack size, and Y is a geometric factor. However, as the flaw size decreased and the cyclic stress approached the fatigue limit observed in S-N fatigue tests, Kitagawa found that the stress no longer followed this relationship instead, it asymptotically approached the fatigue limit observed during tests on initially smooth samples. Figure 38 reveals that for small flaws, the fatigue limit (the horizontal line labeled "A" in this figure) determines whether or not failure will occur, and for larger flaws, it is the threshold stress intensity (the line with a slope of -1/2 labeled "B" in the figure) that determines fatigue failure. The point where these two line cross (labeled "C" in the figure) is the boundary between "long crack behavior" and "short crack behavior." As shown in Figure 38, this approach basically divides fatigue behavior into four classifications: 1) A region below the S-N fatigue limit where the surface flaws and cracks are too small to produce stress intensities that exceed the fatigue threshold, 2) A region above the S-N fatigue limit and where flaws produce stress intensities greater than the threshold so that both short crack and long crack fatigue analyses will predict failure, 3) A region below the S-N fatigue limit, but to the right of the threshold stress intensity line, where the stress intensities at the flaws are sufficient to cause crack propagation. In this region, fatigue failures could occur in service even though S-N fatigue tests may predict otherwise and 4) A region below and to the left of the threshold stress intensity line, but above the S-N fatigue limit. In this region, the threshold stress intensity will not predict failure, but short cracks will propagate because the cyclic stress is above the fatigue limit.

At the onset of this study, it was thought that the situation was one where the long crack threshold stress intensity was being reduced more in Alloy 75 than in Alloy 86 and it was postulated that previous investigators misjudged the extent of the shift in Alloy 75 due to a loading frequency effect. Based on the results of this study, it has now clear that the existing techniques, measurements, and data are characterizing the "long crack" behavior of these alloys sufficiently. That leaves two possible causes for the fatigue failure in Alloy 75 in service. Either the "short crack" (S-N) fatigue limit is being reduced in this alloy to the point where short cracks can propagate under the service stresses (i.e., line A is reduced in Alloy 75 resulting in a transition from region 1 to region 4 behavior in Figure 38) or the pits in this alloy are growing to the extent that they generate flaws of sufficient magnitude that the stress intensity at the base of these flaws exceeds the long crack threshold stress intensity resulting in crack propagation (i.e., a transition from region 1 behavior to region 2 behavior due to the growth of flaws in service). Since the results of S-N fatigue tests have been reported in the literature for Alloy 75 [2, 53, 56], the first of these possibilities seems unlikely (though it should not be ignored) and the second possibility appears to be the most probable at this time. When slow strain rate tensile tests were conducted on Alloy 86 with a potentiostat to hold the potential of this alloy at a value such that pitting would occur in this alloy similar to that observed in Alloy 75 during free corrosion in service, this alloy fractured in a manner virtually identical to that observed in Alloy 75 during free corrosion. The results of this experiment indicated that once Alloy 86 contains flaws of the same size and shape as those that occur in Alloy 75 during service, the same fracture resistance results. Similar results should occur if S-N fatigue tests were conducted on these alloys. For example, if one were to grow pits into smooth S-N fatigue samples of Alloy 75 and Alloy 86 under controlled conditions so that their size could be controlled and measured and then ran fatigue tests on these samples in air and in white water, then one could quantify the extent that the fatigue limit is reduced in these alloys by the environment and the influence of flaw size in a Kittagawa diagram. However, based on the results of the slow strain rate experiments, it is reasonable to assume that for the same size pits, Alloy 75 and Alloy 86 will exhibit the similar fatigue limits. That is, the results of this study indicate that Alloy 75 fails in service because it grows larger flaws in service than Alloy 86 due to its lower pitting resistance.

The results of these analyses should enable the development of better alloys for suction roll shells. By determining that the pitting resistance of the alloys is the primary factor which determines the in-service fatigue life, it is now possible to evaluate new alloys that are resistant to this failure mode. Through the use of computer programs designed to predict and model alloy behavior, and simple electrochemical techniques to evaluate the pitting potential, it should be possible to develop new alloys that respond to the changing needs of the paper making industry. Mechanical testing techniques such as slow strain rate tensile tests and fatigue crack propagation measurements will still be required to predict performance in service, but using electrochemical measurements of pitting resistance to guide alloy development should speed alloy development, reduce the amount of mechanical testing, reduce costs and reduce the probability of premature failure. Until new alloys can be developed and placed into service, the performance of the existing alloys could possibly be improved through the use of corrosion inhibitors or simply reducing the possibility of pitting through avoiding exposure to highly oxidizing conditions in operation or during shutdown.

5. Conclusions

This evaluation was designed to investigate the measurement methods used for life prediction of duplex stainless steels in paper making environments in order to address the reported differences in service performance between two Sandusky International suction roll shell alloys. The approach adopted for this investigation was to use a review of the state of the art to determine first, whether an error or a deficiency existed in the current test methodology and second, whether the life prediction models may overlook one of the causative factors in the failure process. The primary goal of this research was to identify or develop test methods that would enable the development of alloys that are more resistant to the paper making environment through an improvement in the accuracy of the life prediction models.

The first set of experiments evaluated possible sources of measurement errors and/or other discrepancies between the testing and service environments. The parameter addressed in this evaluation was the potential influence of cyclic loading frequency on the crack propagation rate. This was examined through a series of scratch repassivation tests. The results of the evaluation revealed that the repassivation rates were very similar for both alloys and that the amount of metal lost during anodic dissolution based crack propagation mechanisms would be essentially the same for both alloys regardless of the cyclic frequency. As a result, it was concluded that the cyclic frequency had little or no influence on the crack propagation rate of these alloys and, thereby, was not a viable means to explain the reported differences in performance. The scratch experiments conducted under free corrosion conditions revealed that substantial quantities of hydrogen can be produced during film rupture but hydrogen embrittlement was ruled out as a possible fracture mechanism because the slow strain rate tensile test results revealed that neither alloy demonstrated appreciable sensitivity to hydrogen embrittlement at the fugacities predicted by the scratch repassivation transients. The results of the this study indicated that simple modifications or improvements to the experimental measurement parameters would not reveal the source of the reported differences in the service behavior between the two duplex alloys.

A second set of experiments was then designed to evaluate the possibility that some process could induce failure in one alloy and not the other. This approach required a thorough evaluation of the corrosion behavior of the two alloys in the simulated paper making environment.

Both alloys exhibited relatively good overall resistance to corrosion in the simulated deinked white water environment, but Alloy 86 consistently demonstrated better resistance to pitting in this environment than Alloy 75. The nominal compositions of the two alloys are essentially the same, and even though the available literature on the influence of copper in stainless steels is inconclusive, the enhanced pitting resistance observed in the Alloy 86 was attributed to the influence of the copper present in that alloy. Under free corrosion conditions in aerated, deinked white water, the Alloy 75 regularly exhibited pitting attack throughout the austenite phase regions as well as along the interphase interfaces. Small amounts of pitting were observed in the Alloy 86, but the pitting tended to be much finer in size and was only observed along the interphase interfaces. These pits could be the result of inhomogeneities in the passive film caused by variations in the distribution of alloying elements resulting from changes in crystal structure but they could also be an indication of chromium depletion and/or sensitization. An exact determination of the nature of the pitting in Alloy 86 requires further analysis.

Differences were observed in electrochemical data which may suggest the copper present in the Alloy 86 influences the interactions between that alloy and the individual ionic species contained in the white water. The cyclic voltammograms conducted in solutions containing individual ions also exhibited some differences in the potentials at which the electrochemical reactions occurred. The largest interactions occurred in the solution containing both thiosulfate and chloride which is in agreement with the synergistic behavior between these two ions discussed in the introduction. Some differences in the electrochemical behavior were also observed in the Alloy 75, but they were much smaller in comparison to those observed in the Alloy 86.

The most apparent difference observed in electrochemical behavior of the two alloys was the separation between the free corrosion and the pitting potentials. In the aerated white water environment, Alloy 75 showed little or no separation between the pitting potential and the free corrosion potential but, in the case of Alloy 86, the pitting potential occurred at a approximately 0.800 V higher than the free corrosion potential. This indicates that Alloy 86 requires a substantially stronger oxidizing environment to induce pitting than Alloy 75. A small separation between the free corrosion and pitting potentials thereby indicates a high probability for pitting in service as the free corrosion potential is a highly variable quantity which fluctuates with changes in the service environment. On the other hand, a wide separation between these potentials indicates a lower probability for pitting under the same corrosion conditions. That is, Alloy 75 is much more likely to pit in service whereas Alloy 86 is not.

Slow strain rate tensile tests were used to evaluate the hypothesis that the pitting resistance is the determining factor in the performance of these alloys in a paper making environment. The results of that analysis revealed that when pitting did occur, the failure mode was identical regardless of the alloy examined. In those experiments, failure was always the result of a reduction in cross sectional area caused by the formation and propagation of pitting. As the pits propagated into the tensile specimen, the anodic attack dissolved the more ductile phase (austenite) which simultaneously decreased the fracture toughness of the alloy and increased the applied stress intensity. The most important result obtained from the slow strain rate experiments is: while the fracture morphologies were essentially the same for both alloys, Alloy 86 required a large degree of polarization with a potentiostat to induce the same type of pitting which readily occurred in Alloy 75 as a result of the simple polarizing influence of the dissolved oxygen in the solution. This finding was supported by the analysis of an actual service failure which revealed that the primary crack front was formed by the union of several smaller cracks that initiated at the base of stable corrosion pits on the inside surface.

The results of this investigation demonstrated that a modification to one of the fatigue experimental parameters would not readily yield a solution to the reported disparity in the service performance between the two alloys. This evaluation also indicated that overall, the mechanical and electrochemical behaviors of these two duplex stainless steel alloys were remarkably similar and that the only real difference between the two alloys was the amount of separation between the free corrosion and pitting potentials. The increased separation in Alloy 86 reduced the probability for pitting in the white water solution and thereby increased the overall performance of the alloy in that environment. Therefore, it was concluded that the reported discrepancy was a direct result of the predictive models not properly accounting for the influence of pitting in the initiation of fatigue cracks.

In summary, the main objective of this work was to develop a solution to an industrial problem. Simply stated, the problem is in-service Alloy 75 corrosion fatigue failures occur even though the life prediction methods indicate they should not. That is, the existing measurement methods and interpretations indicate that both Alloy 75 and Alloy 86 should have essentially identical corrosion fatigue behaviors, yet one alloy fails in service while the other does not. At the onset of this work, it was thought that the development of a crack propagation methodology that had a higher resolution would provide more reliable data for use in the existing life prediction models and that data would both reveal the source of the differences in the behaviors and enable the development of alloys which are more resistant to this failure mode. A review of the literature on crack propagation in these alloys and life predicition methods led to a set of experiments that were designed to evaluate the relative influences of anodic and cathodic processes on enviromentally induced fracture in these alloys. The results of these experiments revealed that a new, higher resolution, long crack propagation technique would not yield an appropriate solution to the problem. This conclusion lead to an evaluation of the existing life prediction models which revealed that these models focus primarily on long crack behavior and they also use crack propagation data taken from long crack measurements to predict short crack behavior. That is, the existing models generally use low stress intensity crack propagation measurements taken from specimens with long cracks to predict the low stress intensity crack propagation (i.e., near threshold behavior) in service and, as shown by Kitagawa, the behavior in this regime may be very different due to the influence of short cracks. Therefore, a second set of experiments was conducted to evaluate what role corrosion may have in the initiation of cracks in these alloys. The results of these experiments demonstrated that Alloy 75 was significantly more likely to pit in service than Alloy 86 and that during pitting, the more ductile austentic phase was preferentially attacked. Furthermore, the morphology of these pits concentrate stress and nucleate cracks more effectively than predicted by the conventional life prediction models. Therefore, it was concluded that the pitting resistance and the resulting pit morphology in Alloy 75 is the source of the disparity in the performance of the alloys in service and that standard pitting resistance measurements are an appropriate means to guide the development of alloys which are more resistant to this failure mechanism.

6. References

[1] D. C. Bennett, "Corrosion Problems in the Pulp and Paper Industry," *Matls Perf*, 1984, pp. 9-12.

[2] R. A. Yeske, "Prediction of Suction Roll Performance in Paper Making," *Materials Perf.*, October, 1987, 1987, pp. 30-37.

[3] C. E. Jaske and A. P. Castillo, "Corrosion Fatigue of Cast Suction-roll Alloys in Simulated Paper-making Environments," *Matls Perf*, vol. 26, 1987, pp. 37-43.

[4] R. M. Yeske, M. A. Revall, and C. M. Thompson, "Corrosion-assisted cracking of duplex stainless steels in suction roll applications," *Tappi J.*, vol. 77, 1994, pp. 210-217.

[5] A. Garner, "Suction Roll Failures in Canada," *Pulp & Paper Canada*, vol. 86, 1985, pp. 62-67.

[6] D. C. Reid and D. A. Wensley, "Electrochemical Corrosion Testing of Duplex Stainless Steel Suction Roll Alloys," *Tappi Journal*, March 1989, 1989, pp. 57-61.

[7] R. A. Yeske, "Corrosion Fatigue Testing of Suction Roll Alloys," *Tappi Journal*, March 1988, 1988, pp. 47-54,.

[8] F. B. Pickering, "Physical Metallurgy of Stainless Steel Developments," *Inter Metal Revs*, vol. 21, 1976, pp. 227-268.

[9] J. J. Demo, "Mechanism of High Temperature Embrittlement and Loss of Corrosion Resistance in AISI 446 Stainless Steel," *Corros*, vol. 27, 1971, pp. 531-544.

[10] A. Plumtree and R. Gullberg, "Embrittlement of a Continuously Cooled Fe-25 Cr Alloy," *Metall Trans A*, vol. 7A, 1976, pp. 1451-1458.

[11] D. J. Duquette, "Corrosion Fatigue Crack Initiation Processes: A State-of-the-Art Review," *Environment-Induced Cracking of Metals*, R. P. Gangloff and M. B. Ives, Eds. NACE, 1988, 45-53.

[12] R. C. Newman, H. S. Isaacs, and B. Alman, "Effects of Sulfur Compounds on the Pitting Behavior of Type 304 Stainless Steel in Near-Neutral Chloride Solutions," *Corrosion*, vol. 38, 1982, pp. 261-265.

[13] D. A. Jones, *Principles and Prevention of Corrosion*. NY, NY: Macmillan Publishing Co, 1992.

[14] M. G. Fontana and N. D. Greene, "Corrosion Engineering," in *McGraw-Hill Series in Materials Science and Engineering*, M. B. Bever, M. E. Shank, and C. A. West, Eds., 2nd ed. NY, NY: McGraw-Hill, Inc., 1987, pp. 28-115.

[15] H. Kaesche, *Metallic Corrosion*, 2nd ed. Houston, TX: National Assoc. of Corrosion Engineers, 1985.

[16] H. P. Leckie and H. H. Uhlig, *J. Electrochem. Soc.*, vol. 113, 1966, pp. 1262.

[17] R. C. Newman and K. Sieradzki, "Electrochemical Aspects of Stress-Corrosion Cracking of Sensitised Stainless Steels," *Corros Sci*, vol. 23, 1983, pp. 363-378.

[18] R. C. Newman and E. M. Franz, “Growth and Repassivation of Single Corrosion Pits in Stainless Steel,” *Corrosion*, vol. 40, 1984, pp. 325-330.

[19] A. J. Sedriks, “Corrosion of Stainless Steels,” in *The Corrosion Monograph Series*, R. T. Foley, N. Hackerman, C. V. King, F. L. LaQue, and Z. A. Foroulis, Eds. NY, NY: John Wiley and Sons, 1979.

[20] R. M. Latanision, O. H. Gastine and C. R. Compeau, "Stress Corrosion Cracking and Hydrogen Embrittlement: Differences and Similarities," *Envrionment-Sensitive Fracture of Engineering Materials*, Z. A. Foroulis, Ed. The Metallurgical Society of AIME, 1977, 48-70.

[21] D. A. Jones, “Chapter 8: Environmentally Induced Cracking,” in *Principles and Prevention of Corrosion*. NY, NY: Macmillan Publishing Co, 1992, pp. 234-289.

[22] U. Bertocci, E. N. Pugh and R. E. Ricker, "Environment-Induced Cracking of Copper Alloys," *Environment-Induced Cracking of Metals*, R. P. Gangloff and M. B. Ives, Eds. NACE, 1988, 273-285.

[23] J. R. Rice and R. Thomson, “Ductile versus Brittle Behavior of Crystals,” *Phil Mag*, vol. 29, 1974, pp. 73-97.

[24] M. R. Stoudt and R. E. Ricker, “Characterization of the Hydrogen Induced Cold Cracking Susceptibility at Simulated Weld Zones in HSLA-100 Steel,” NIST, NISTIR 5408, 1994 .

[25] R. A. Oriani, “Hydrogen— The Versatile Embrittler,” *Corro*, vol. 43, 1987, pp. 390-397.

[26] H. H. Johnson, “Hydrogen in Iron,” *Metall Trans A*, vol. 19A, pp. 2371-2387, 1988.

[27] S. Suresh, *Fatigue of Materials*. Cambridge, UK: Cambridge University Press, 1991.

[28] R. E. Ricker and D. J. Duquette, "The Role of Environment on Time Dependent Crack Growth," *Micro and Macro Mechanics of Crack Growth*, K. Sadananda, B. B. Rath and D. J. Michel, Eds. TMS, 1981, 29-47.

[29] R. P. Gangloff, "Corrosion Fatigue Crack Propagation in Metals," *Environment-Induced Cracking of Metals*, R. P. Gangloff and M. B. Ives, Eds. NACE, 1988, 55-109.

[30] H. Spaehn, "Stress Corrosion Cracking and Corrosion Fatigue of Martensitic, Ferritic and Ferritic-Austenitic (Duplex) Stainless Steels," *Environment-Induced Cracking of Metals*, R. P. Gangloff and M. B. Ives, Eds. NACE, 1988, 449-487.

[31] C. Laird and D. J. Duquette, "Mechanisms of Fatigue Crack Nucleation," in *Corrosion Fatigue*. Houston, TX: NACE, 1972, pp. 88-117,.

[32] A. J. McEvily and R. P. Wei, "Fracture Mechanics and Corrosion Fatigue," in *Corrosion-fatigue: Chemistry,Mechanics and Microstructure*, vol. NACE-2, O. F. Devereux, A. J. McEvily, and R. W. Staehle, Eds. Houston, TX: NACE, 1972, pp. 381-395.

[33] G. E. Deiter, "Mechanical Metallurgy," in *McGraw-Hill Series in Materials Science and Engineering*, M. B. Bever, Ed., 3 ed. NY, NY: McGraw-Hill, 1986, pp. 275-324.

[34] R. P. Wei and J. Landes, "Correlation Between Sustained-load and Fatigue Crack Growth in High Strength Steels," *Materials Research and Standards*, vol. 9, 1970, pp. 25-27, 44-46.

[35] I. M. Austen and P. McIntyre, "Corrosion-fatigue of High-Strength Steel in Low Pressure Hydrogen Gas," *Metal Science*, vol. 13, 1979, pp. 420-428.

[36] F. P. Ford and P. L. Andresen, "Advances in Fracture Research," , K. Salema, K. Ravi-Chandor, D. M. R. Taplin, and P. R. Rao, Eds. Oxford, UK: Pergamon Press, 1989, pp. 1571-1584.

[37] A. Garner, "Thiosulphate Corrosion in Paper Machine White Water," *Corrosion*, vol. 41, 1985, pp. 587-591.

[38] R. C. Newman, K. Sieradzki, and H. S. Isaacs, "Stress Corrosion Cracking of Sensitized Type 304 Stainless Steel in Thiosulfate Solutions," *Metal Trans A*, vol. 13A, 1982, pp. 2015-2026.

[39] R. C. Newman, "The Dissolution and Passivation Kinetics of Stainless Alloys Containing Molybdenum—II. Dissolution Kinetics in Artificial Pits," *Corros Sci*, vol. 25, 1985, pp. 341-350.

[40] D. B. Wells, J. Stewart, R. Davidson, P. M. Scott, and D. E. Williams, "The Mechanism of Intergranular Stress Corrosion Cracking of Sensitized Austenitic Stainless Steel in Dilute Thiosulphate Solution," *Corros Sci*, vol. 33, 1992, pp. 39-71.

[41] G. Valensi, J. V. Muylder, and M. Pourbaix, "Sulphur," in *Atlas of Electrochemical Equilbria in Aqueous Solutions*. Paris: Pergammon Press/Cebelcor, 1966, pp. 545-553.

[42] R. E. Reed-Hill, *Physical Metallurgy Principles*, 2nd ed. Boston, MA: PWS-Kent, 1973.

[43] G. L. Kehl, *The Principles of Metallographic Laboratory Practice*, 3rd ed. NY: McGraw-Hill, 1949.

[44] G. F. VanderVoort, "Quantitative Metallography," in *Metallography Principles and Practice, Materials Science and Engineering Series*. NY: McGraw-Hill Inc, 1984, pp. 410-502.

[45] A. J. Bard and L. R. Faulkner, *Electrochemical Methods*. New York: J. Wiley & Sons, 1980.

[46] M. R. Stoudt, A. K. Vasudevan, and R. E. Ricker, "Examination of the Influence of Lithium on the Repassivation Rate of Aluminum Alloys," in *New Methods for Corrosion Testing of Aluminum Alloys*, ASTM STP 1134, V. S. Agarwala and G. M. Ugiansky, Eds. Phila. PA: Am. Society for Testing and Materials, 1992, pp. 196-213.

[47] R. C. Newman, "The Dissolution and Passivation Kinetics of Stainless Alloys Containing Molybdenum—I. Fe-Cr-Mo Alloys," *Corros Sci*, vol. 25, 1985, pp. 331-339.

[48] M. R. Stoudt, J. L. Fink, and R. E. Ricker, "Evaluation of the Propensity of Replacements for Halon 1301 to Induce Stress Corrosion Cracking in Alloys Used in Aircraft Fire-Suppressant Storage and Distribution Systems," *J. Matls Engr and Perf*, Vol 5, 1996, pp. 507-515.

[49] M. R. Stoudt, J. L. Fink and R. E. Ricker, "Evaluation of the Stress Corrosion Cracking Susceptibility of Fire Suppressant Storage Container Alloys in Replacement Candidates for Halon 1301," *Tri-Service Conference on Corrosion*, T. Naguy, Ed. 1994, pp. 467-478.

[50] T. Lyman, "Metallography, Structures and Phase Diagrams," in *ASM Handbook*, vol. 8, 8 ed. Metals Park, OH: ASM International, 1973.

[51] B. N. Taylor and C. E. Kuyatt, "Guidelines for Evaluating and Expressing the Uncertainty of NIST Measurement Results," NIST, NIST Technical Note 1297-1994 Edition, 1994.

[52] R. E. Ricker, M. R. Stoudt and J. L. Fink, "Hydrogen Embrittlement of Ductile Nickel Aluminide During Corrosion in Aqueous Solutions," *Hydrogen Effects on Material Behavior*, N. R. Moody and A. W. Thompson, Eds. TMS, 1990, pp. 499-506.

[53] A. P. Castillo, G. M. Michel, and J. C. Rogers, “Alloy 86— A Suction Roll Material for White Waters Containing Thiosulfate Ion,” *Tappi Journal*, vol. 72, 1989, pp. 193-197.

[54] Anon., “ASTM Designation G-30— Standard Practice for Making and Using U-Bend Stress-Corrosion Test Specimens,” in *Annual Book of ASTM Standards, Section 3, Metals Test Methods and Analytical Procedures*, vol. 03.02 Wear and Erosion; Metal Corrosion. Phila, PA, 1993.

[55] J. A. Beavers and G. H. Koch, “Limitations of the Slow Strain Rate Test Technique,” in *Slow Strain Rate Testing for the Evaluation of Environmentally Induced Cracking: Research and Engineering Applications, ASTM STP 1210*, R. D. Kane, Ed. Philadelphia, PA: American Society for Testing and Materials, 1993, pp. 22-39.

[56] A. P. Castillo and G. M. Michel, “A Suction-Roll Shell Material With Improved Corrosion-Fatigue Strength,” *Tappi J.*, vol. 75, 1992, pp. 131-138.

[57] A. K. Vasudevan, K. Sadananda, and K. Rajan, “Role of Microstructures on The Growth of Long Fatigue Cracks,” *Int. J. Fatigue*, vol. 19, 1997, pp. 151-159.

[58] K. Sadananda and V. K. Vasudevan, “Short Crack Growth Behavior,” in *Fatigue and Fracture Mechanics: 27th Volume, ASTM STP 1296*, R. S. Piascik and J. C. Newman, Eds. Philadelphia, PA: ASTM, 1997, pp. 301-316.

[59] A. Moskowitz, G. A. Saltzman, K. E. Pinnow, and L. S. Redmerski, “Influence of Residual and Minor Elements on the Pitting and Atmospheric Corrosion Resistance of Austenitic Stainless Steels,” in *Effects of Residual Elements on the Properties of Stainless Steels, ASTM STP 418*. Phila, PA: ASTM, 1967, pp. 3-22.

[60] G. W. Castellan, *Physical Chemistry*, 3rd ed. Menlo Park, CA: The Benjamin/Cummings Publishing Co, 1983.

[61] M. Stern, “The Effect of Alloying Elements in Iron on Hydrogen Overvoltage and Corrosion Rate in Acid Environments,” *J. Electrochem Soc*, vol. 102, 1955, pp. 663-668.

[62] H. Kitagawa and S. Takahashi, "Applicability of Fracture Mechanics to Very Small Cracks or the Cracks in the Early Stage," Second International Conference on Mechanical Behavior of Materials, Am. Soc. for Metals, 1976, 627-631.

Table 1. Nominal Alloy Compositions

Element	Alloy 75 wt%	Alloy 75 at%	Alloy 86 wt%	Alloy 86 at%
C	0.017	0.077	0.014	0.064
Mn	0.760	0.755	0.800	0.795
Si	0.500	0.972	0.770	1.496
Cr	25.390	26.652	26.070	27.357
Ni	6.700	6.229	6.800	6.320
Mo	0.030	0.017	0.030	0.017
N	0.066	0.257	0.055	0.214
P	0.032	0.056	0.032	0.056
S	0.011	0.019	0.003	0.005
Cu	0.180	0.155	2.080	1.786
Fe	66.314	64.811	63.346	61.890

Table 2. Nominal Mechanical Property Data
(as reported by Sandusky International)

Property	**Alloy 75**	**Alloy 86**
Yield Stress, MPa (KSI)	386 (56)	450 (65)
UTS, MPa (KSI)	740 (107)	800 (116)
Elongation (%)	15	22
RA (%)	16	27

Table 3. Nominal Solution Chemistries

Standard White Water

Anion	Concentration
SO_4^{-2}	500 ppm
Cl^-	200 ppm
$S_2O_3^{-2}$	50 ppm

White Water— Minus Thiosulfate

Anion	Concentration
SO_4^{-2}	500 ppm
Cl^-	200 ppm

White Water— Minus Chloride

Anion	Concentration
SO_4^{-2}	500 ppm
$S_2O_3^{-2}$	50 ppm

Na^+ was used as the cation in all cases.

The solution pH was adjusted to 3.9 ± 0.1

Table 4a. Open Circuit Scratch-Repassivation Data for Alloy 75

Scratch Number	**E_{min} (V_{SCE})**	**dE/dt (V_{SCE}/s)**
1	-0.5535	19.8020
2	-0.8370	180.0000
3	-0.7010	52.0000
4	-0.7710	58.5714
5	-0.6390	97.1963
Avg	-0.7003	81.5139
Std Dev	0.1107	61.5452

Table 4b. Open Circuit Scratch-Repassivation Data for Alloy 86

Scratch Number	**E_{min} (V_{SCE})**	**dE/dt (V_{SCE}/s)**
1	-0.4150	12.9032
2	-0.4170	6.3492
3	-0.7800	52.1739
4	-0.8120	55.5556
5	-0.6660	194.5946
Avg	-0.6180	64.3153
Std Dev	0.1922	76.1579

Table 5a. Controlled Potential Scratch-Repassivation Data for Alloy 75

Scratch Number	t (seconds)	i(B)	t(B)	n	i(t)
1	0.000965	1.0292	0.000187	-0.5549	-0.004468
2	0.000690	1.5586	0.000211	-0.4240	-0.008321
3	0.000850	0.9133	0.000206	-0.4974	-0.006746
Avg	0.000835	1.1670	0.000201	-0.4921	-0.006512
Std Dev	0.000138	0.3440	0.000013	0.0656	0.002583

Table 5b. Controlled Potential Scratch-Repassivation Data for Alloy 86

Scratch Number	t (seconds)	i(B)	t(B)	n	i(t)
1	0.000480	1.7454	0.000206	-0.4974	-0.006746
2	0.000900	1.7527	0.000426	-0.6316	-0.004667
3	0.001120	1.5384	0.000365	-0.4477	-0.011432
Avg	0.000833	1.6788	0.000332	-0.5256	-0.007615
Std Dev	0.000325	0.1217	0.000114	0.0952	0.003465

The current required for repassivation, i(t), was determined with the following equation:

$$i(t) = i_B \left[\frac{t}{t_B} \right]^n$$

Table 6a. Slow Strain Rate Mechanical Data for Sandusky Alloy 75

Testing Environment	Potential (Vsce)	Ultimate Tensile Stress (MPa)	Total Strain to Failure (percent)	Reduction in Area (percent)
Nitrogen	n/a	650.06	13.54	18.41
White Water @ 50 °C	FCP	588.52	8.38	9.85
White Water @ 50 °C	-0.300	552.12	4.01	17.86
White Water @ 50 °C	-0.600	625.21	8.11	8.35
White Water @ 50 °C	-0.850	588.47	7.69	7.22

Table 6b. Slow Strain Rate Mechanical Data for Sandusky Alloy 86

Testing Environment	Potential (Vsce)	Ultimate Tensile Stress (MPa)	Total Strain to Failure (percent)	Reduction in Area (percent)
Nitrogen	n/a	645.96	10.41	15.98
White Water @ 50 °C	FCP	620.33	10.86	14.81
White Water @ 50 °C	-0.300	730.02	16.56	26.68
White Water @ 50 °C	-0.600	659.75	13.44	17.78
White Water @ 50 °C	+0.850	518.97	3.54	7.21

Table 7a. Mechanical Property Ratios vs Nitrogen for Sandusky Alloy 75

Testing Environment	Potential (Vsce)	Ultimate Tensile Stress (MPa)	Total Strain to Failure (percent)	Reduction in Area (percent)
Nitrogen	n/a	1.000	1.000	1.000
White Water @ 50 °C	FCP	0.905	0.619	0.535
White Water @ 50 °C	-0.300	0.849	0.296	0.970
White Water @ 50 °C	-0.600	0.962	0.599	0.454
White Water @ 50 °C	-0.850	0.905	0.568	0.392

Table 7b. Mechanical Property Ratios vs Nitrogen for Sandusky Alloy 86

Testing Environment	Potential (Vsce)	Ultimate Tensile Stress (MPa)	Total Strain to Failure (percent)	Reduction in Area (percent)
Nitrogen	n/a	1.000	1.000	1.000
White Water @ 50 °C	FCP	0.960	1.043	0.926
White Water @ 50 °C	-0.300	1.130	1.591	1.669
White Water @ 50 °C	-0.600	1.021	1.292	1.112
White Water @ 50 °C	+0.850	0.803	0.341	0.451

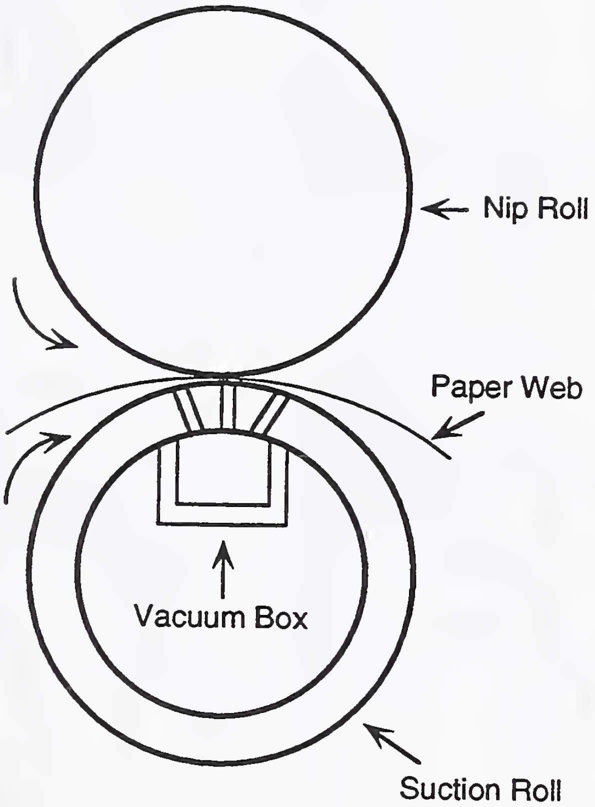

Figure 1. Schematic diagram showing the general configuration of a suction press (or nip) roll. (after Yeske, 1987)

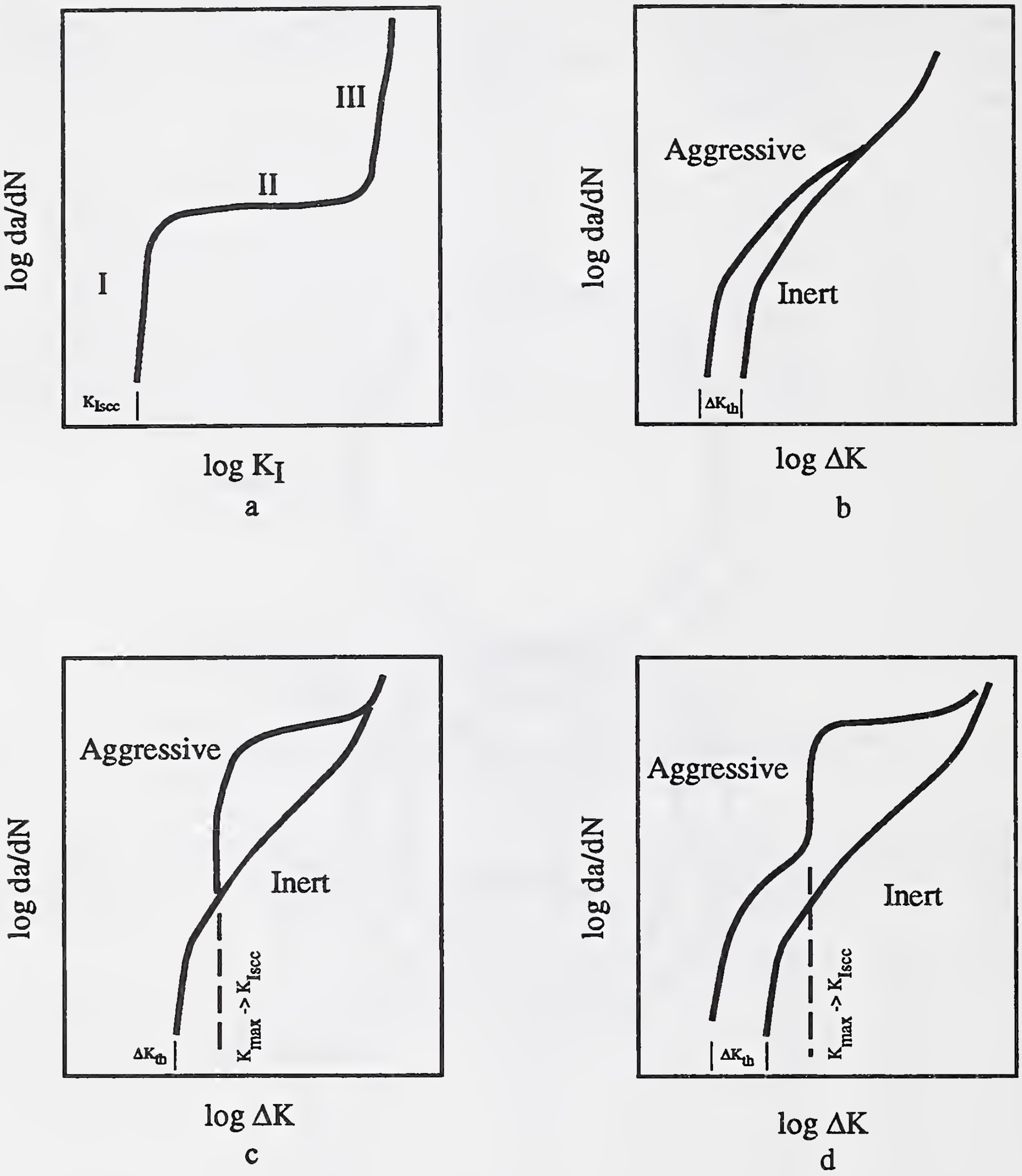

Figure 2. A schematic representations of the combined mechanical fatigue and environmentally induced crack growth. a) Crack growth under sustained loads. b) True corrosion fatigue. c) Stress corrosion-fatigue and d) Mixed corrosion and stress corrosion fatigue behavior. (after McEvily and Wei 1972.)

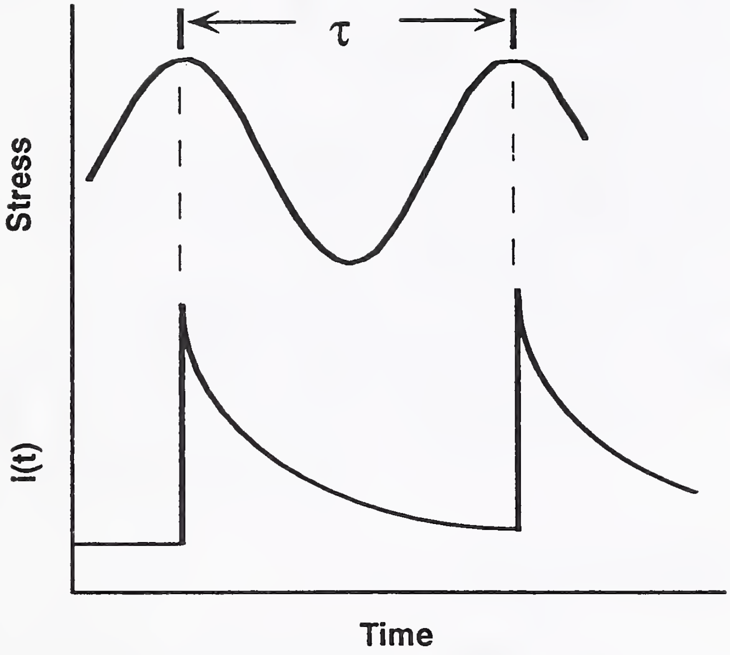

Figure 3. Schematic illustration showing the relationship between cyclic loading and passive film restoration current transients.

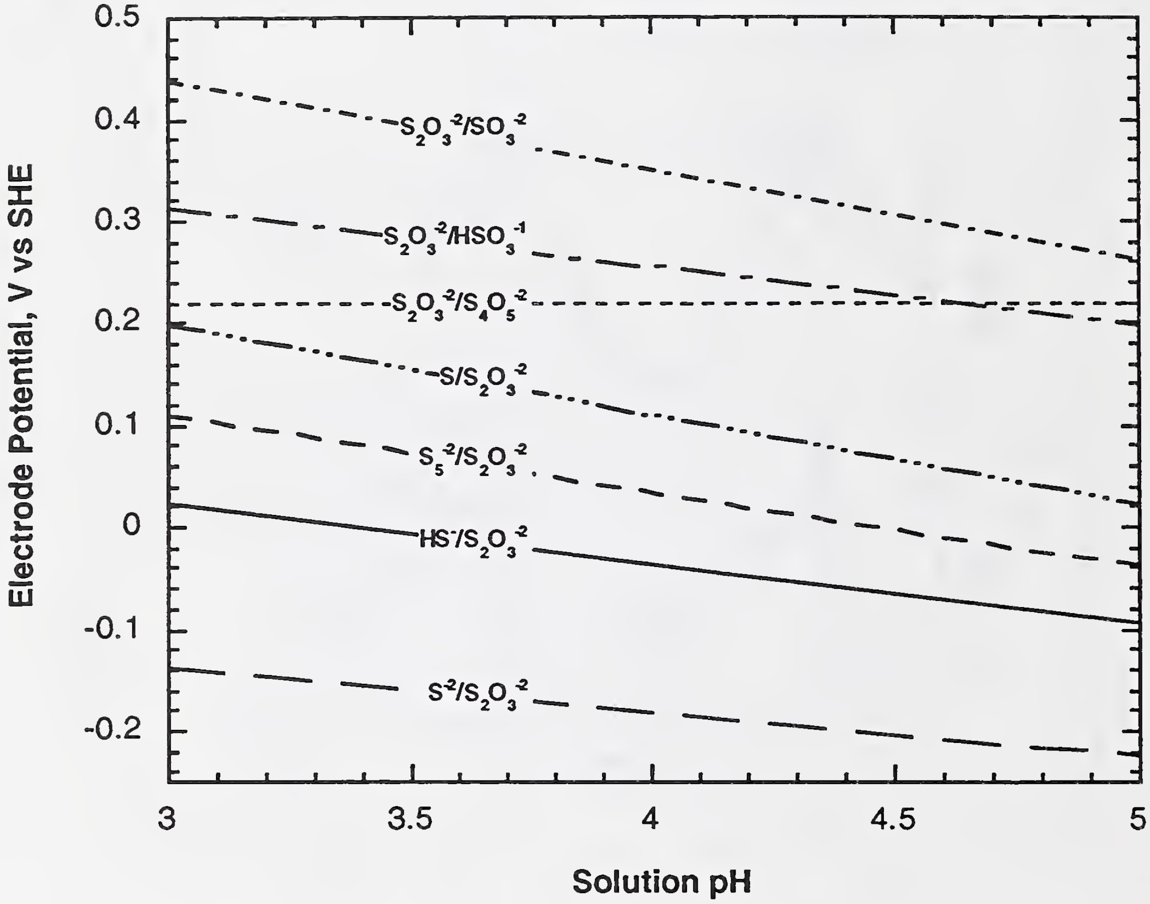

Figure 4. E-pH diagram showing the possible reactions with thiosulfate over the nominal white water solution pH range. (after Valensi, 1966)

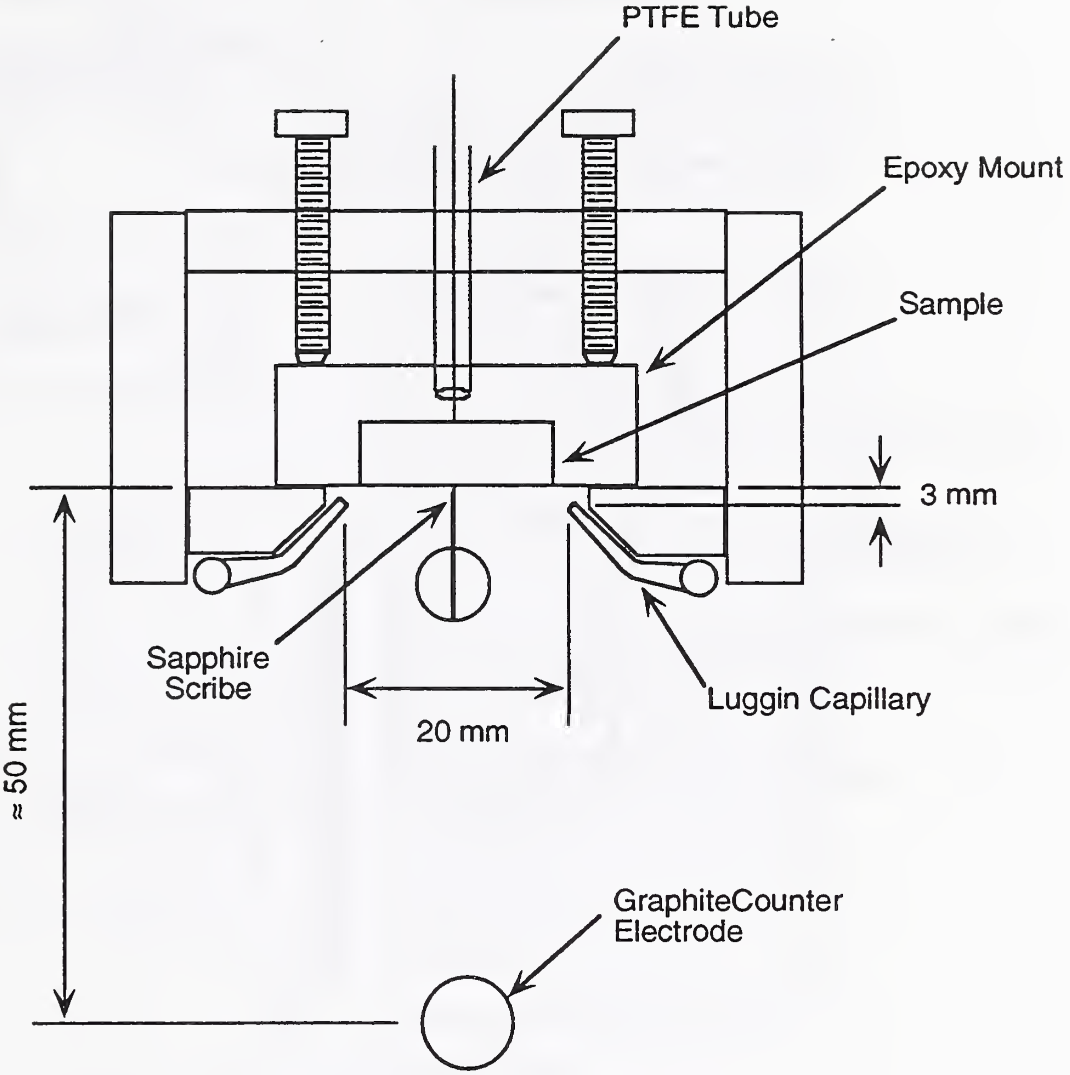

Figure 5. Schematic diagram of the scratch system sample holder illustrating the arrangement of the Luggin capillaries and counter electrode.

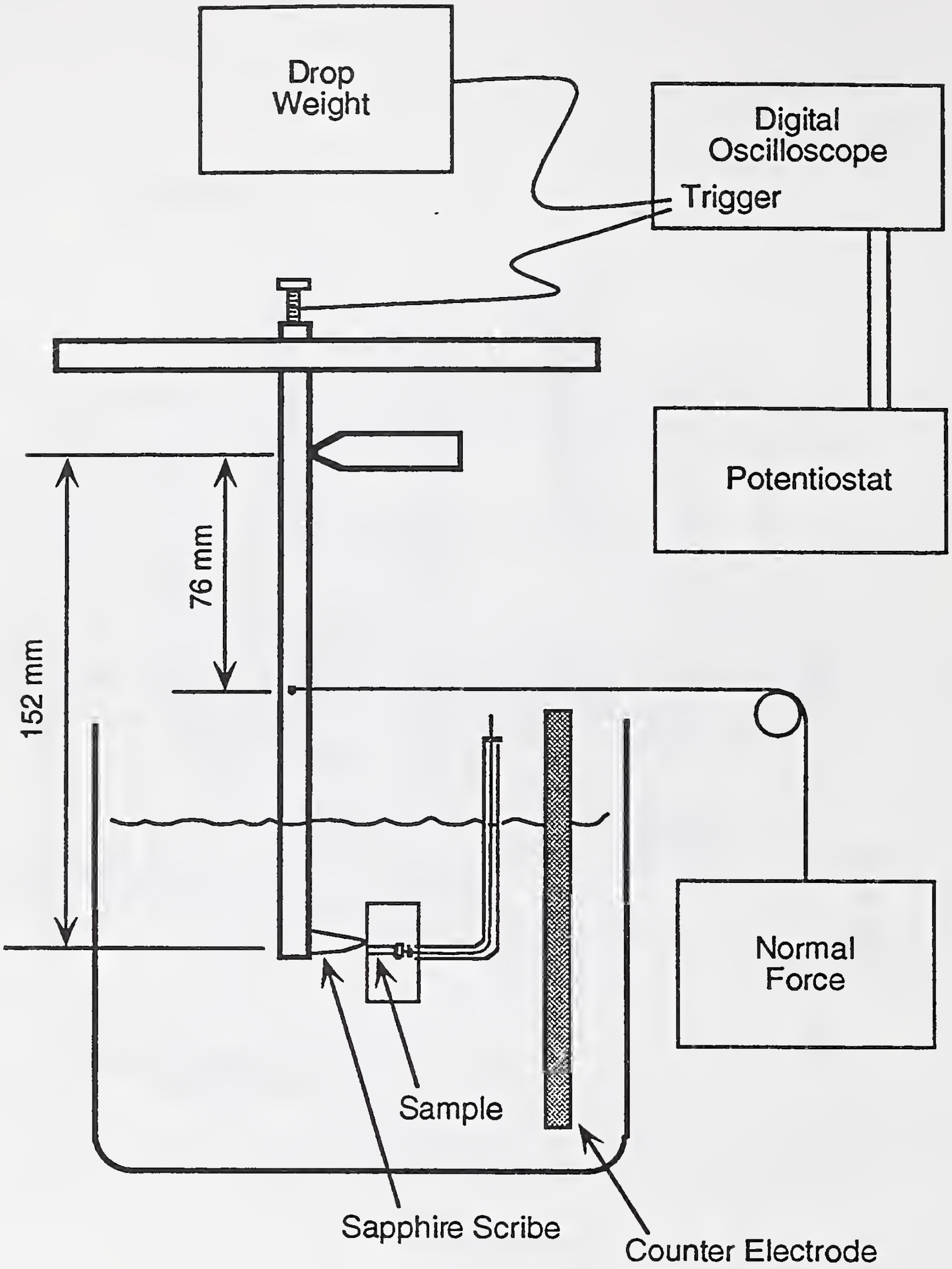

Figure 6. Schematic diagram of the apparatus used to generate the bare surface in the scratch-repassivation measurements.

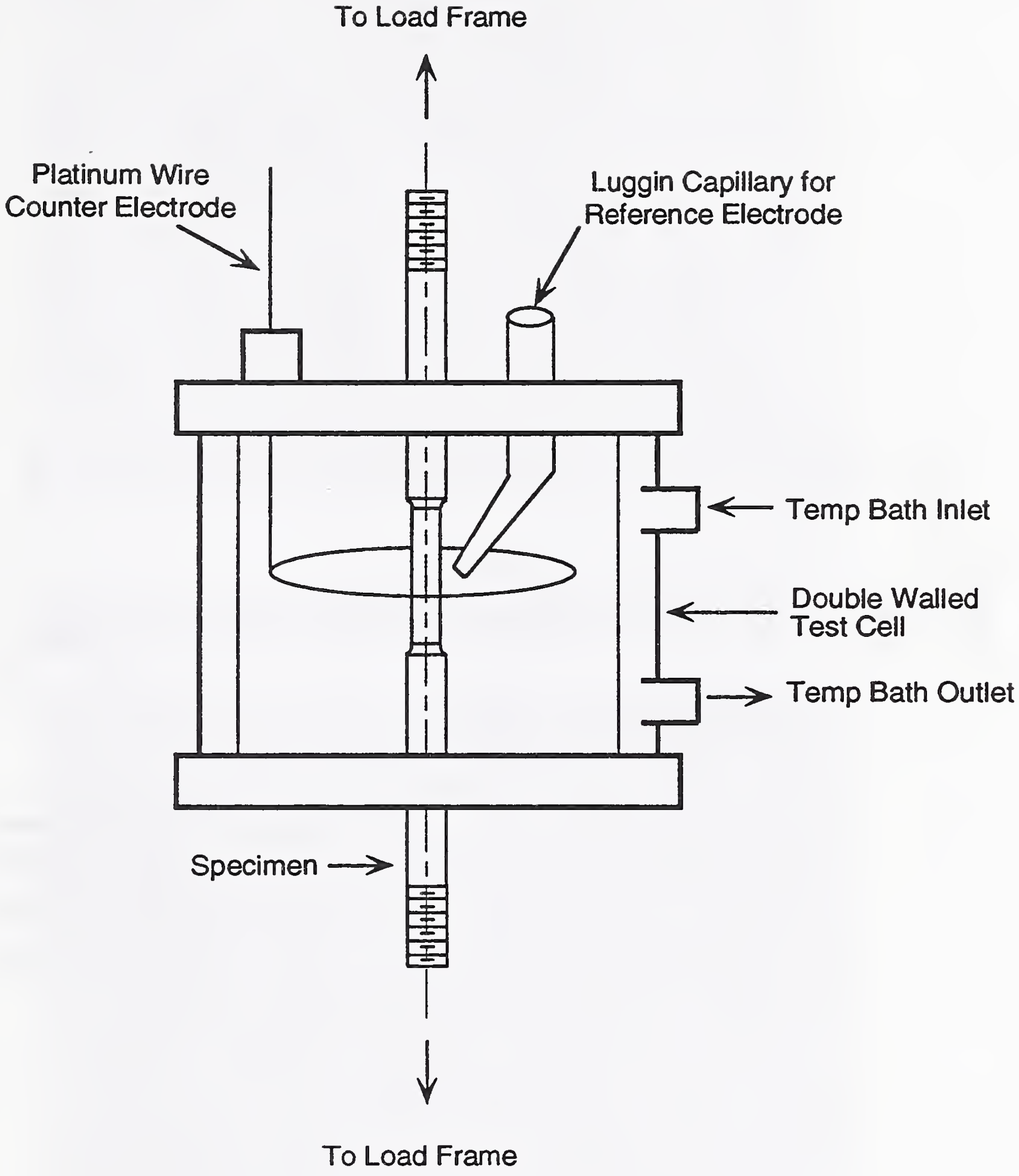

Figure 7. A schematic diagram of the electrochemical cell used in the slow strain rate tests.

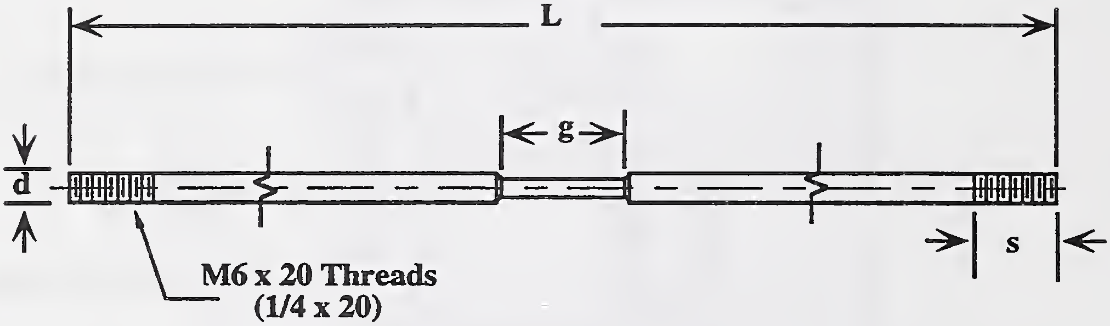

d = 19 mm (0.25 in)
L = 178 mm (7.0 in)
g = 25.4 mm (1.0 in)
s = 19 mm (0.75 in)

Figure 8. Schematic diagram of the specimen geometry used for the slow strain rate tensile experiments.

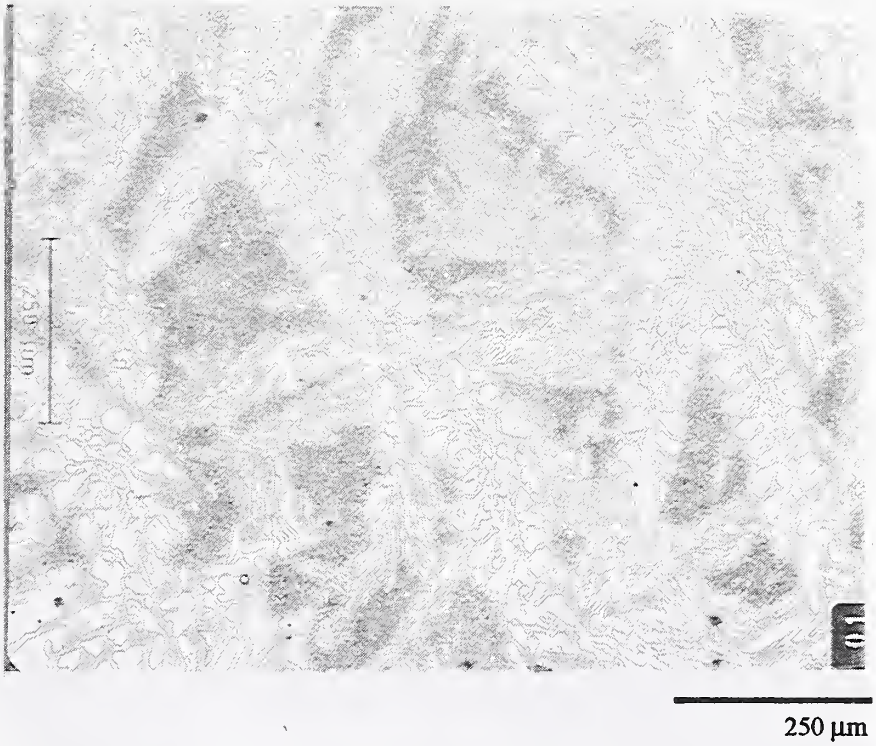

Figure 9a. Optical micrograph showing the duplex structure of Sandusky Alloy 75. (Viella's etch. Gray: Ferrite, White: Austenite)

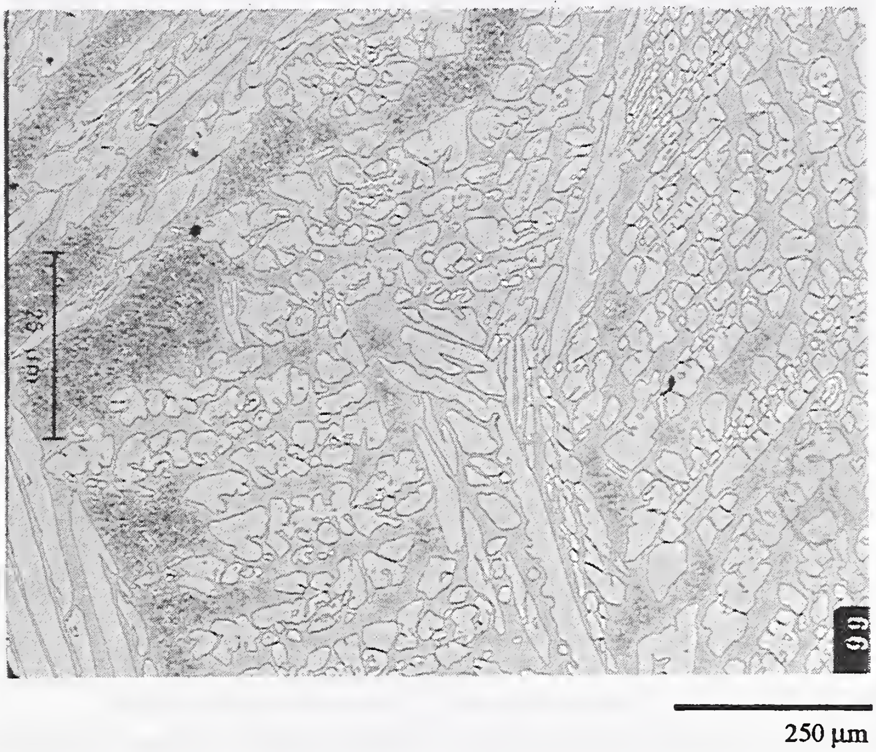

Figure 9b. Optical micrograph showing the duplex structure of Sandusky Alloy 86. (Viella's etch. Gray: Ferrite, White: Austenite)

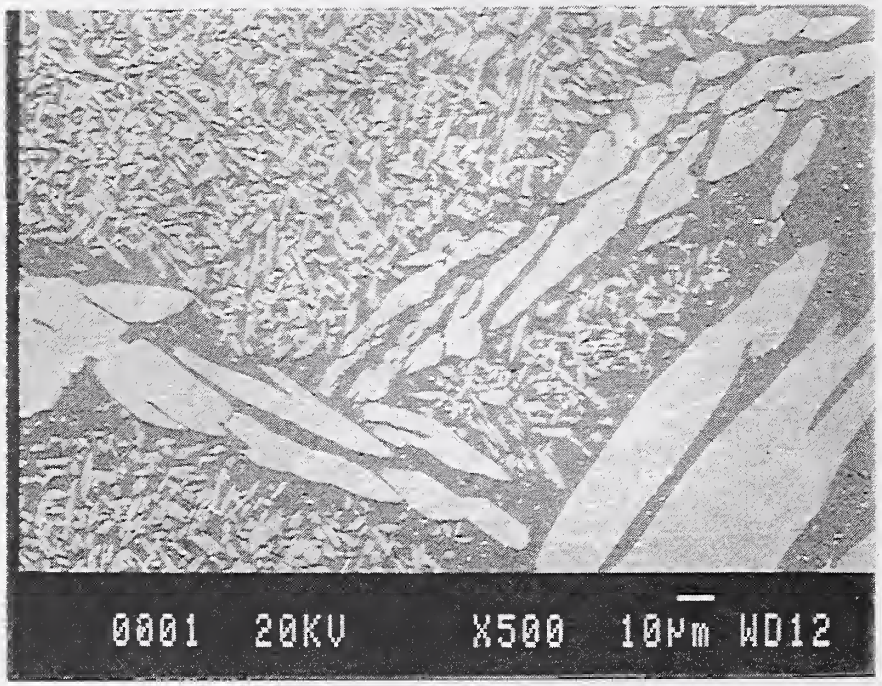

Figure 10. Back scattered scanning electron micrograph of Sandusky Alloy 86. (Dark Regions: Ferrite, Bright Regions: Austenite)

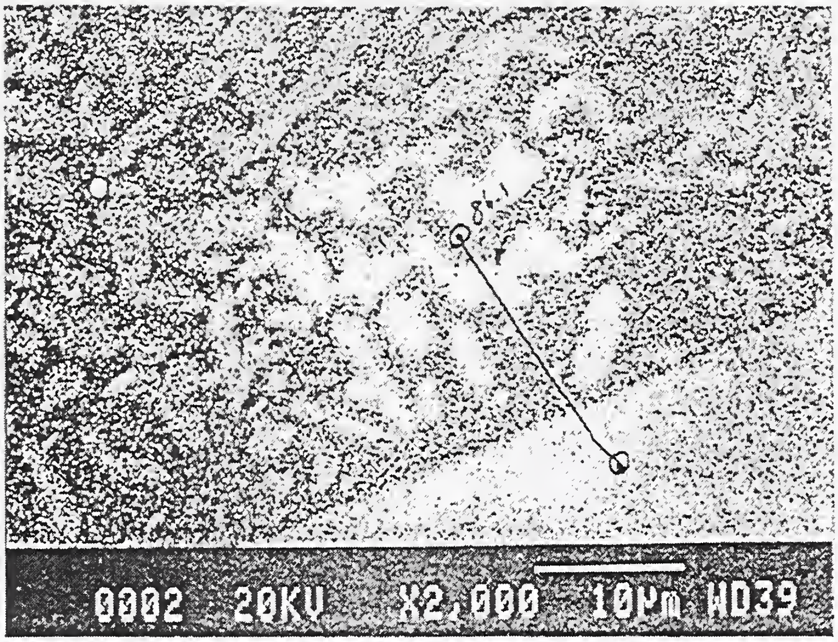

Figure 11a. BSE micrograph of Sandusky Alloy 86 optimized for EDS compostional analysis.

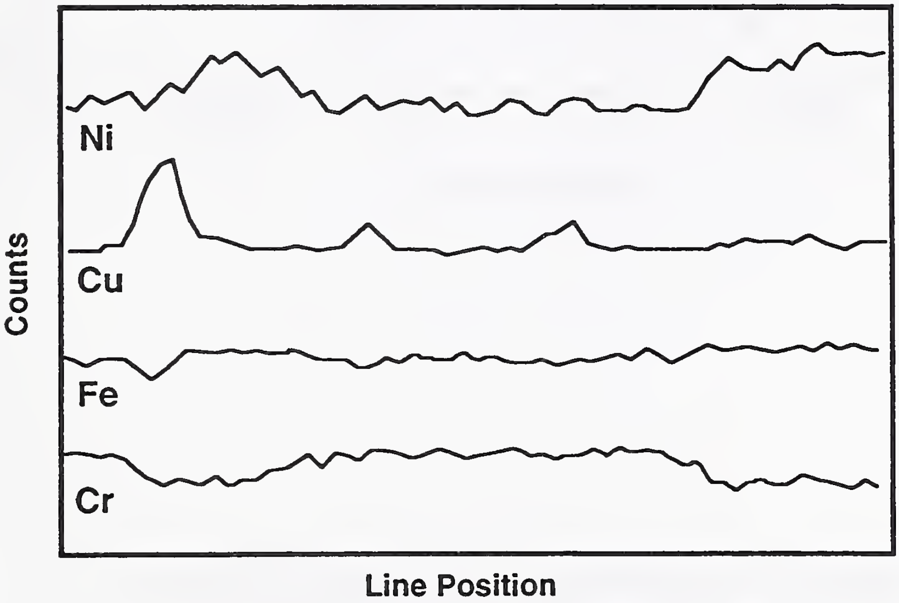

Figure 11b. 4 element EDS compositional profile for the scanned lineshown in Figure 11a. Note that Cu is only present in the bright regions (austenite).

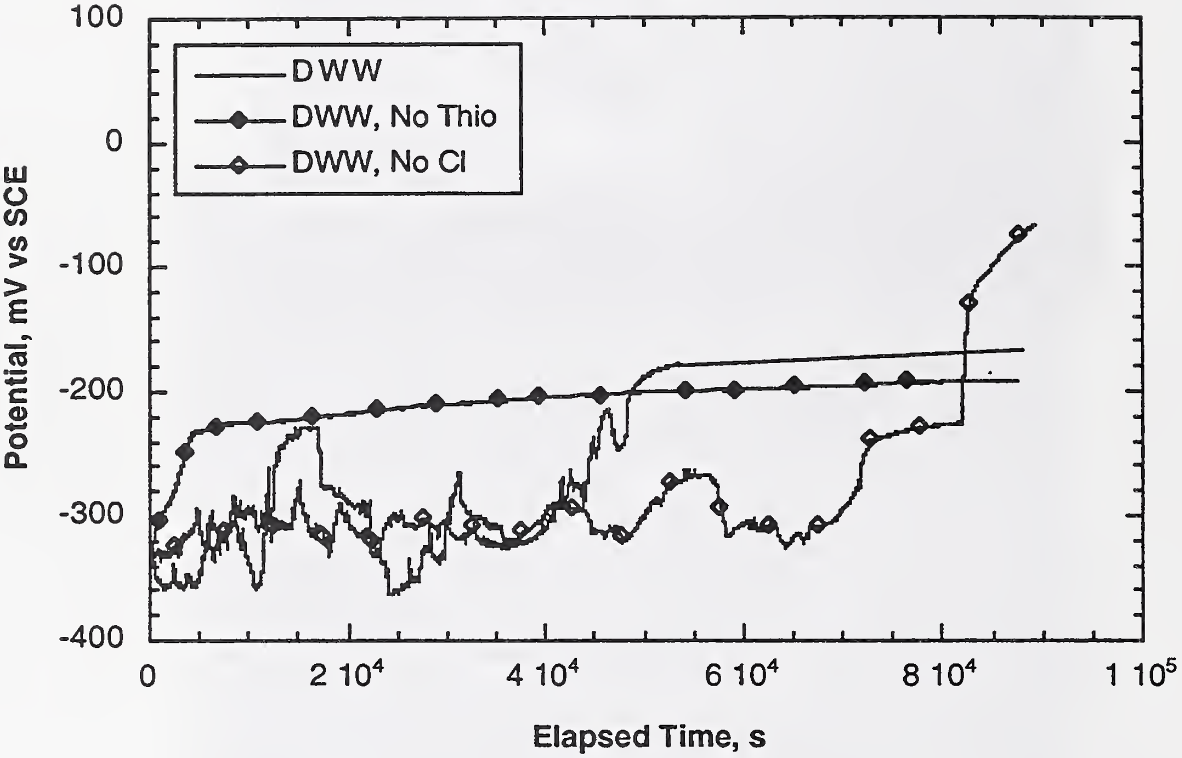

Figure 12. Free corrosion potential for Sandusky Alloy 75 in aerated, deinked simulated white water at 50 °C.

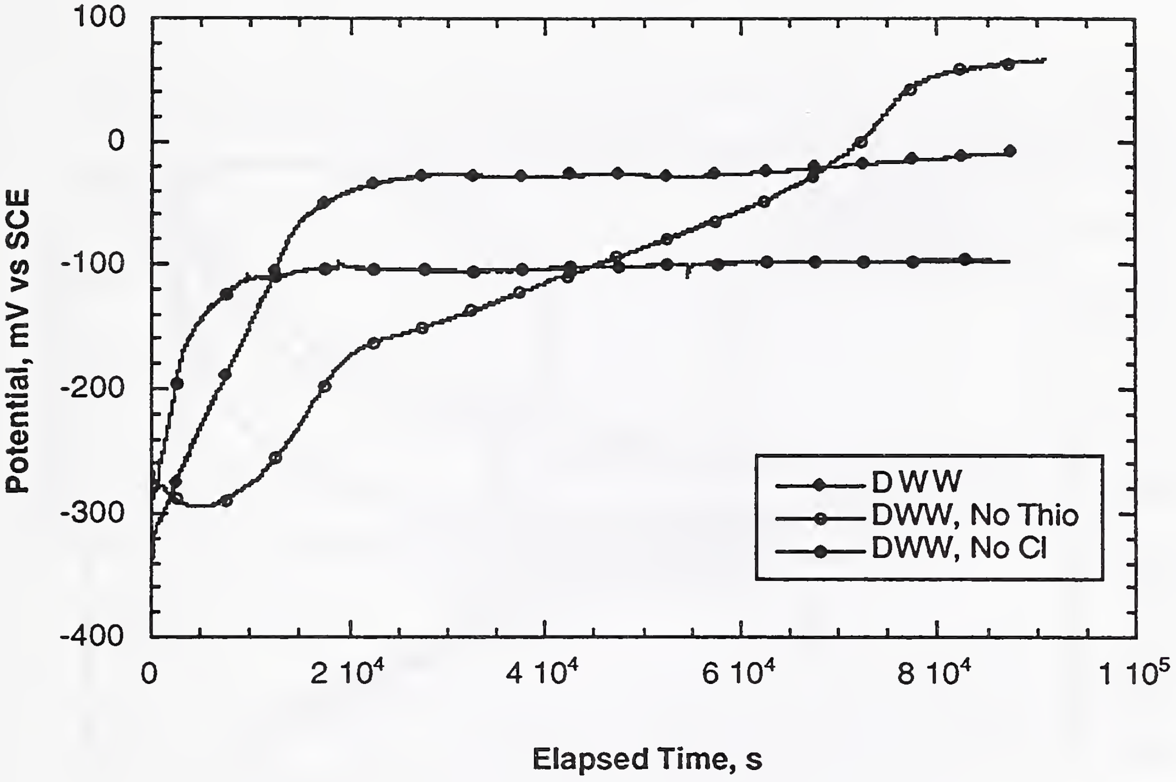

Figure 13. Free corrosion potential for Sandusky Alloy 86 in aerated, deinked simulated white water at 50 °C.

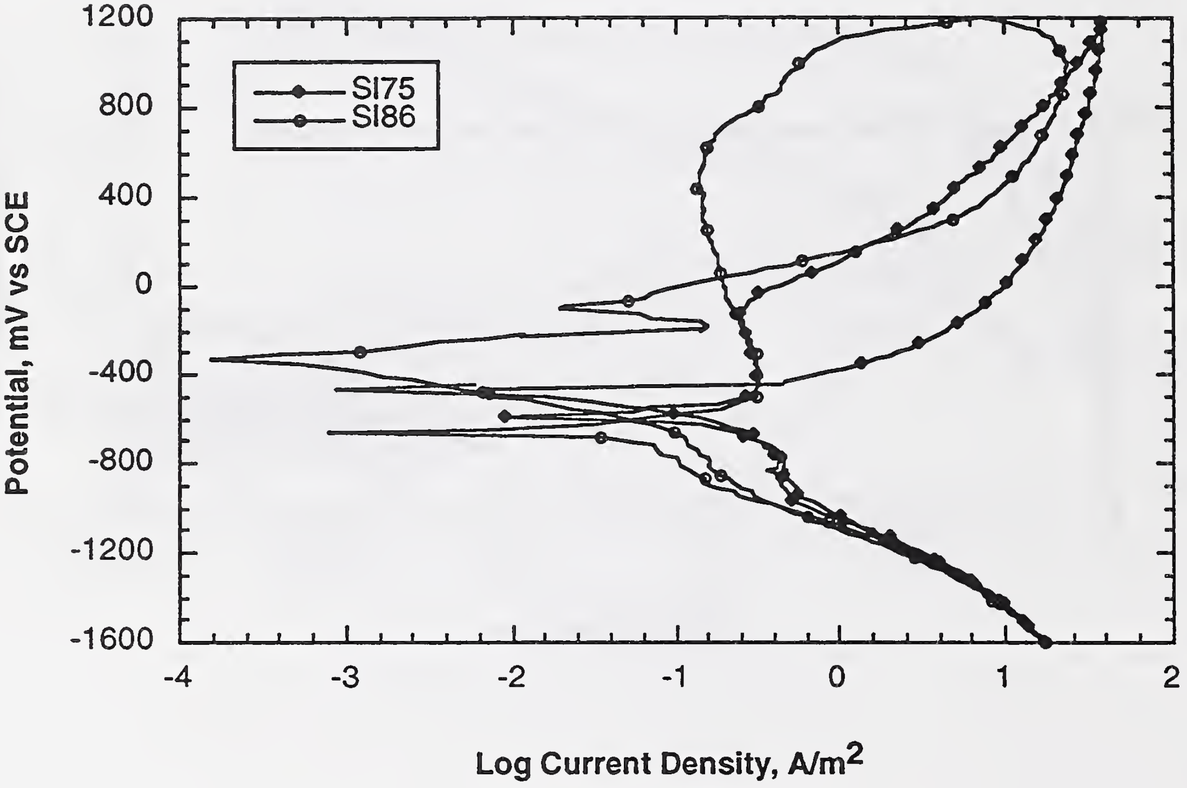

Figure 14. Comparison of the electrochemical behavior of the two Sandusky alloys in deaerated, deinked white water at 50 °C with a 5 mV/s sweep rate.

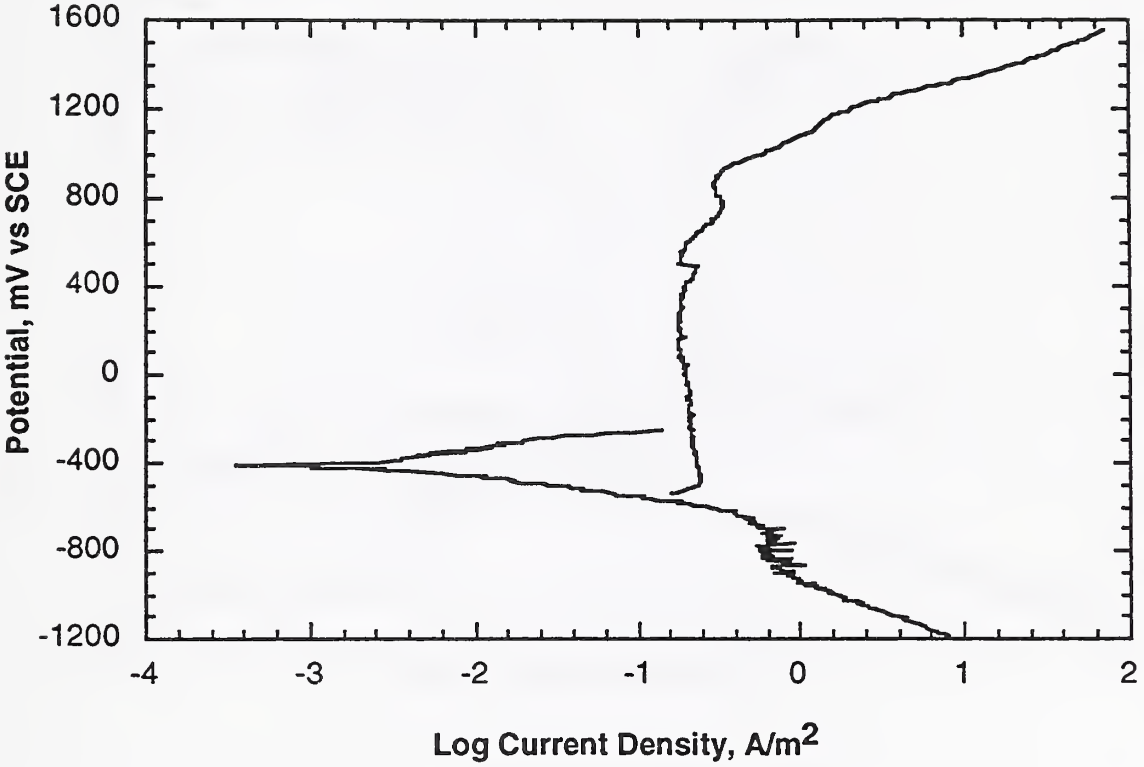

Figure 15. Composite Sweep for Sandusky Alloy 75 in deaerated, deinked white water at 50 °C with a 1 mV/s sweep rate.

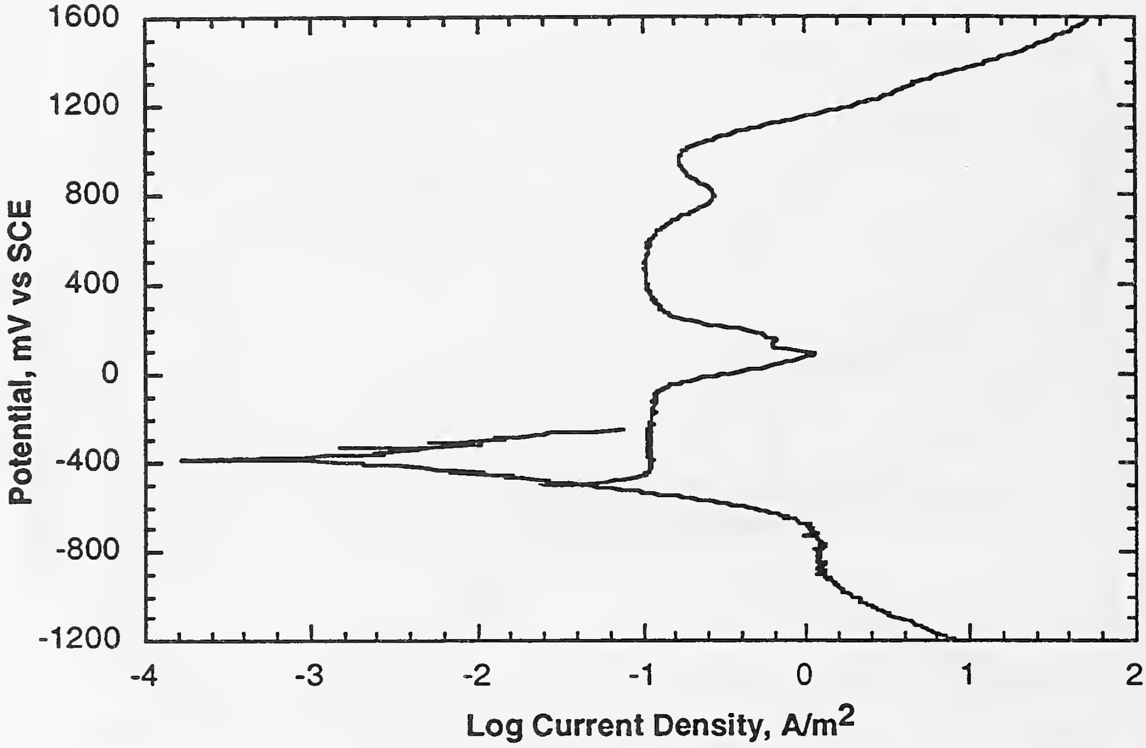

Figure 16. Composite Sweep for Sandusky Alloy 86 in deaerated, deinked white water at 50 °C with a 1 mV/s sweep rate.

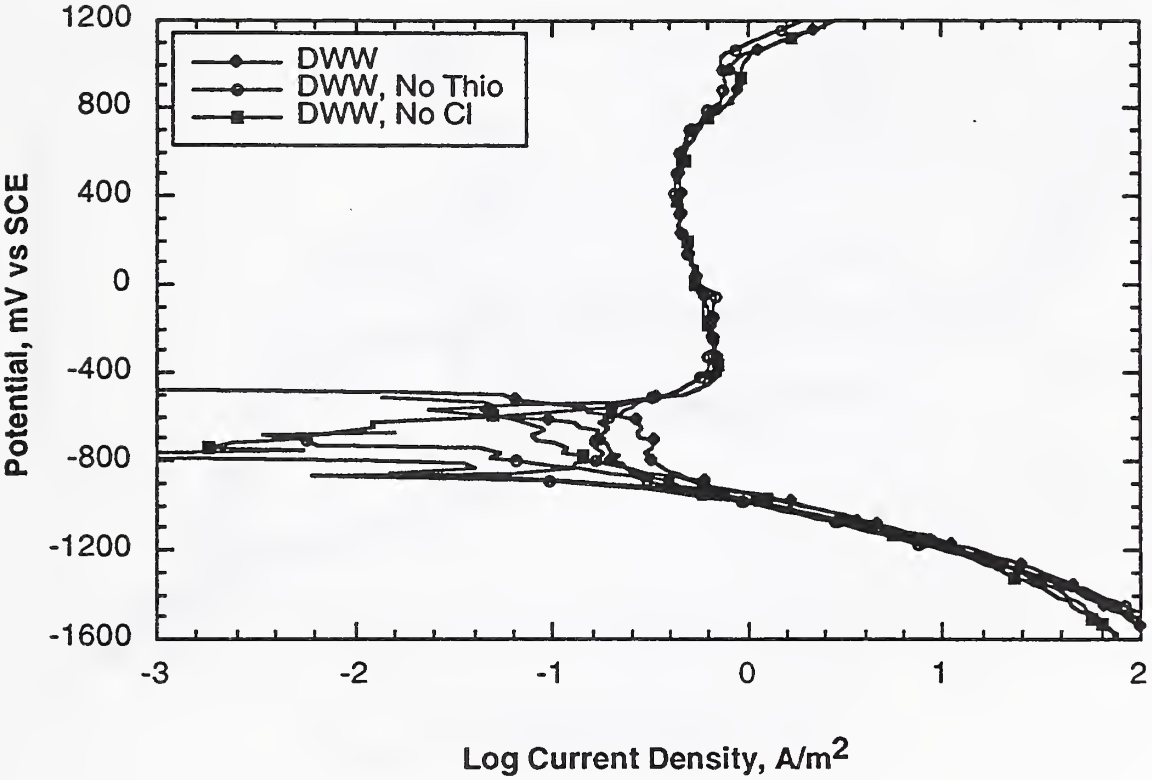

Figure 17. Comparison of the behaviors of Sandusky Alloy 75 in deinked white water solutions at 50 °C with and without thiosulfate and chloride ions. Sweep rate: 5mV/s

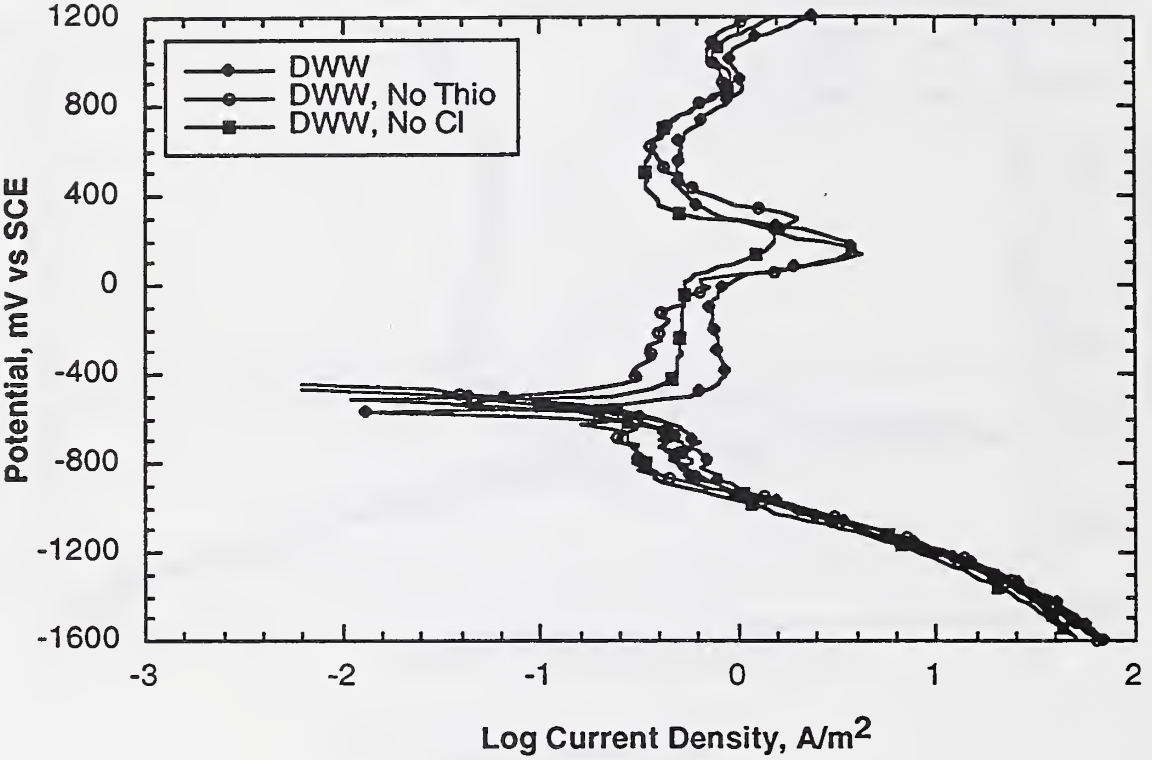

Figure 18. Comparison of the behaviors of Sandusky Alloy 86 in deinked white water solutions at 50 °C with and without thiosulfate and chloride ions. Sweep rate: 5mV/s

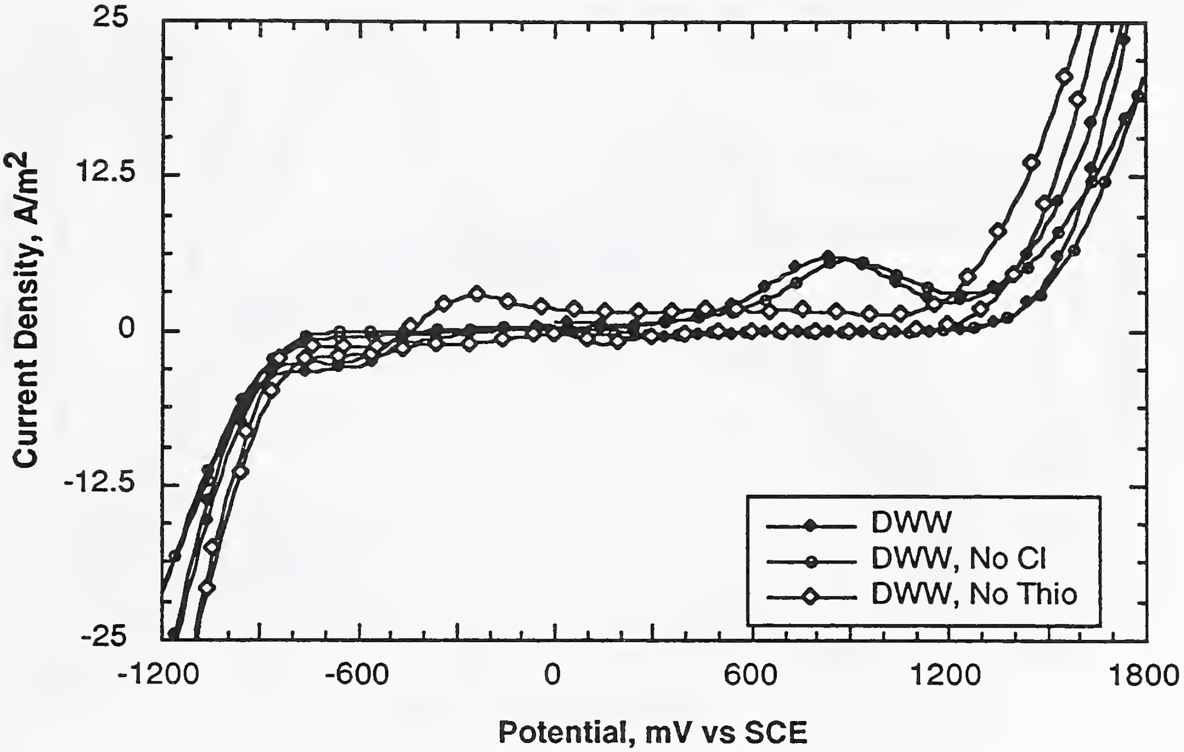

Figure 19. Cyclic voltammogram for platinum in deaerated, deinked white water at 50 °C with and without chloride and thiosulfate ions. Sweep rate: 20 mV/s

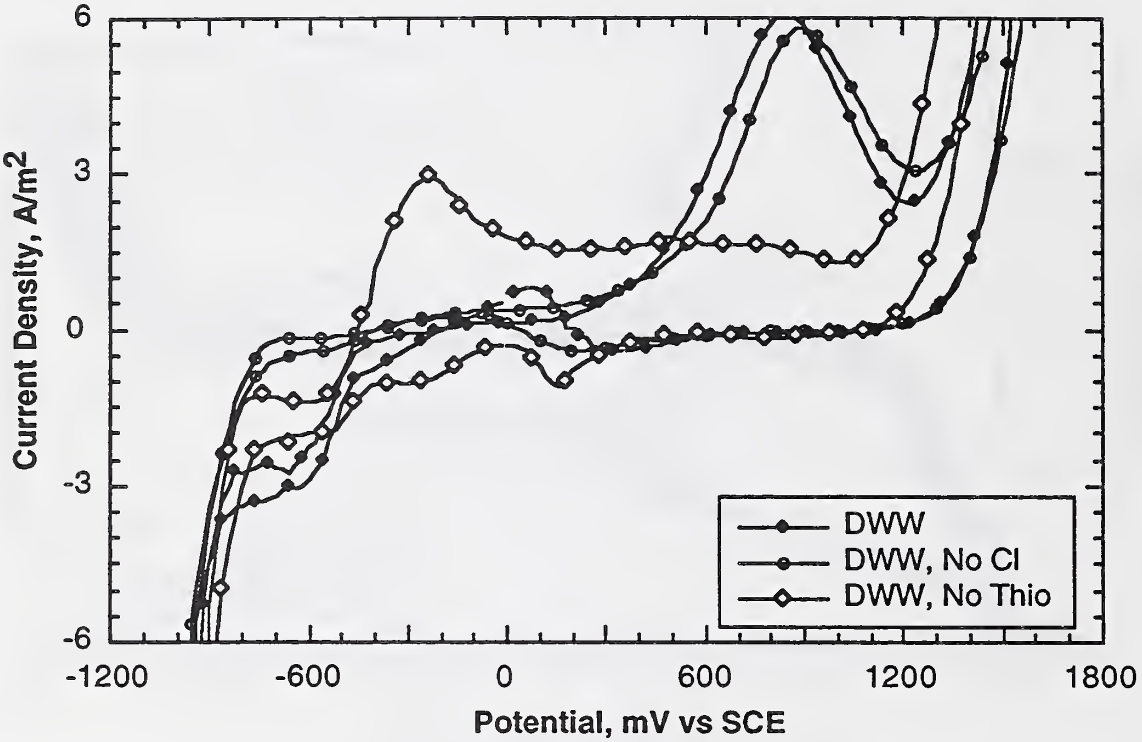

Figure 20. Cyclic voltammogram shown over a smaller current range for platinum in deaerated, deinked white water at 50 °C with and without chloride and thiosulfate ions. Sweep rate: 20 mV/s

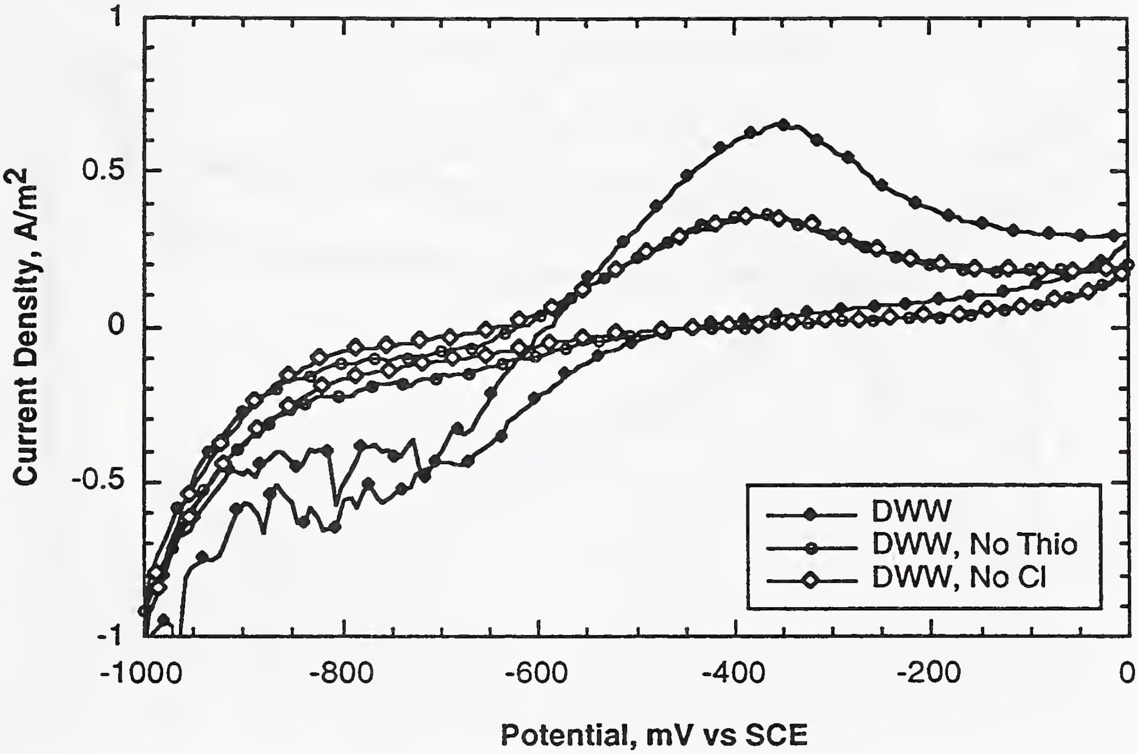

Figure 21. Cyclic voltammogram for Sandusky Alloy 75 in deaerated, deinked white water at 50 °C with and without chloride and thiosulfate ions. Sweep rate: 20 mV/s

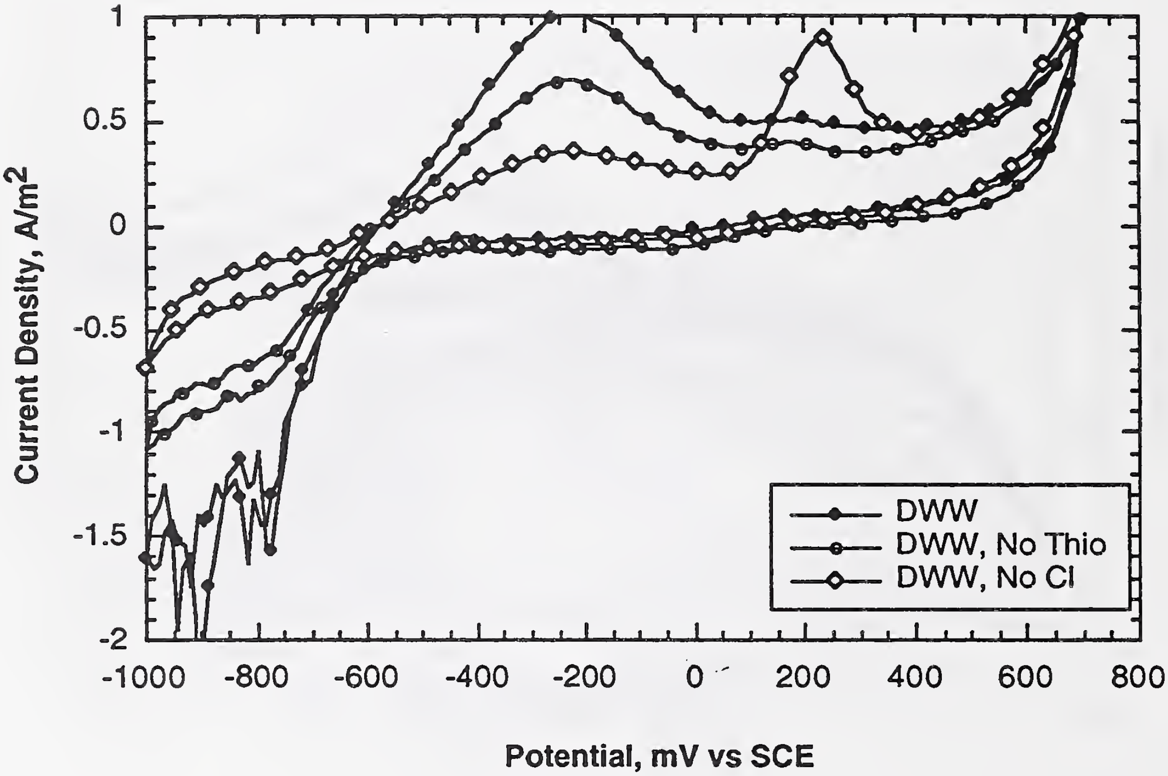

Figure 22. Cyclic voltammogram for Sandusky Alloy 86 in deaerated, deinked white water at 50 °C with and without chloride and thiosulfate ions. Sweep rate: 20 mV/s

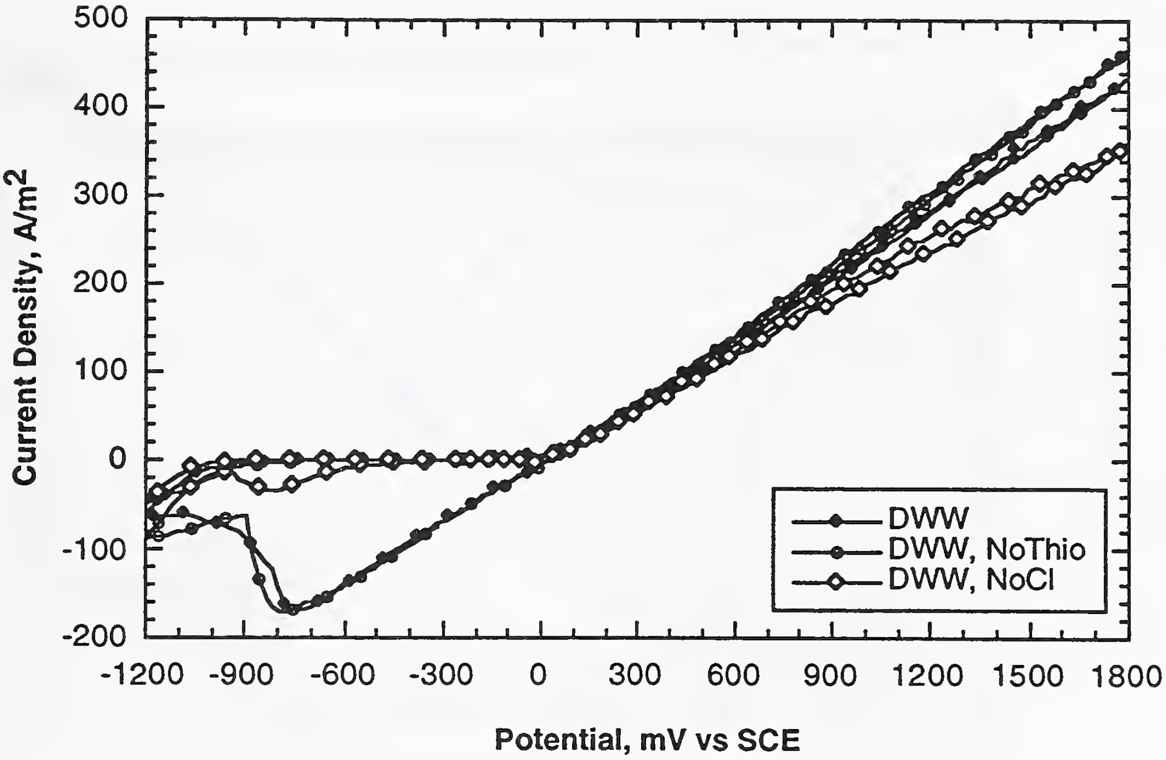

Figure 23. Cyclic voltammogram for pure copper in deaerated, deinked white water at 50 °C with and without chloride and thiosulfate ions. Sweep rate: 20 mV/s

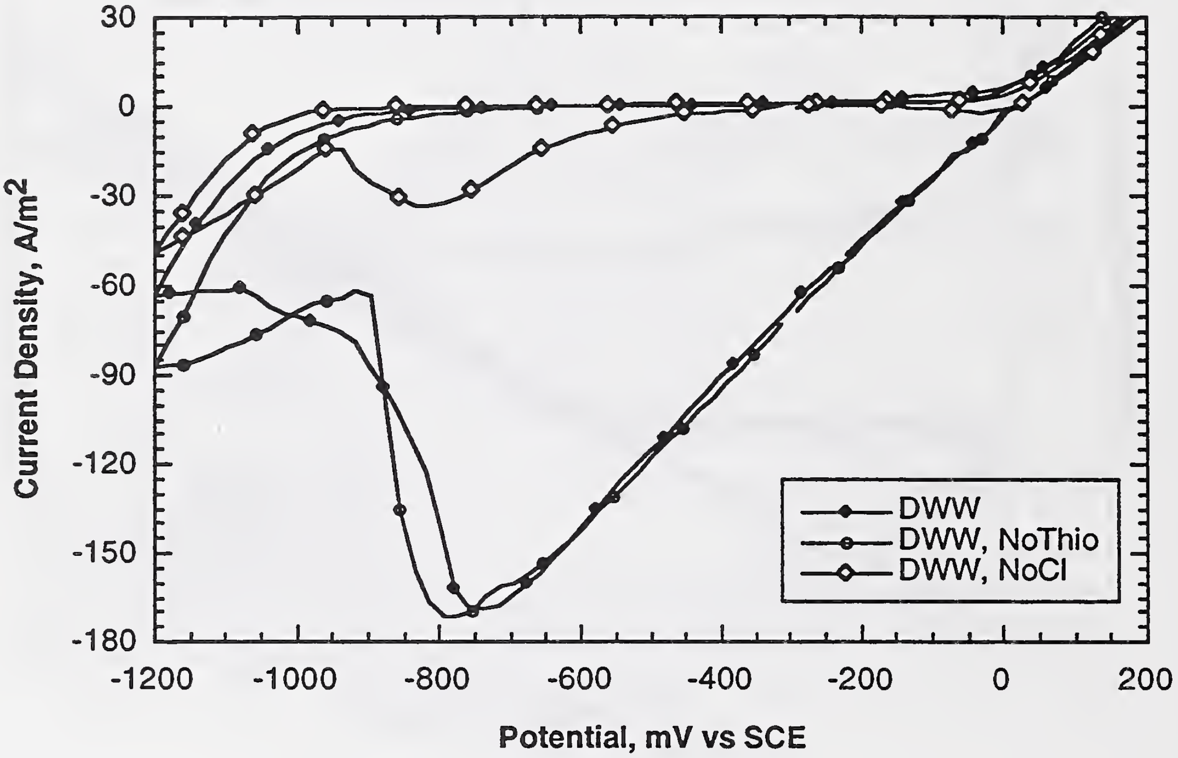

Figure 24. Cyclic voltammogram shown over a smaller current range for pure copper in deaerated, deinked white water at 50 °C with and without chloride and thiosulfate ions. Sweep rate: 20 mV/s

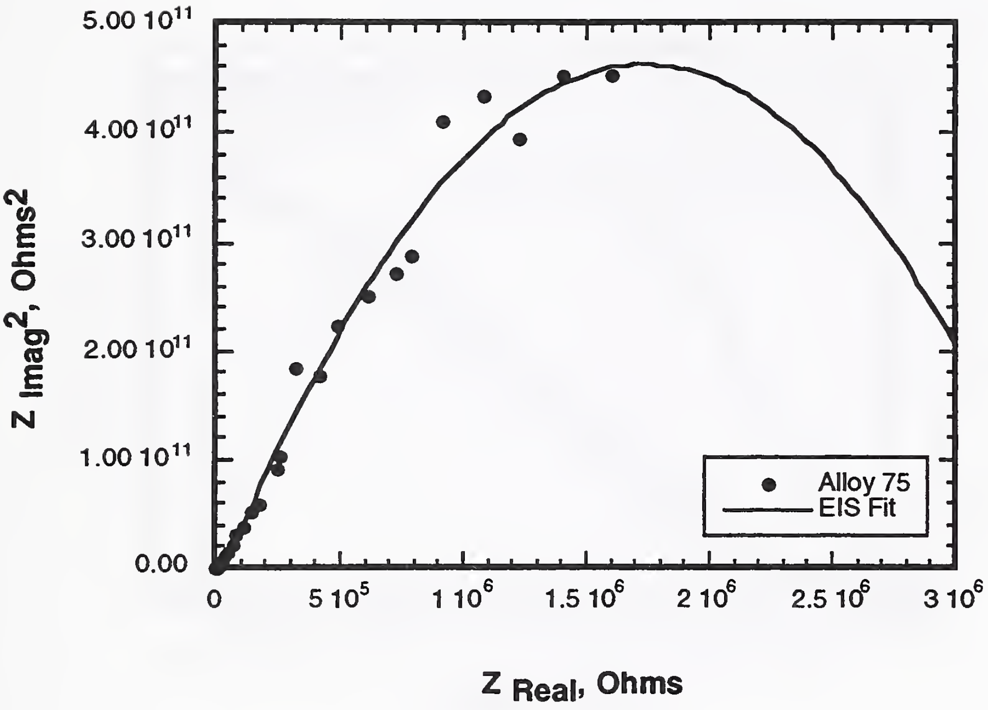

Figure 25. Electrochemical impedence spectrograph in Nyquist format for Sandusky Alloy 75 in deaerated, deinked white water at 50 °C showing the relationship between the actual data and a predictive model used to estimate the corrosion rate.

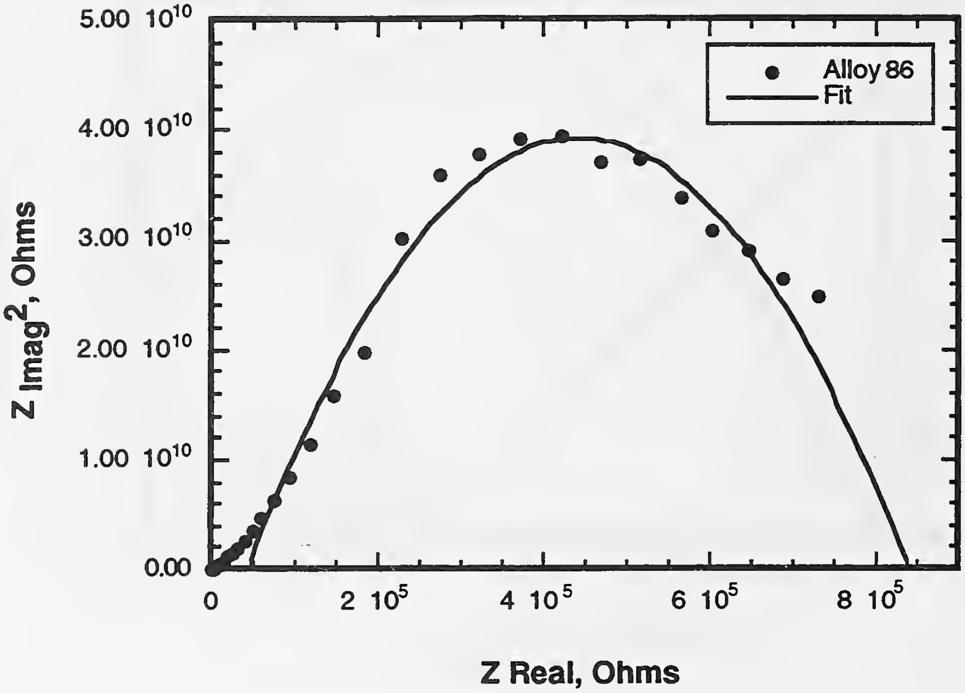

Figure 26. Electrochemical impedence spectrograph in Nyquist format for Sandusky Alloy 86 in deaerated, deinked white water at 50 °C showing the relationship between the actual data and a predictive model used to estimate the corrosion rate.

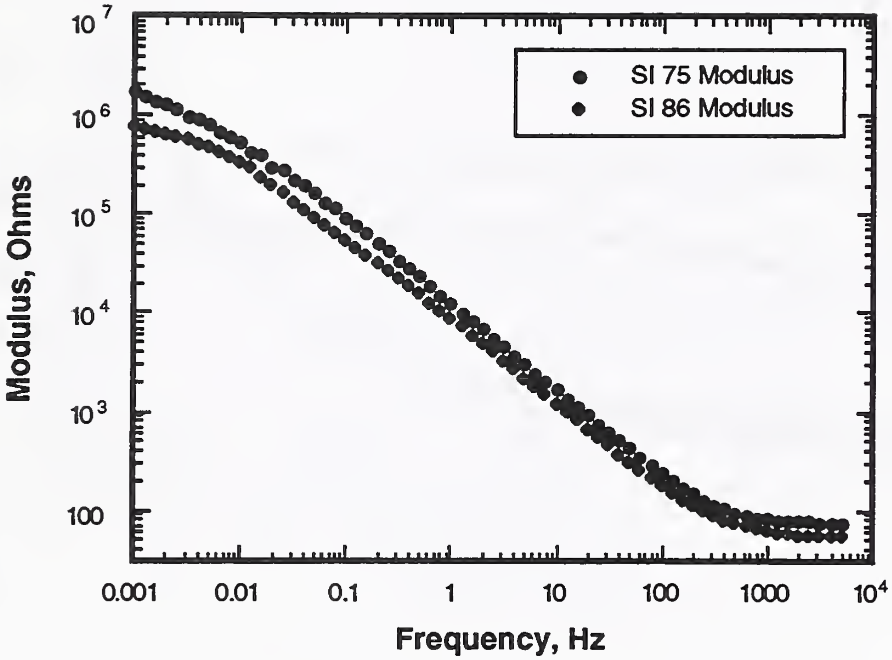

Figure 27. Electrochemical impedence spectrograph in Bode format comparing the corrosion behaviors of the two Sandusky duplex alloys in deaerated, deinked white water at 50 °C.

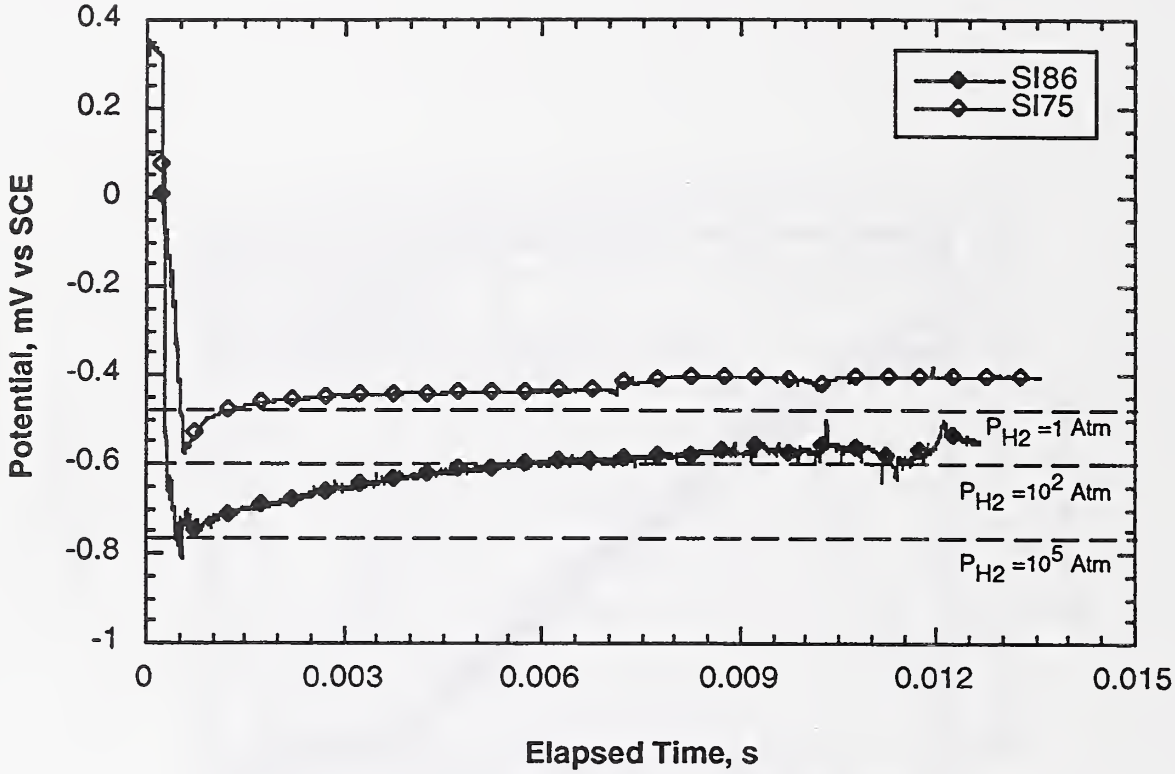

Figure 28. Scratch repassivation behavior of the two Sandusky Alloys under free corrosion conditions in aerated, deinked white water at 50 °C

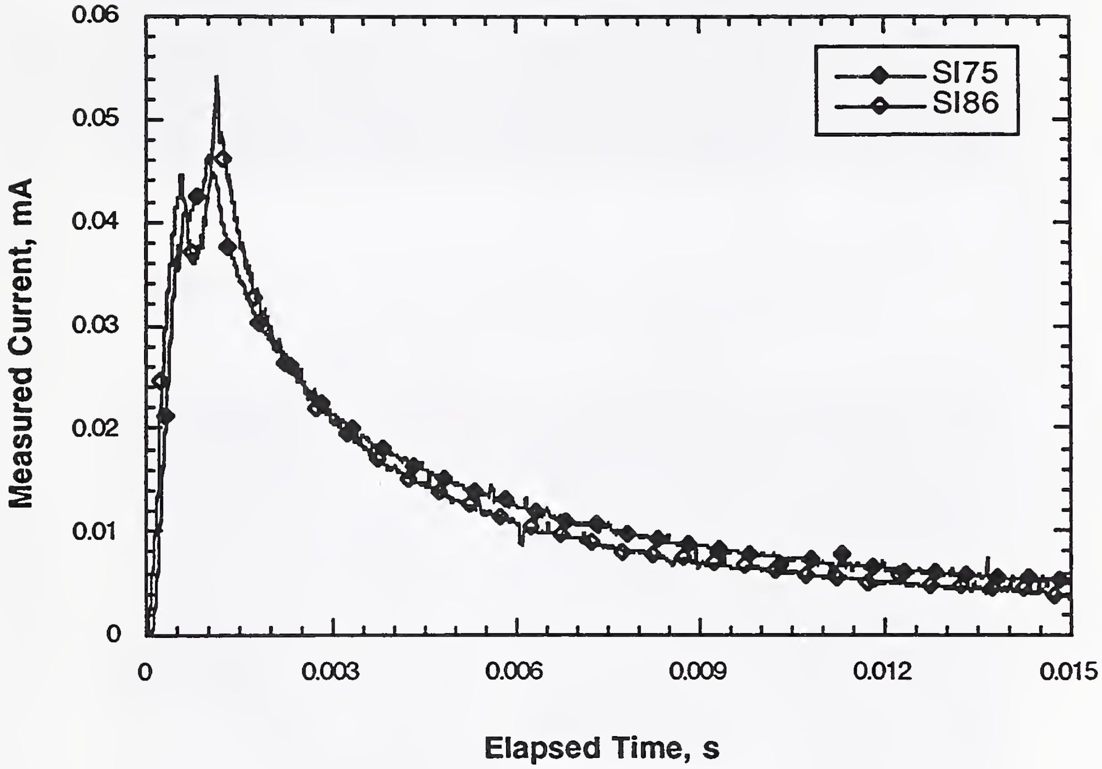

Figure 29. Scratch repassivation transients for the two Sandusky alloys in aerated deinked white water at 50 °C under a controlled potential of $-0.300V_{sce}$.

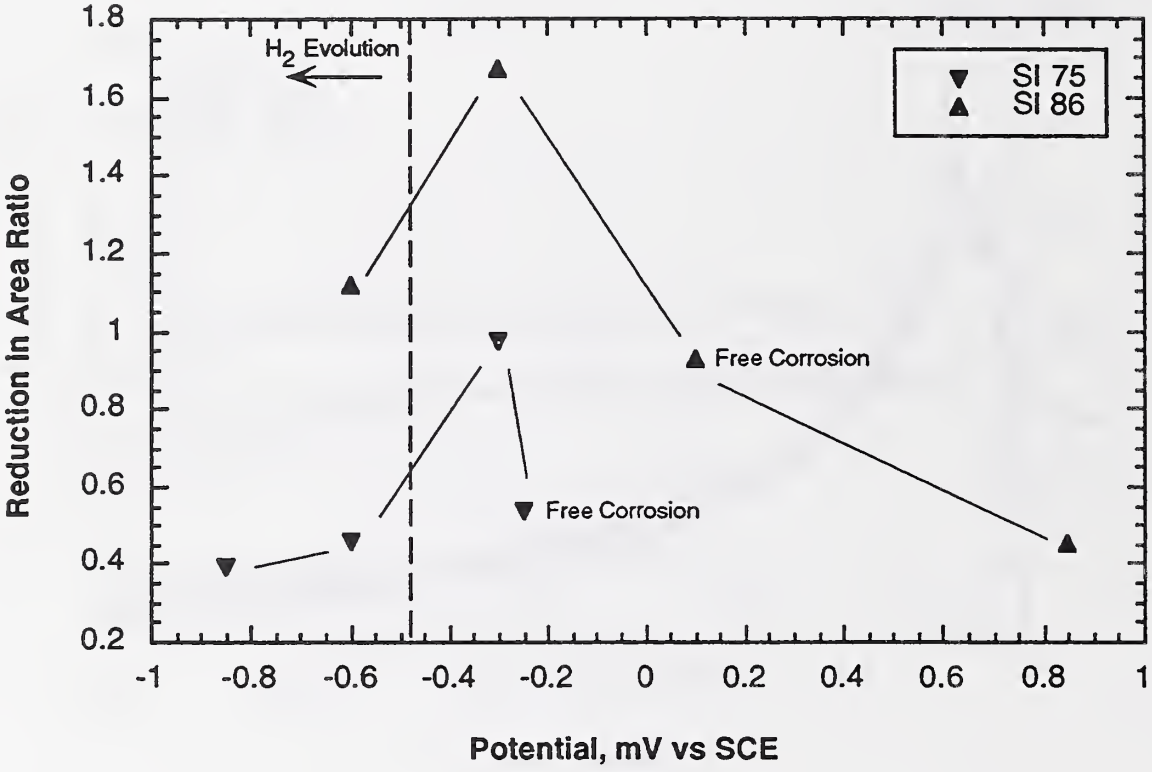

Figure 30. Plot of the reduction in area results of SSR experiments conducted in aerated deinked white water at 50 °C, ratioed to the nitrogen values, versus the electrode potential.

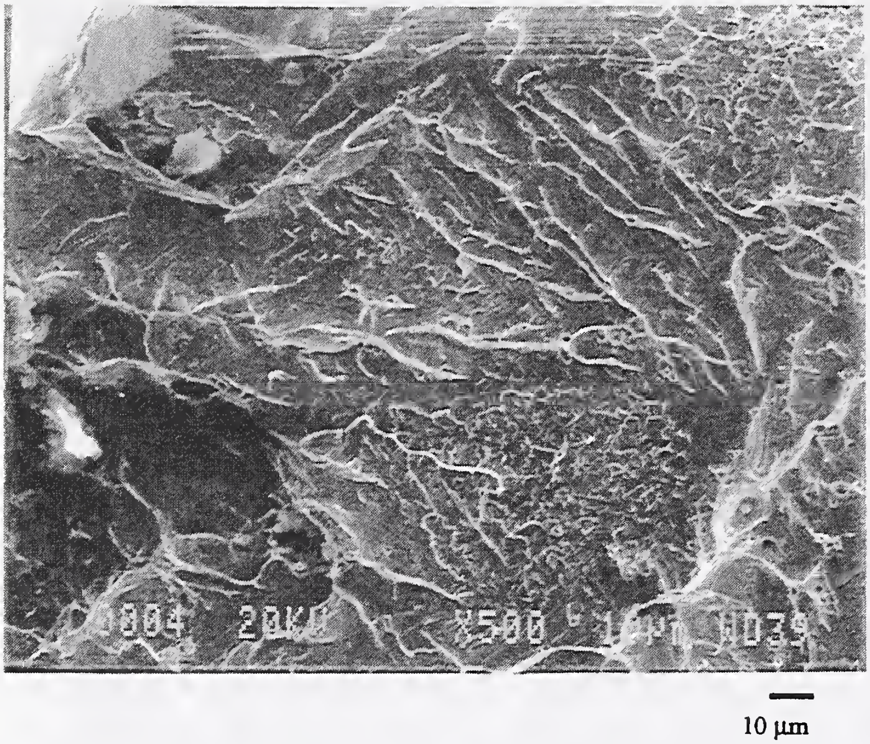

Figure 31a. Scanning electron micrograph showing the SSR fracture behavior of Sandusky Alloy 75 in Nitrogen at 50 °C.

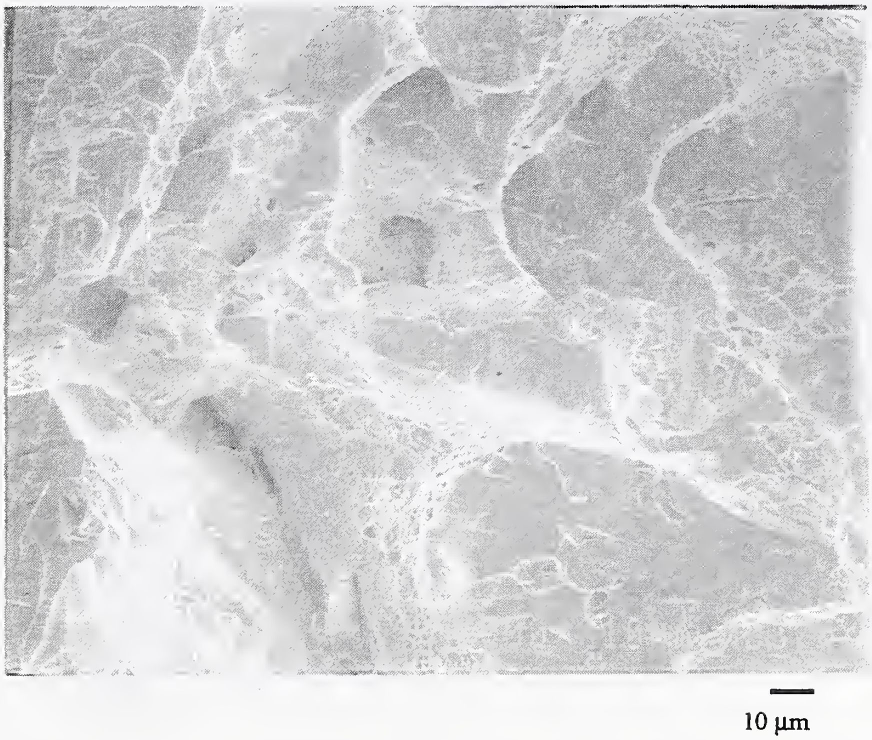

Figure 31b Scanning electron micrograph showing the SSR fracture behavior of Sandusky Alloy 86 in Nitrogen at 50 °C.

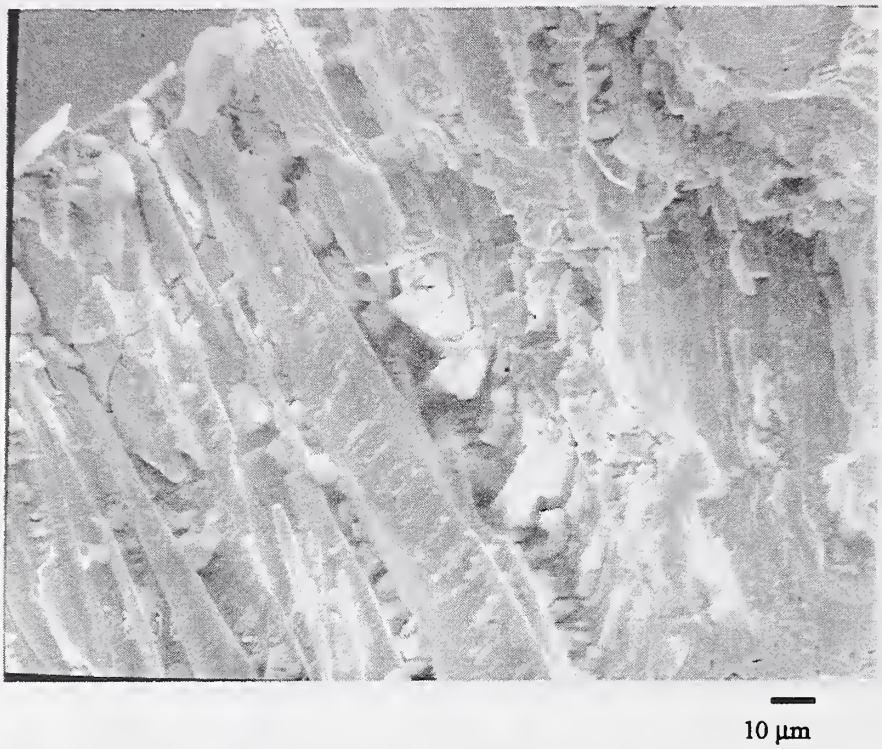

Figure 32a. Scanning electron micrograph showing the SSR fracture behavior of Sandusky Alloy 75 under free corrosion conditions in aerated, deinked white water at 50 °C.

Figure 32b. Scanning electron micrograph showing the preferential attack in the austenite phase of the Sandusky Alloy 75 SSR specimen tested under free corrosion conditions in the deinked white water solution at 50 °C.

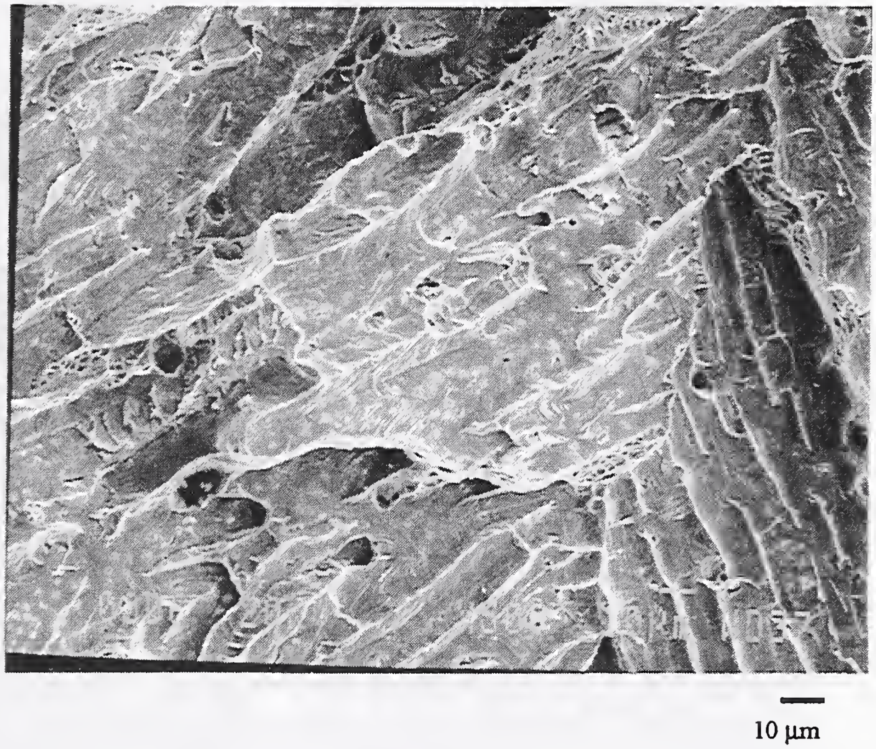

Figure 33. Representative scanning electron micrograph showing the SSR fracture behavior of Sandusky Alloy 86 under a controlled electrode potential of -0.300 V_{sce} in aerated deinked white water at 50 °C.

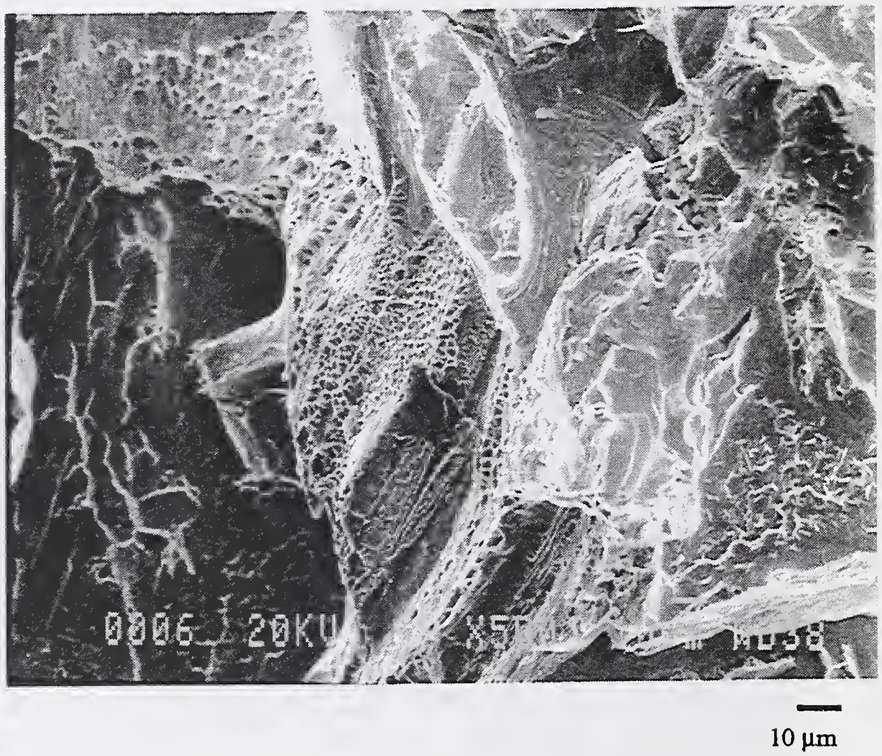

Figure 34. Representative scanning electron micrograph showing the SSR fracture behavior of Sandusky Alloy 75 under cathodic protection conditions at an electrode potential of -0.600 V_{sce} in aerated deinked white water at 50 °C.

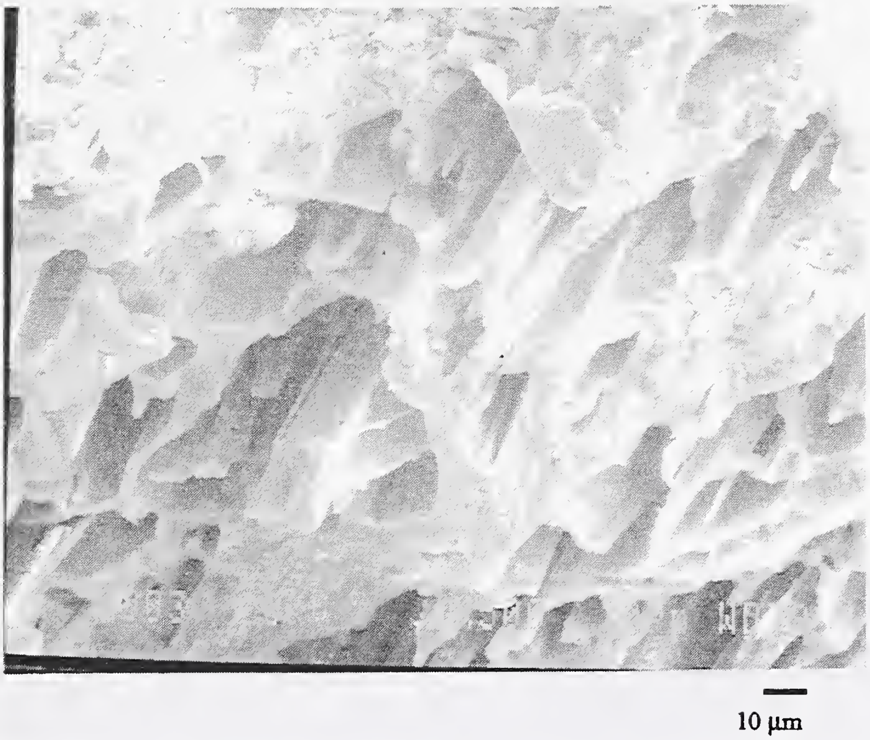

Figure 35a. Scanning electron micrograph showing the SSR fracture behavior of Sandusky Alloy 86 near the pitting potential in aerated, deinked white water at 50 °C.

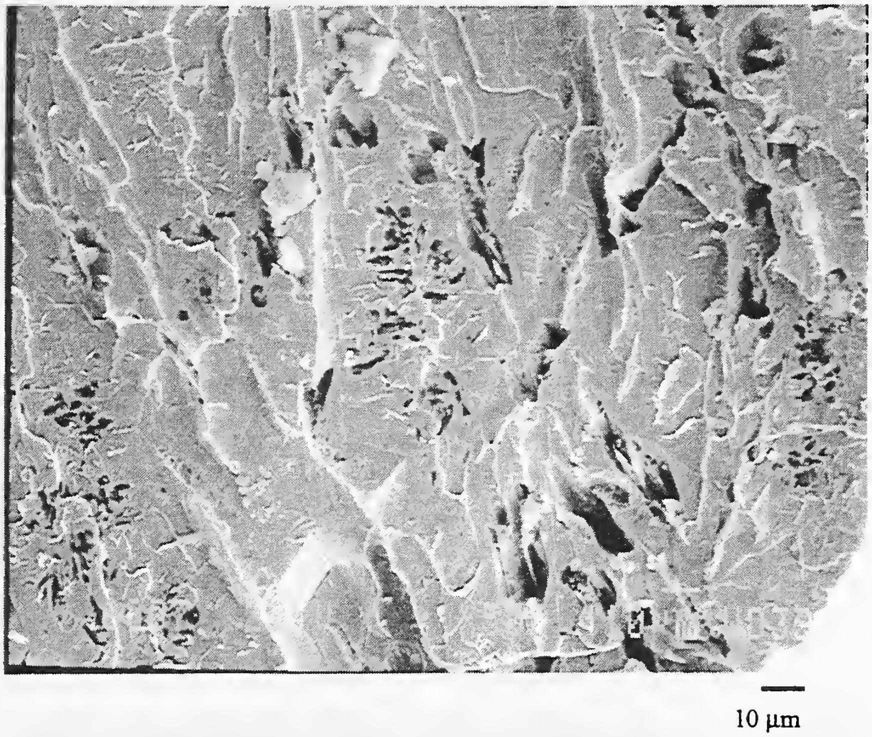

Figure 35b. Scanning electron micrograph showing the preferential attack in the austenite phase of the Sandusky Alloy 86 SSR specimen tested near the pitting potential in the deinked white water solution at 50 °C.

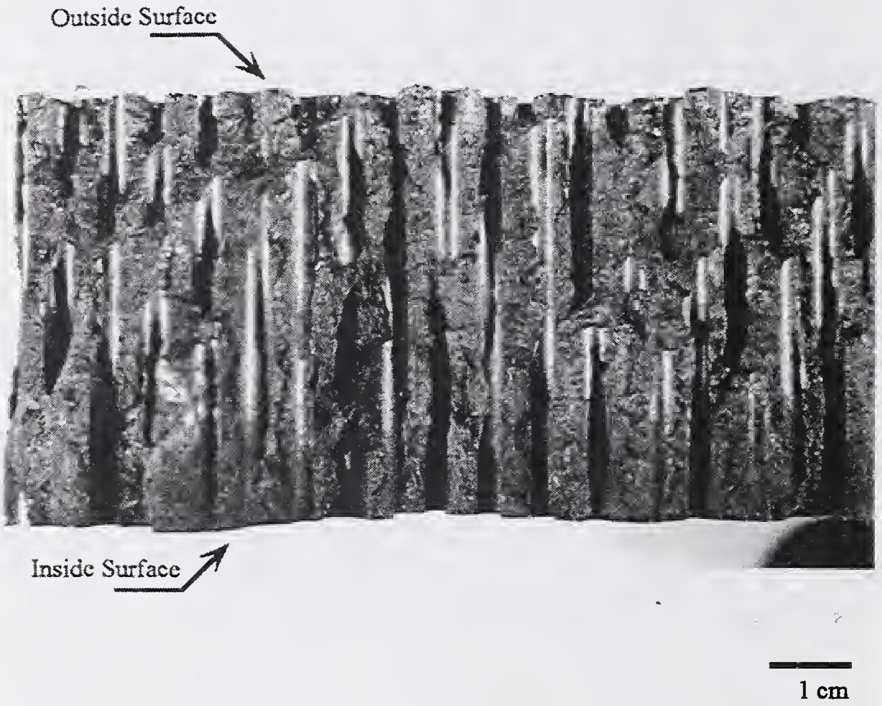

Figure 36. Low magnification overview of the surface of a failed Sandusky Alloy 75 suction roll shell showing the arrangement of drilled holes and fractured ligaments.

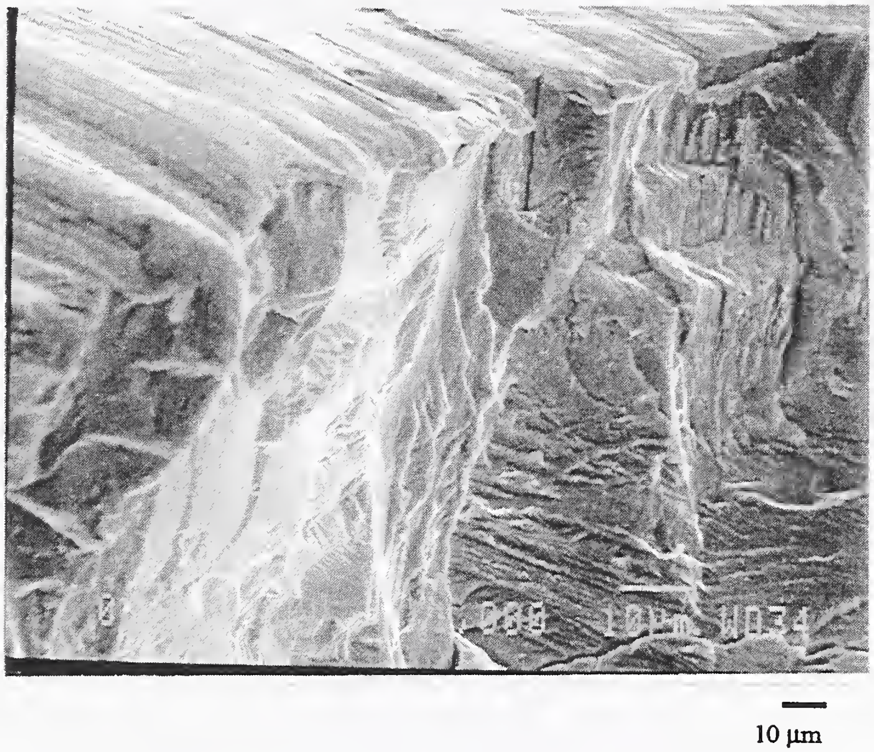

Figure 37. Scanning electron micrograph showing several small fatigue cracks initiating at the base of corrosion pits located on the internal diameter surface of a failed Sandusky Alloy 75 suction roll shell.

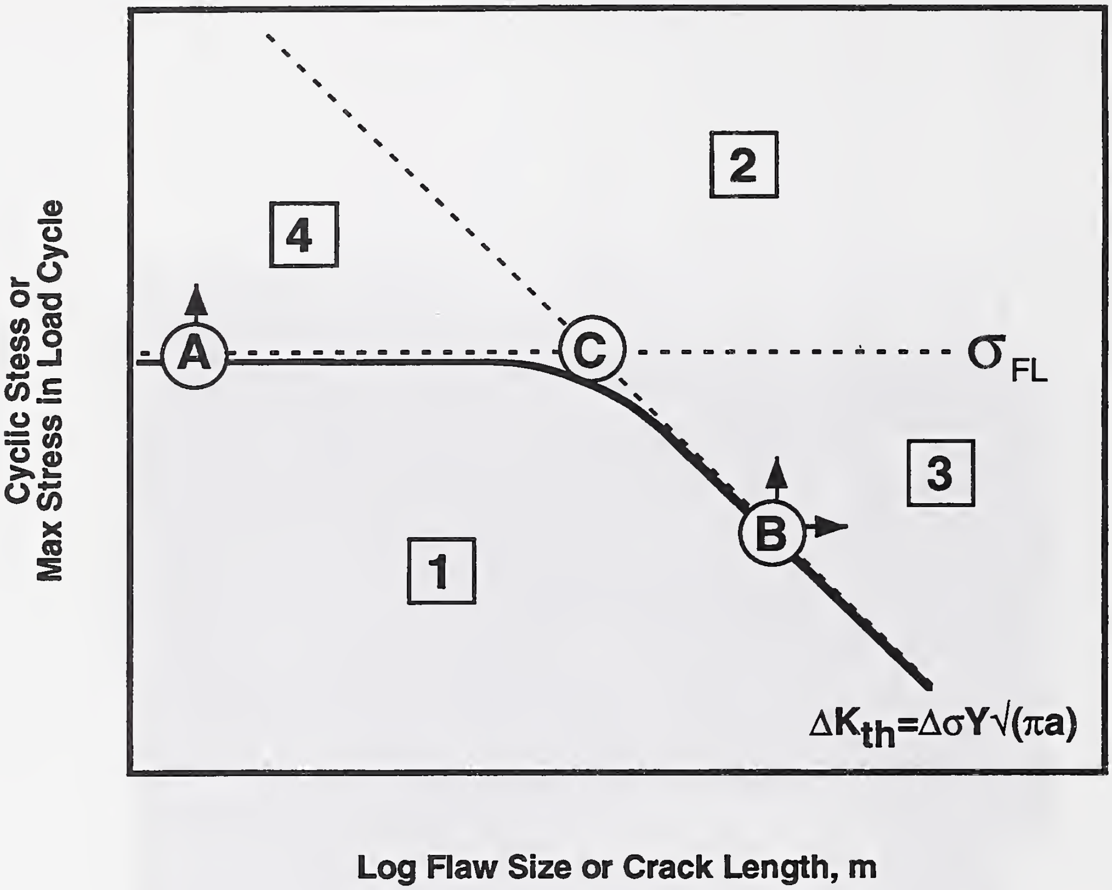

Figure 38. Relationship between the cyclic stress required to cause fatigue failure and the crack or flaw size. (After Kitagawa)